EFFECTS OF EXTERNAL FACTORS ON THE FLUIDITY OF SUPPORTED LIPID BILAYERS AND CELL MEMBRANES

By

Masroor Hossain

A DISSERTATION

Submitted to
Michigan State University
in partial fulfillment of the requirements
for the degree of

Chemistry – Doctor of Philosophy

2020

ABSTRACT

EFFECTS OF EXTERNAL FACTORS ON THE FLUIDITY OF SUPPORTED LIPID BILAYERS AND CELL MEMBRANES

By

Masroor Hossain

Biological plasma membranes are essential for a cell's proper function. They play key roles in cell-communication, structural support, and are involved in key processes, such as inducing anesthesia. They are composed of hundreds of distinct molecules with the majority being phospholipids, followed by proteins and carbohydrates. We take advantage of this well-crafted system by creating artificial bilayer models, whose parameters are well-controlled. Ultimately, the goal of this research is to understand the complex interplay of molecules in a model bilayer through translational diffusion constants and connect the results to live plasma membranes.

The model bilayer composition was simplified by focusing on major lipids, namely cholesterol, 1,2-dioleoyl-*sn*-phosphatidylcholine (DOPC), sphingomyelin, and ceramide on mica substrates. Various applications of artificial membranes exist, and we choose to focus on the area of anesthesiology. Though anesthesia use continues to be vital, from minor to major surgical processes, molecular mechanisms are not clear and lack of widespread consensus on theories cause debate among researchers. The main contenders are anesthetics acting directly on proteins or indirectly by dissolving in lipids and affecting transmembrane protein functions. Drawing from previous work in the Blanchard research group, we apply ethanol and *n*-butanol, on our models to understand interactions of general anesthetics with the bilayer. With perylene or 1,2-dioleoyl-*sn*-glycero-3-phosphoethanolamine-N-(lissamine rhodamine B sulfonyl) as fluorescent probes (sensitive to phospholipid headgroup or tail mobility, respectively), the fluorescent recovery after photobleaching (FRAP) technique results in fluorescence recovery curves of the supported lipid

bilayers, from which translational diffusion constants are extracted. The values are related directly to fluidity and, as predicted, application of the short-chain alcohols led to higher diffusion coefficients overall. However, high alcohol concentrations resulted in lower diffusion coefficients potentially due to bilayer interdigitation. On both the macroscopic and microscopic scale, ceramide rigidified the system.

As a whole, further investigations pointed to the heterogeneous morphology of the models. Size-dependent FRAP measurements led to an important observation that anomalous diffusion is occurring. Ultimately, results from the models need to be connected with those on live cell membranes and we had this experience with a collaborative project with the Busik laboratory in the physiology department at Michigan State University.

Their group works on various projects, one of which involves treatment options for retinal-based degradation in diabetic subjects. Increased cholesterol generally decreases membrane fluidity, and related to our research goals, the drug N, N-dimethyl-3β-hydroxy-cholenamide (DMHCA), a selective LXR agonist, rejuvenated circulating angiogenic cell (CAC) membrane fluidity which has potential in vascular repair of people afflicted with the diabetic retinopathy complication.

Dedicated to Afroz Hossain, Riham Hossain, Nahin Mulla, and late Mohammed Mazdar Hossain
who all sacrificed more than I can imagine.

ACKNOWLEDGEMENTS

First and foremost, I would like to thank my amazing advisor Dr. Gary Blanchard. He deserves more gratitude than I can express. In addition to his critical insight and suggestions, he is welcoming with a literal open-door policy, generous, kind, and understanding. From the first day I joined his research group, expectations were clearly explained. His knowledge of both academic and industrial settings helped tremendously, and I am fortunate to have worked under his supervision. I thoroughly enjoyed scientific and academic discussions, soup lunches, words of wisdom, and hilarious stories. In addition, I am grateful to the rest of the group - Sheryl Blanchard, Dr. Stephen Baumler, Dr. Xiaoran Zhang, Dr. Krystyna Kijewska, Dr. Barrack Stubbs, Dr. Ke Ma, Briana Capistran, Yufeng Wang, Corbin Livingston, Iqbal Hossain, Andrew Wendel, Alexandra Korabiewski, Austin Benedict, Yasmine Farhat, and Stephanie Schiffert.

I also appreciate the opportunity to have collaborated with Dr. Busik's physiology group and members Dr. Seda Grigoryan, Dr. Sandra Hammer, Dr. Yan Levitsky, Dr. Chao Huang, Svetlana Navitskaya, Kiera Fisher, Anthony Novello, Delaney McFarland, David Pegouske, and Travan Gentles. Along those lines, Dr. Maria Grant and her ophthalmology and visual sciences group deserve my gratitude as well: Dr. Cristiano Vieira, Dr. Ana Leda Longhini, Mariana DuPont, and others I communicated with indirectly.

Thank you to my guidance committee members Dr. Julia Busik, Dr. Dana Spence, Dr. David Weliky, and Dr. Greg Swain for their support, suggestions for my research, and other advice.

I would like to thank my previous research group advisor Dr. James McCusker and members Dr. Jennifer Miller, Dr. Monica Carey, Dr. Bryan Paulus, Dr. Christopher Tichnell, Dr.

Sara Adelman, Dr. Daniela Arias-Rotondo, Dr. Shuxuan Li, Matthew Woodhouse, Jonathan Yarranton, Phillip Casamento, and Karl Nielsen.

It was a pleasure learning from various instructors in classes, and I appreciate their tutelage: Dr. Thomas Hamann, Dr. Rémi Beaulac, Dr. Aaron Odom, Dr. James McCusker, Dr. John McCracken, Dr. Denis Proshlyakov, Dr. Mitch Smith, Dr. Gary Blanchard, Dr. Greg Swain, Dr. Dana Spence, Dr. Liangliang Sun, Dr. David Weliky, and Dr. Heedeok Hong.

I am grateful to have worked with many during my teaching assignments, particularly Dr. Joseph Ward, Dr. Amy Pollock, Dr. Virginia Cangelosi, Dr. Kathryn Severin, Dr. Thomas Carter, and Todd Burkhart.

I appreciate staff's willingness to help, Anna Osborn, Tiphani Scott, Heidi Wardin, Bob Rasico, Eric Smariege, Brenda Franklin, Dianne Karsten, Dawn Kuhn, Mary Mroz, David Voss, Letta Dibaba, and Bill Flick.

Thank you to Dr. Babak Borhan and Dr. Xuefei Huang for access to freezers in the penthouse and DLS instrument, respectively.

Thank you to friends from board game groups (Friend Zone, CGN, LAGE) and other recreational activities for fun times. Thank you to fellow graduate students for scientific discussions, activities (like ping pong), and rooming together - Eziz Kuliyev and Daniel Steigerwald. Thank you to Lauren Skrajewski for showing me how to use EndNote. In Gary's words, "it is a game changer." Thank you to Dr. Katharina Domnanich and Amanda Setser for various kinds of knowledge and advice.

Special thanks to family, dear friends, and influential individuals who supported, encouraged, motivated, and inspired me to do my best, like Jenna, Obi, Sarvie, Komal, Josh, Mojtaba, Roxanne, Michelle, Mo, Vernon, Trent, Natalie, Kio, Ben, Evelyn, Charlie, Clarice, Mr. Phanisha Mandagere, and those no longer with us, notably Carol Whitney, David Haan, and Yu-Ling Lien.

This research would not have been possible without funding from the National Institutes of Health and MSU Department of Chemistry, for which I am grateful.

Thank you to high school teachers Dr. Myers, Mr. Branch, Mr. Carlson, and Ms. Ransford. Thank you to college instructors Dr. Barth, Dr. Bartz, Dr. Smith, Martha Warpehoski, and previous employers.

Though not mentioned here directly, I am grateful for the help and guidance of many. As the African proverb goes, “it takes a village to raise a child.”

I tend to be meticulous and detail-oriented, sometimes focusing on a leaf or a tree. Both Gary and Jim guided me to look at the forest as well (big picture) and finding balance has been an area for continuous growth and improvement.

My graduate career has been far more than an academic challenge but also one of personal development and growth. It is part of my journey of using chemistry to make a significant impact in people’s lives. A lesson in perseverance reverberated throughout my time as a graduate student, especially in times of hardship and low morale:

We fall so we can learn how to pick ourselves up.

TABLE OF CONTENTS

LIST OF TABLES

LIST OF FIGURES

KEY TO SYMBOLS AND ABBREVIATIONS

$\langle r^2 \rangle$	mean square displacement
^{2}H-NMR	deuterium nuclear magnetic resonance
α	anomalous diffusion coefficient
ABCA1	ATP-binding cassette transporter
ACCORD	Action to Control Cardiovascular Risk in Diabetes
ACS	American Chemical Society
AF	alexafluor
AFM	atomic force microscopy
AMD	age-related macular degeneration
ANOVA	analysis of variance
APC	allophycocyanin
ASM	acid sphingomyelinase
ATP	adenosine triphosphate
BB	brilliant blue
BLM	black lipid membranes
BM	bone marrow
BV	brilliant violet
CAC	circulating angiogenic cell
CCL	chemokine (C-C motif) ligand
CCR	chemokine receptor
CD	cluster of differentiation
cer	ceramide

CFU	colony forming unit
Chol	cholesterol
Cy5	cyanine 5
D	translational diffusion constant
DAPI	4′,6-diamidino-2-phenylindole
db/db	diabetic mice
db/m	control mice
DC	dendritic cell
DGE	differential gene expression
DLS	dynamic light scattering
DMHCA	N, N-dimethyl-3β-hydroxy-cholenamide
DMSO	dimethyl sulfoxide
DOPC	1,2-dioleoyl-*sn*-phosphatidylcholine
DOPE	1,2-dioleoyl-*sn*-glycero-3-phosphoethanolamine
DR	diabetic retinopathy
ELISA	enzyme-linked immunoassay
ERG	electroretinogram
ESR	electron spin resonance
FADI	fluorescence anisotropy decay imaging
FBS	fetal bovine serum
FITC	fluorescein isothiocyanate
FLT	FMS like tyrosine kinase
FRAP	fluorescence recovery after photobleaching

$GABA_A$	γ-aminobutyric acid type A
GEMM	granulocyte, erythroid, macrophage, megakaryocyte
GMP	granulocyte myeloid progenitor
HBB-BT	hemoglobin β adult t chain
HIV	human immunodeficiency virus
HS/PC	hematopoietic stem and progenitor cell
HSC	hematopoietic stem cells
HV	high voltage
IACUC	institutional animal care and use committee
IL	interleukin
IM	intramuscular
I_o, I_1	modified Bessel functions
IPA	ingenuity pathways analysis
IRB	institutional review board
KO	knockout
LC-MS	liquid chromatography-mass spectrometry
L_d	liquid-disordered
LDL	low-density lipoproteins
Liss Rhod PE	lissamine rhodamine phosphoethanolamine
L_o	liquid-ordered
LSK	lineage$^-$sca1$^+$c-Kit$^+$
LT	long-term
LTQ	linear trap quadrupole

LXR	liver X receptor
MAST	Model-based Analysis of Single-cell Transcriptomics
MEP	megakaryocyte-erythrocyte progenitor
mol	mole
n	number of measurements
NMDA	N-methyl-D-aspartate
PAGA	partition-based graph abstraction
PBS	phosphate-buffered saline
PC	polycarbonate
PE	phycoerythrin
PMT	photomultiplier tube
pO_2	partial pressure of oxygen
PSD	particle size distribution
qPCR	quantitative polymerase chain reaction
r	radius of diffusing moiety
RBC	red blood cell
RCT	reverse cholesterol transport
RI	refractive index
RNA	ribonucleic acid
ROI	region of interest
SALB	solvent-assisted lipid bilayer
SB	super bright
scRNA-seq	single-cell RNA sequencing

SEM	standard error of the mean
SLB	supported lipid bilayer
SM	sphingomyelin
SR	sulforhodamine
SREBP-1c	sterol regulatory element-binding protein-1c
ST	short-term
T	temperature
t	time
τ_D	characteristic diffusion time
T2D	type 2 diabetes
TCSPC	time-correlated single-photon counting
Texas Red	sulforhodamine 101 acid chloride
TNF	tumor necrosis factor
UMAP	uniform manifold approximation and projection
UV	ultraviolet
v	volume
WT STZ	wild type streptozotocin
η	viscosity
ω	radius of circular beam

CHAPTER 1: INTRODUCTION

Biological membranes are responsible for protecting a cell from its environment and play key roles in transport, cell communication (via proteins), and structural support. It is mainly composed of lipids (phospholipids and sterols) with interspersed proteins and some carbohydrates attached to lipids (glycolipids) and to proteins (glycoproteins). An amphiphilic phospholipid consists of a hydrophilic phosphate headgroup and a hydrophobic hydrocarbon chain/acyl tail group, both connected to a glycerol molecule (Figure 1.1). The polar head group orients toward aqueous media while the non-polar tails face each other. There exists a “gallery” region between the phospholipid leaflets in a bilayer. Singer and Nicolson’s fluid mosaic model proposed in 1972 emphasized the lipid bilayer’s fluidity.[1] It is thought to play a key role in how anesthetics work on the molecular level.

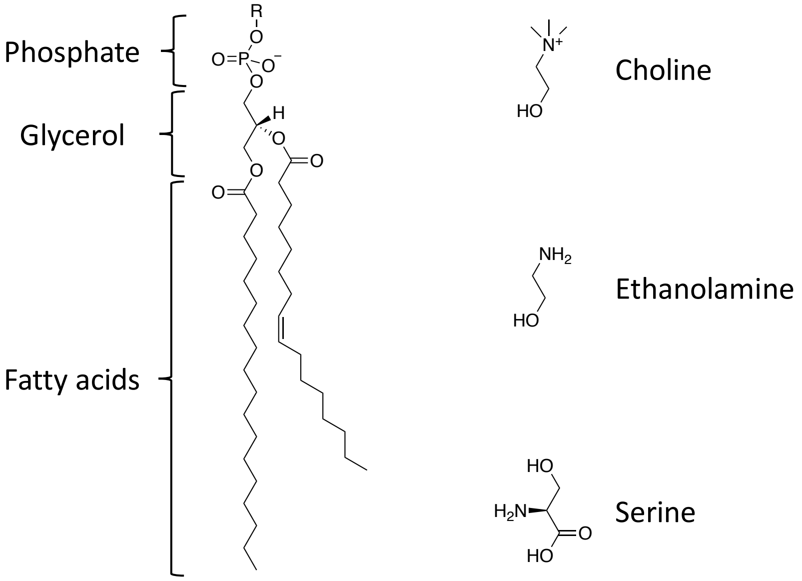

Figure 1.1. Molecular Structure of a Generic Phospholipid. Some examples of the R group are choline, ethanolamine, and serine, shown to the right. The left-most hydrophobic tail is saturated and the other is unsaturated, and the bend shown is exaggerated for emphasis.

The four main types of anesthesia are local which numbs a small area of the body; regional, which blocks pain in a large part of the body such as an arm or a leg; general which involves unconsciousness, amnesia, and analgesia; and monitored/conscious sedation where a patient is in a deep “twilight” state of feeling relaxed and staying conscious, with the possibility of sleep and no memory of the surgical procedure.[2] Examples of anesthetics include lidocaine (local), clonidine (regional), propofol (general), and nitrous oxide (sedation) (Figure 1.2).[3, 4] In this work, we focus on general anesthetics.

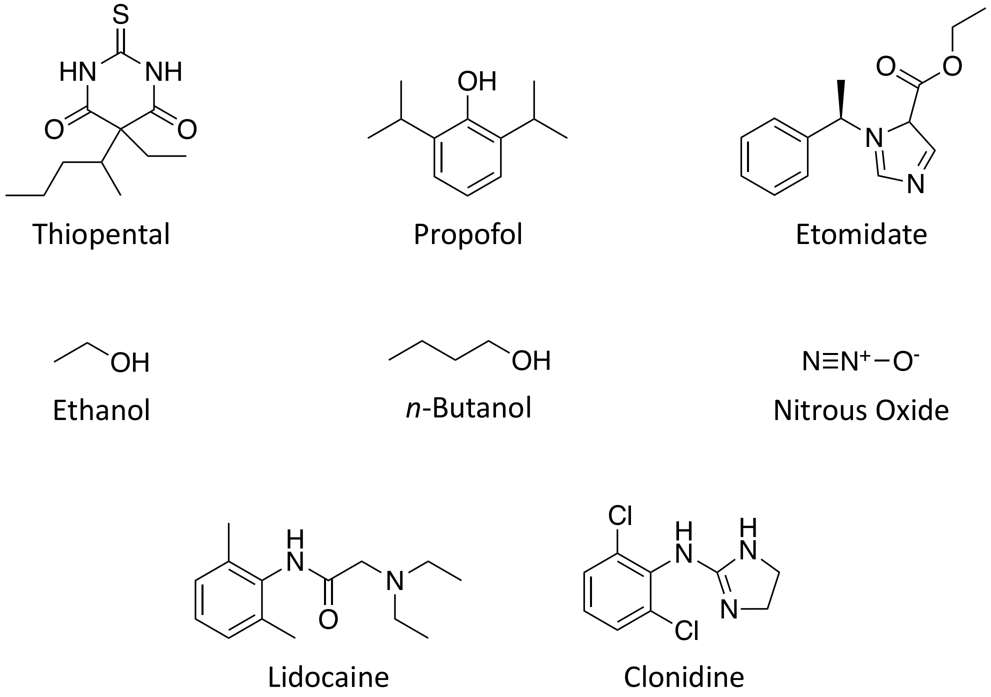

Figure 1.2. Molecular Structures of Anesthetics. The top six have been used in general anesthesia.

General anesthetics have been in use as far back as 1540 by Paracelsus, and the first public demonstration of ether in surgery was in 1846 by Morton, and though the physiological effects are well known, how they work on a molecular level is still unclear.[5] Meyer and Overton correlated anesthetic potency with lipid solubility, and their theory gained prominence in the 1900s.[6] They argued that anesthetic molecules, despite varying chemical structures (Figure 1.2), cause changes in the structure of the bilayer (such as its fluidity) which may indirectly affect how integral membrane proteins function, inducing anesthesia.[6]

Although the Meyer-Overton theory was widely accepted, exceptions exist such as fluorothyl - shows no anesthetic activity but is structurally similar to anesthetics, α-chloralose - potent anesthetic but with low lipid solubility, and chloral hydrate - less potent than predicted.[7-9] Moreover, Franks and Lieb presented evidence in the late 1970s that general anesthetics interact directly with proteins; in particular, their X-ray and neutron diffraction data showed that the primary site of action of general anesthetics had both non-polar and polar characteristics, implying that the site was composed of protein.[10] They also performed other physical and electrophysiology-based experiments to strengthen their theory.[10-14] The inhibitory γ-aminobutyric acid type A ($GABA_A$) receptor was discovered to be a main target for anesthetic action and acts by blocking nerve impulses.[15, 16] However, other targets also exist such as the glycine[17], nicotinic acetylcholine[18], and N-methyl-D-aspartate (NMDA) receptors[19].[20] While scientists are leaning toward the direct mechanism of action with different protein receptors, there is still widespread debate on the theories. Nonetheless, a central theme that arises is that the fluidity of the plasma membrane could be affected, whether indirectly or directly.

Membrane fluidity lacks an accurate definition and in general terms, it is indirectly proportional to its viscosity. Dzikovski and Freed define it as “the variety of anisotropic motions which contribute to the mobility of components in the biological membrane” and is a measure of how easily molecules move in the membrane.[21] Various factors can impact it such as temperature, the chain length of phospholipids, their degree of saturation, and cholesterol. In general, increasing temperatures increase membrane fluidity. Short-chain saturated fatty acids decrease the melting/gel-to-fluid transition temperature, Tm, of phospholipid bilayers, are more susceptible to changes in kinetic energy, participate in fewer London dispersion forces than their long-chain counterparts, and therefore make the membrane more fluid.[22, 23] Unsaturated fatty acyl chains introduce “kinks” in the chain as pi bonds and form less stable van der Waals interactions with surrounding lipids than saturated chains, leading to more fluid membranes.[24] Cholesterol’s hydrophilic hydroxyl group aligns with the phosphate groups of phospholipids, and the hydrophobic steroid ring and hydrocarbon tail orient toward the phospholipid tails. It intercalates among phospholipids and is a bidirectional regulator or buffer of fluidity since it prevents the membrane from stiffening at low temperatures (steroid ring disrupts intermolecular interactions) and at high temperatures, cholesterol brings the phospholipids together. Several techniques are used to measure fluidity of a plasma membrane.

Some methods for measuring or studying the fluidity include electron spin resonance (ESR) spectroscopy, atomic force microscopy (AFM), deuterium nuclear magnetic resonance (^{2}H-NMR) spectroscopy, and fluorescence microscopy.[21] ESR involves studying the behavior of spin probes, and associated spectroscopic parameters may be connected to the degree of membrane fluidity.[25-27] AFM gives high-resolution images of surfaces with a spatial resolution of nanometers or less and elucidates structural features (such as lipid-disordered and lipid-ordered phases) and local changes of fluidity and elasticity in cell membranes.[28-32] Deuterium nuclear magnetic resonance spectral analyses (e.g. specific carbon-deuterium bond orientations in hydrophobic regions or arrangement of amphiphile molecules at certain temperatures) can give information on phase separations of a membrane, thereby characterizing its fluidity.[33-35] Fluorescence Correlation Spectroscopy can also be used to measure lateral diffusion coefficients of planar membranes on a micrometer scale and related to fluidity.[36-40] Of particular interest in the Blanchard research group is fluorescence microscopy. The rotational diffusion behavior and fluorescence lifetime of a fluorescent probe, obtained via fluorescence anisotropy decay imaging (FADI) and/or time-correlated single-photon counting (TCSPC) experiments, may be correlated to the fluidity of a monolayer or bilayer.[41-50] However, the FADI and TCSPC techniques yield information on the sub-micron scale, so in order to obtain translational diffusion coefficients of molecules in membranes on the micrometer to sub-millimeter scale, fluorescence recovery after photobleaching (FRAP) has been employed in this work, details of which are in the next chapter (Chapter 2: Experimental Techniques).

Artificial lipid membranes allow one to change different parameters and relate the results (such as changes in fluidity) to a biological plasma membrane. Ethanol and *n*-butanol have been shown to have general anesthetic properties[51, 52], and the Blanchard research group has experience with studying their applications on model lipid bilayers.[48-50] In this work, we perform translational diffusion measurements on solid supported lipid bilayers (SLBs) whose properties are well-controlled, and the results can be connected to the cell membrane.

The literature is replete with experiments on several kinds of artificial lipid bilayers, some of which are mentioned in Chapter 3. The reviews of Richter *et al*., Castellana *et al*., and Miller *et al*. detail potential mechanisms behind lipid bilayer formation on solid supports.[53-55] Briefly, key factors include the bilayer composition, nature of the support (such as glass and mica), and the aqueous environment. We prepared vesicle (also known as a liposome) solutions composed of cholesterol, sphingomyelin, ceramide, 1,2-dioleoyl-*sn*-phosphatidylcholine (DOPC), perylene, and/or 1,2-dioleoyl-*sn*-glycero-3-phosphoethanolamine-N-(lissamine rhodamine B sulfonyl) on freshly cleaved mica slides. In order to mimic a biological membrane, the pH of Tris® buffer was around 7.5 which is similar to the body's physiological pH. The phospholipid vesicles and substrate would be expected to have negative charges at pH 7.5.[55, 56] Repulsive forces compete against the van der Waals forces of attraction. Therefore, divalent cations such as Mg^{2+} or Ca^{2+} (Ca^{2+} used in this work) bridge the two negatively charged groups.[57] We prepared a 2 mM solution of $CaCl_2$ because that is the approximate concentration of Ca^{2+} in the extracellular space of biological membranes.[58, 59] Moreover, we observed that the $CaCl_2$ solution, when added to the cleaved mica surface first, helped with stability and reproducibility of translational diffusion measurements. Though we did not increase the ionic strength of aqueous solutions further, it might promote adsorption of lipid vesicles onto the substrate.[53-55] Ultimately, we wish to make a connection with live neuronal cell membranes by performing similar fluidity measurements. Fortunately, the Blanchard research group has a long-standing, ongoing collaboration with the Busik group in the physiology department at Michigan State University, hence giving us the opportunity to study the fluidity of live cell membranes.

The Busik research group aims to develop novel therapeutic options for diabetes-related retinal degradation by understanding the pathogenesis. Diabetes is commonly linked to hyperglycemia (high blood glucose levels) but can also be associated with dyslipidemia (abnormal levels of lipids in the blood - namely high levels of low-density lipoproteins, LDL , triglycerides, and cholesterol and low levels of high-density lipoproteins), both of which may lead to the development of sight threatening diabetic retinopathy (DR).[60, 61] Beta (β) cells are located in pancreatic islets and are responsible for producing insulin, which helps glucose reach and be used by different tissues. However, in type 1 diabetes, the beta cells are destroyed, so insulin is not produced. In type 2 diabetes, insulin is produced but cells in the body do not respond to it normally (insulin resistance) leading to elevated blood glucose levels. In both types, plasma lipid levels, lipid profiles, and fatty-acid composition are affected, and dyslipidemia is connected to DR.[61] This complication results from damage of blood vessels in the retina which can swell, leak, or close, all of which can lead to vision loss. Thus, of particular interest are bone-marrow derived circulating angiogenic cells (CAC) because they can migrate toward sites of endothelial injury and promote vascular repair, but their function is compromised in DR.[62-67] Studies by Chakravarthy *et al.* showed that CAC membrane fluidity is decreased in DR, likely from elevated LDL cholesterol.[68-71] Therefore, we hypothesized that increasing or rejuvenating the fluidity could help CACs function properly. CACs from non-diabetic (control), type 1, and type 2 patients as well as from mice were isolated and each was split in two groups: cells treated *ex-vivo* with the drug N, N-dimethyl-3β-hydroxycholenamide (DMHCA) or not treated for pairwise comparisons (Figure 1.3).

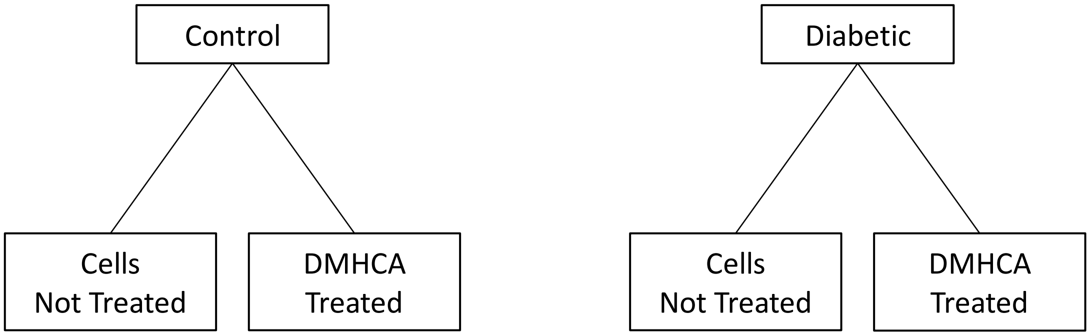

Figure 1.3. Flowchart of CAC Drug Treatment. Cells from control, type 1, and type 2 subjects were not treated or treated with DMHCA.

DMHCA is a synthetic oxysterol and a selective liver X receptor (LXR) agonist that acts as a cholesterol-lowering agent without promoting triglyceride synthesis.[72-74] It rejuvenates membrane fluidity in CACs, among positive pleiotropic effects, and has the potential to reduce inflammation in diabetes; therefore, DMHCA treatment has exciting potential in correcting the retinal and bone marrow dysfunction in type 2 diabetes, explained in Chapter 5. That work was recently accepted for publication in the *Journal of Clinical Investigation (JCI) Insight*. How general anesthetics work on the molecular level and how fluidity of diabetic cells can be measured using a new diagnostic tool are the key research questions investigated in this work.

We use the fluorescence recovery after photobleaching (FRAP) technique to measure the fluidity of planar supported lipid bilayers and circulating angiogenic cell membranes via translational diffusion constants, described in Chapter 2: Experimental Techniques. Upon application of ethanol and *n*-butanol (separately) to the aqueous overlayer of supported lipid bilayers, we notice a trend of diffusion coefficients increasing with concentration, then decreasing potentially due to a bilayer interdigitation phenomenon. The results and discussion are presented in Chapter 3: Effects of Ethanol and *n*-Butanol on Structural Composition of Supported Lipid Bilayers via Translational Diffusion. The data are indicative of a heterogenous nature of the planar SLB system which was corroborated with ceramide-based and rhodamine-based systems, molecules of which deviate from normal diffusion, explained in Chapter 4: Investigating Anomalous Diffusion in Heterogenous Supported Lipid Bilayers via Translational Diffusion. A connection between model membranes and live cell membranes was attempted by undertaking a collaborative project and using FRAP to measure translational diffusion coefficients of circulating angiogenic cells, mentioned in Chapter 5: Selective LXR agonist, DMHCA, corrects retinal and bone marrow dysfunction in type 2 diabetes. Though the results from SLB and CAC membrane fluidity experiments are different in detail, the results from both are connected on theoretical grounds and are complementary.

REFERENCES

REFERENCES

1. Singer, S. J.; Nicolson, G. L., The Fluid Mosaic Model of the Structure of Cell Membranes. *Science* **1972,** *175* (4023), 720-731.

2. https://www.uclahealth.org/anes/types-of-anesthesia Types of Anesthesia.

3. Allegri, M.; Delazzo, M. G.; Grossi, P.; Borghi, B., Efficacy of drugs in regional anesthesia: A review. *European Journal of Pain Supplements* **2009,** *3* (2), 41-48

4. Galeotti, A.; Bernardin, G. A.; D'Antò, V.; Ferrazzano, G. F.; Gentile, T.; Viarani, V.; Cassabgi, G.; Cantile, T., Inhalation Conscious Sedation with Nitrous Oxide and Oxygen as Alternative to General Anesthesia in Precooperative, Fearful, and Disabled Pediatric Dental Patients: A Large Survey on 688 Working Sessions. *Biomed Res Int* **2016,** *2016*, 1-6.

5. Antkowiak, B., How do general anaesthetics work? *Naturwissenschaften* **2001,** *88*, 201-213.

6. Overton, C. E., *Studien Über Die Narkose: Zugleich Ein Beitrag Zur Allgemeinen Pharmakologie*. Jena Fischer: 1901.

7. Krasowski, M. D., Contradicting a Unitary Theory of General Anesthetic Action: a History of Three Compounds from 1901 to 2001. *Bull Anesth Hist* **2003,** *21* (3), 1-13.

8. Butler, T. C.; Dickison, H. L., The Anesthetic Activity of Optical Antipodes I. The Secondary Butyl Alcohols. *J Pharmacol Exp Ther* **1940,** *69* (3), 225-228.

9. Butler, T. C., The Metabolic Fate of Chloral Hydrate. *J Pharmacol Exp Ther* **1948,** *92* (1), 49-58.

10. Franks, N. P.; Lieb, W. R., Where do general anaesthetics act? *Nature* **1978,** *274* (5669), 339-342.

11. Franks, N. P.; Lieb, W. R., Molecular and Cellular Mechanisms of General Anaesthesia. *Nature* **1994,** *367* (6464), 607-614.

12. Franks, N. P.; Lieb, W. R., Is Membrane Expansion Relevant to Anaesthesia? *Nature* **1981,** *292* (5820), 248-251.

13. Franks, N. P.; Lieb, W. R., Molecular Mechanisms of General Anaesthesia. *Nature* **1982,** *300* (5892), 487-493.

14. Franks, N. P.; Lieb, W. R., Partitioning of Long-Chain Alcohols Into Lipid Bilayers: Implications for Mechanisms of General Anesthesia. *Proc Natl Acad Sci U S A* **1986,** *83* (14), 5116-5120.

15. Darlison, M. G.; Albrecht, B. E., $GABA_A$receptor subtypes: which, where and why? *Seminars in Neuroscience* **1995,** *7* (2), 115-126

16. Garcia, P. S.; Kolesky, S. E.; Jenkins, A., General Anesthetic Actions on $GABA_A$ Receptors. *Curr Neuropharmacol* **2010,** *8* (1), 2-9.

17. Sonner, J. M.; Antognini, J. F.; Dutton, R. C.; Flood, P.; Gray, A. T.; Harris, R. A.; Homanics, G. E.; Kendig, J.; Orser, B.; Raines, D. E.; Rampil, I. J.; Trudell, J.; Vissel, B.; Eger, E. I., Inhaled Anesthetics and Immobility: Mechanisms, Mysteries, and Minimum Alveolar Anesthetic Concentration. *Anesth Analg* **2003,** *97* (3), 718-740.

18. Flood, P.; Ramirez-Latorre, J.; Role, L., Alpha 4 Beta 2 Neuronal Nicotinic Acetylcholine Receptors in the Central Nervous System Are Inhibited by Isoflurane and Propofol, but Alpha 7-type Nicotinic Acetylcholine Receptors Are Unaffected. *Anesthesiology* **1997,** *86* (4), 859-865.

19. Lin, L. H.; Chen, L. L.; Harris, R. A., Enflurane Inhibits NMDA, AMPA, and Kainate-Induced Currents in Xenopus Oocytes Expressing Mouse and Human Brain mRNA. *Federation of American Societies for Experimental Biology Journal* **1993,** *7* (5), 479-485.

20. Son, Y., Molecular mechanisms of general anesthesia. *Korean J Anesthesiol* **2010,** *59* (1), 3-8.

21. Dzikovski, B.; Freed, J., *Membrane Fluidity*. Springer: Berlin, Heidelberg, 2013.

22. Ibarguren, M.; López, D. J.; Escribá, P. V., The Effect of Natural and Synthetic Fatty Acids on Membrane Structure, Microdomain Organization, Cellular Functions and Human Health. *Biochim Biophys Acta* **2014,** *1838* (6), 1518-1528.

23. Maulucci, G.; Cohen, O.; Daniel, B.; Sansone, A.; Petropoulou, P. I.; Filou, S.; Spyridonidis, A.; Pani, G.; De Spirito, M.; Chatgilialoglu, C.; Ferreri, C.; Kypreos, K. E.; Sasson, S., Fatty Acid-Related Modulations of Membrane Fluidity in Cells: Detection and Implications. *Free Radic Res* **2016,** *50* (sup1), S40-S50.

24. Lodish, H.; Berk, A.; Zipursky, S. L.; Matsudaira, P.; Baltimore, D.; Darnell, J., *Biomembranes: Structural Organization and Basic Functions*. W. H. Freeman: New York, 2000.

25. Yawata, Y.; Sugihara, T.; Mori, M.; Nakashima, S.; Nozawa, Y., Lipid Analyses and Fluidity Studies by Electron Spin Resonance of Red Cell Membranes in Hereditary High Red Cell Membrane Phosphatidylcholine Hemolytic Anemia. *Blood* **1984,** *64* (5), 1129-1134.

26. Man, D.; Olchawa, R.; Kubica, K., Membrane Fluidity and the Surface Properties of the Lipid Bilayer: ESR Experiment and Computer Simulation. *J Liposome Res* **2010,** *20* (3), 211-218.

27. Man, D.; Olchawa, R., Dynamics of surface of lipid membranes: theoretical considerations and the ESR experiment. *European Biophysics Journal* **2017,** *46* (4), 325-334.

28. Chiantia, S.; Ries, J.; Kahya, N.; Schwille, P., Combined AFM and Two-Focus SFCS Study of Raft-Exhibiting Model Membranes. *Chemphyschem* **2006,** *7* (11), 2409-2418.

29. Galvanetto, N., Single-cell unroofing: probing topology and nanomechanics of native membranes. *Biochimica et Biophysica Acta (BBA) - Biomembranes* **2018,** *1860* (12), 2532-2538.

30. Matjaž, M. G.; Škarabot, M.; Gašperlin, M.; Janković, B., Lamellar Liquid Crystals Maintain Keratinocytes' Membrane Fluidity: An AFM Qualitative and Quantitative Study. *Int J Pharm* **2019,** *572*, 1-11.

31. Sarangi, N. K.; Ayappa, K. G.; Visweswariah, S. S.; Basu, J. K., Nanoscale Dynamics of Phospholipids Reveals an Optimal Assembly Mechanism of Pore-Forming Proteins in Bilayer Membranes. *Phys Chem Chem Phys* **2016,** *18* (43), 29935-29945.

32. Muller, D. J., AFM: A Nanotool in Membrane Biology. *Biochemistry* **2008,** *47* (31), 7986-7998.

33. Dazzoni, R.; Grélard, A.; Morvan, E.; Bouter, A.; Applebee, C. J.; Loquet, A.; Larijani, B.; Dufourc, E. J., The Unprecedented Membrane Deformation of the Human Nuclear Envelope, in a Magnetic Field, Indicates Formation of Nuclear Membrane Invaginations. *Sci Rep* **2020,** *10* (1), 1-14.

34. Gómez-Murcia, V.; Torrecillas, A.; de Godos, A. M.; Corbalán-García, S.; Gómez-Fernández, J. C., Both Idebenone and Idebenol Are Localized Near the Lipid-Water Interface of the Membrane and Increase Its Fluidity. *Biochim Biophys Acta* **2016,** *1858* (6), 1071-1081.

35. Filippelli, L.; Rossi, C. O.; Uccella, N. A., E, Z and Positional-Monoenoic Phyto-Fatty Acids Influencing Membrane Fluidity: DSC and NMR Experiments. *Colloids Surf B Biointerfaces* **2011,** *82* (1), 13-17.

36. Machán, R.; Hof, M., Lipid Diffusion in Planar Membranes Investigated by Fluorescence Correlation Spectroscopy. *Biochim Biophys Acta* **2010,** *1798* (7), 1377-1391.

37. Macháň, R.; Hof, M., Recent Developments in Fluorescence Correlation Spectroscopy for Diffusion Measurements in Planar Lipid Membranes. *Int J Mol Sci* **2010,** *11* (2), 427-457.

38. Petrov, E. P.; Schwille, P., *State of the Art and Novel Trends in Fluorescence Correlation Spectroscopy*. Springer-Verlag: Berlin Heidelberg, 2008; Vol. 6.

39. Guo, L.; Har, J. Y.; Sankaran, J.; Hong, Y.; Kannan, B.; Wohland, T., Molecular Diffusion Measurement in Lipid Bilayers Over Wide Concentration Ranges: A Comparative Study. *Chemphyschem* **2008,** *9* (5), 721-728.

40. Heinemann, F.; Betaneli, V.; Thomas, F. A.; Schwille, P., Quantifying Lipid Diffusion by Fluorescence Correlation Spectroscopy: A Critical Treatise. *Langmuir* **2012,** *28* (37), 13395-13404.

41. Dominska, M.; Mazur, M.; Greenough, K. P.; Koan, M. M.; Krysiński, P. G.; Blanchard, G. J., Probing Organization and Communication at Layered Interfaces. *Bioelectrochemistry* **2007,** *70* (2), 421-434.

42. Domińska, M.; Krysiński, P.; Blanchard, G. J., Interrogating Interfacial Organization in Planar Bilayer Structures. *Langmuir* **2008,** *24* (16), 8785–8793.

43. Greiner, A. J.; Pillman, H. A.; Worden, R. M.; Blanchard, G. J.; Ofoli, R. Y., Effect of Hydrogen Bonding on the Rotational and Translational Dynamics of a Headgroup-Bound Chromophore in Bilayer Lipid Membranes. *J Phys Chem B* **2009,** *113* (40), 13263-13268.

44. Kijewska, K.; Blanchard, G. J., Using Diffusion To Characterize Interfacial Heterogeneity. *Langmuir* **2017,** *33* (5), 1155-1161.

45. Lapinski, M. M.; Blanchard, G. J., The Role of Phospholipid Headgroups in Mediating Bilayer Organization. Perturbations Induced by the Presence of a Tethered Chromophore. *Chem Phys Lipids* **2007,** *150* (1), 12-21.

46. Lapinski, M. M.; Blanchard, G. J., Interrogating the role of liposome size in mediating the dynamics of a chromophore in the acyl chain region of a phospholipid bilayer. *Chem. Phys. Lipids* **2008,** *153*, 130-137.

47. Mize, H. E.; Blanchard, G. J., Interface-Mediation of Lipid Bilayer Organization and Dynamics. *Phys Chem Chem Phys* **2016,** *18* (25), 16977-16985.

48. Pillman, H. A.; Blanchard, G. J., Effects of Ethanol on the Organization of Phosphocholine Lipid Bilayers. *Journal of Physical Chemistry B* **2010,** *114*, 3840-3846.

49. Setiawan, I.; Blanchard, G. J., Ethanol-Induced Perturbations to Planar Lipid Bilayer Structures. *J. Phys. Chem. B* **2014,** *118*, 537-546.

50. Setiawan, I.; Blanchard, G. J., Structural Disruption of Phospholipid Bilayers over a Range of Length Scales by n-Butanol. *J. Phys. Chem. B* **2014,** *118*, 3085-3093.

51. Wong, S. M. E.; Fong, E.; Tauck, D. L.; Kendig, J. J., Ethanol as a General Anesthetic: Actions in Spinal Cord. *European Journal of Pharmacology* **1997,** *329*, 121-127.

52. Fang, Z.; Ionescu, P.; Chortkoff, B. S.; Kandel, L.; Sonner, J.; Laster, M. J.; Eger, E. I., Anesthetic Potencies of N-Alkanols: Results of Additivity and Solubility Studies Suggest a Mechanism of Action Similar to That for Conventional Inhaled Anesthetics. *Anesth Analg* **1997,** *84* (5), 1042-1048.

53. Richter, R. P.; Bérat, R.; Brisson, A. R., Formation of Solid-Supported Lipid Bilayers: An Integrated View. *Langmuir* **2006,** *22* (8), 3497–3505.

54. Castellana, E. T.; Cremer, P. S., Solid supported lipid bilayers: From biophysical studies to sensor design. *Surface Science Reports* **2006,** *61* (10), 429-444.

55. Miller, E.; Stubbington, L.; Dinet, C.; Staykova, M., Biophysical insights from supported lipid patches. *Advances in Biomembranes and Lipid Self-Assembly* **2019,** *29*, 23-48.

56. Marsh, D., *CRC Handbook of Lipid Bilayers*. Boca Raton, FL, 1990.

57. Richter, R.; Mukhopadhyay, A.; Brisson, A., Pathways of Lipid Vesicle Deposition on Solid Surfaces: A Combined QCM-D and AFM Study. *Biophys J* **2003,** *85* (5), 3035-3047.

58. Melcrová, A.; Pokorna, S.; Pullanchery, S.; Kohagen, M.; Jurkiewicz, P.; Hof, M.; Jungwirth, P.; Cremer, P. S.; Cwiklik, L., The Complex Nature of Calcium Cation Interactions With Phospholipid Bilayers. *Sci Rep* **2016,** *6* (38035), 1-12.

59. Xu, N.; Francis, M.; Cioffi, D. L.; Stevens, T., Studies on the Resolution of Subcellular Free Calcium Concentrations: A Technological Advance. Focus on "Detection of Differentially Regulated Subsarcolemmal Calcium Signals Activated by Vasoactive Agonists in Rat Pulmonary Artery Smooth Muscle Cells". *Am J Physiol Cell Physiol* **2014,** *306* (7), C636-C638.

60. Goldberg, I. J., Diabetic Dyslipidemia: Causes and Consequences. *J Clin Endocrinol Metab* **2001,** *86* (3), 965-971.

61. Busik, J. V.; Esselman, W. J.; Reid, G. E., Examining the Role of Lipid Mediators in Diabetic Retinopathy. *Clinical Lipidology* **2012,** *7* (6), 661-675.

62. Loomans, C. J.; de Koning, E. J.; Staal, F. J.; Rookmaaker, M. B.; Verseyden, C.; de Boer, H. C.; Verhaar, M. C.; Braam, B.; Rabelink, T. J.; van Zonneveld, A. J., Endothelial Progenitor Cell Dysfunction: A Novel Concept in the Pathogenesis of Vascular Complications of Type 1 Diabetes. *Diabetes* **2004,** *53* (1), 195-199.

63. Tikhonenko, M.; Lydic, T. A.; Opreanu, M.; Li Calzi, S.; Bozack, S.; McSorley, K. M.; Sochacki, A. L.; Faber, M. S.; Hazra, S.; Duclos, S.; Guberski, D.; Reid, G. E.; Grant, M. B.; Busik, J. V., N-3 Polyunsaturated Fatty Acids Prevent Diabetic Retinopathy by Inhibition of Retinal Vascular Damage and Enhanced Endothelial Progenitor Cell Reparative Function. *PLoS One* **2013,** *8* (1), e55177.

64. Segal, M. S.; Shah, R.; Afzal, A.; Perrault, C. M.; Chang, K.; Schuler, A.; Beem, E.; Shaw, L. C.; Li Calzi, S.; Harrison, J. K.; Tran-Son-Tay, R.; Grant, M. B., Nitric Oxide Cytoskeletal-Induced Alterations Reverse the Endothelial Progenitor Cell Migratory Defect Associated With Diabetes. *Diabetes* **2006,** *55* (1), 102-109.

65. Shaw, L. C.; Neu, M. B.; Grant, M. B., Cell-based Therapies for Diabetic Retinopathy. *Curr Diab Rep* **2011,** *11* (4), 265-274.

66. Kim, C.; Schneider, G.; Abdel-Latif, A.; Mierzejewska, K.; Sunkara, M.; Borkowska, S.; Ratajczak, J.; Morris, A. J.; Kucia, M.; Ratajczak, M. Z., Ceramide-1-phosphate regulates migration of multipotent stromal cells (MSCs) and endothelial progenitor cells (EPCs) – implications for tissue regeneration. *Stem Cells* **2013,** *31* (3), 500-510.

67. Tongers, J.; Roncalli, J. G.; Losordo, D. W., Therapeutic Angiogenesis for Critical Limb Ischemia: Microvascular Therapies Coming of Age. *Circulation* **2008,** *118* (1), 9-16.

68. Chakravarthy, H.; Navitskaya, S.; O'Reilly, S.; Gallimore, J.; Mize, H.; Beli, E.; Wang, Q.; Kady, N.; Huang, C.; Blanchard, G. J.; Grant, M. B.; Busik, J. V., Role of Acid

Sphingomyelinase in Shifting the Balance Between Proinflammatory and Reparative Bone Marrow Cells in Diabetic Retinopathy. *Stem Cells* **2016,** *34* (4), 972-983.

69. Chew, E. Y.; Ambrosius, W. T.; Davis, M. D.; Danis, R. P.; Gangaputra, S.; Greven, C. M.; Hubbard, L.; Esser, B. A.; Lovato, J. F.; Perdue, L. H.; Goff, D. C.; Cushman, W. C.; Ginsberg, H. N.; Elam, M. B.; Genuth, S.; Gerstein, H. C.; Schubart, U.; Fine, L. J., Effects of Medical Therapies on Retinopathy Progression in Type 2 Diabetes. *The New England Journal of Medicine* **2010,** *363* (3), 233-244.

70. Bryszewska, M.; Watała, C.; Torzecka, W., Changes in Fluidity and Composition of Erythrocyte Membranes and in Composition of Plasma Lipids in Type I Diabetes. *Br J Haematol* **1986,** *62* (1), 111-116.

71. Kruit, J. K.; Wijesekara, N.; Fox, J. E. M.; Dai, X. Q.; Brunham, L. R.; Searle, G. J.; Morgan, G. P.; Costin, A. J.; Tang, R.; Bhattacharjee, A.; Johnson, J. D.; Light, P. E.; Marsh, B. J.; MacDonald, P. E.; Verchere, C. B.; Hayden, M. R., Islet Cholesterol Accumulation Due to Loss of ABCA1 Leads to Impaired Exocytosis of Insulin Granules. *Diabetes* **2011,** *60* (12), 3186-3196.

72. Quinet, E. M.; Savio, D. A.; Halpern, A. R.; Chen, L.; Miller, C. P.; Nambi, P., Gene-selective Modulation by a Synthetic Oxysterol Ligand of the Liver X Receptor. *J Lipid Res* **2004,** *45* (10), 1929-1942.

73. Lund, E. G.; Peterson, L. B.; Adams, A. D.; Lam, M. H.; Burton, C. A.; Chin, J.; Guo, Q.; Huang, S.; Latham, M.; Lopez, J. C.; Menke, J. G.; Milot, D. P.; Mitnaul, L. J.; Rex-Rabe, S. E.; Rosa, R. L.; Tian, J. Y.; Wright, S. D.; Sparrow, C. P., Different Roles of Liver X Receptor Alpha and Beta in Lipid Metabolism: Effects of an Alpha-Selective and a Dual Agonist in Mice Deficient in Each Subtype. *Biochem Pharmacol* **2006,** *71* (4), 453-463.

74. Miao, B.; Zondlo, S.; Gibbs, S.; Cromley, D.; Hosagrahara, V. P.; Kirchgessner, T. G.; Billheimer, J.; Mukherjee, R., Raising HDL Cholesterol Without Inducing Hepatic Steatosis and Hypertriglyceridemia by a Selective LXR Modulator. *J Lipid Res* **2004,** *45* (8), 1410-1417.

CHAPTER 2: EXPERIMENTAL TECHNIQUES

Supported Lipid Bilayers

Vesicle constituents are provided in Table 2.1 as an example, and mole percentages may be adjusted accordingly based on a total of 4.0×10^{-6} moles. Tris® buffer (8 mM Tris® HCl, 2 mM Tris® base, milli Q H_2O, pH 7.5) was added for a total lipid concentration of 1 mg/mL (or 4 mM). For instance, a total lipid mass of 2.66 mg needed 2.66 mL of Tris® buffer.

Table 2.1. Membrane Components presented with their Mole Percentages and Volume in Chloroform. DOPC stands for 1,2-dioleoyl-*sn*-phosphatidylcholine and DOPE is 1,2-dioleoyl-*sn*-glycero-3-phosphoethanolamine.

Molecule	Mole Percent (%)	Moles	Volume (μL)
Cholesterol	10	4.0×10^{-7}	31
DOPC	47	1.9×10^{-6}	148
Sphingomyelin	20	8.0×10^{-7}	56
Ceramide	20	8.0×10^{-7}	86
Perylene	3	1.2×10^{-7}	30
Rhodamine-DOPE	1	4.0×10^{-8}	52

Vesicle preparation, formation, extrusion, and deposition/fusion on supported lipid bilayers (SLBs) are elucidated in detail in subsequent chapters. SLBs were characterized by Dynamic Light Scattering and Fluorescence Recovery after Photobleaching experiments (*vide infra*).

Dynamic Light Scattering Measurements

Dynamic Light Scattering (DLS), also known as Photon Correlation Spectroscopy or Quasi-Elastic Light Scattering, is a non-invasive technique used to measure the particle size distribution of particles typically in the sub-micron region in solution, undergoing Brownian motion.[1, 2] Monochromatic light, usually from a laser, is incident on a sample and scattered light interferes constructively or destructively. The fluctuations in light intensities are recorded as a function of time and are related directly to the translational diffusion coefficient, D, of the molecules in solution via an autocorrelation function, which in turn yields the particle size, r (hydrodynamic radius), through the Stokes-Einstein relation:

$$D = \frac{k_B T}{6\pi\eta r}$$

where η is the viscosity of the solvent.

Instrument and Software Settings

DLS measurements were obtained at 25 ºC using a Malvern Zetasizer Nano ZS which determines vesicle size distribution. The instrument was equipped with a 633-nm He-Ne laser and given a 30-min warm up time before use. Disposable UV cuvettes were used and filled to the appropriate line, indicating a 1-mL volume. Zetasizer Software v 6.20 accompanied the instrument and settings selected were: Measure, Manual, Measurement Type - Size, Material DOPC (refractive index of 1.590, absorption of 0.01), water was the dispersant (temperature 25 ºC, viscosity 0.8872 cP, RI 1.330), Temperature 25.0 ºC, Equilibration time 120 seconds, Cell type ZEN0112 low volume disposable sizing cuvette, Measurement duration: 'No' for extending duration for large particles, Positioning method: 'Seek for optimum position,' Automatic attenuation selection: Yes. Once measurements are complete, multiple files may be selected, and the particle size distributions may be viewed in the Intensity PSD (M) tab and saved.

Human Circulating Angiogenic Cell Staining

Perylene dye solution was prepared by dissolving 2 mg of perylene (Sigma Aldrich) in 8 mL of dimethyl sulfoxide DMSO (Sigma Aldrich) such that its concentration was 1 mM. It was filtered into a sterile 50-mL tube and 200-mL aliquots were transferred to sterile 1-mL Eppendorf tubes, stored in a freezer. The samples with *ca.* 25,000 isolated circulating angiogenic cells were stained with an amount commensurate with approximately 1-4 percent of the total volume. For instance, 1-2 μL of perylene solution (at 37 °C) were pipetted into 50 μL of sample, mixed, and kept in an incubator for 10 min. If there were 1000 μL of sample (typically for samples treated with a drug), 10 μL of perylene were pipetted instead, mixed, kept in incubator for 10 min, centrifuged (0.8 or 1 x 10^3 G, 10 min, 20 °C, Fisher Scientific AccuSpin Micro 17R), and 800 μL of supernatant were removed. The stained samples, in Eppendorf tubes, were placed in floating foams in a beaker with 37 °C-water and transferred to a laser instrument room for fluidity measurements, utilizing fluorescence recovery after photobleaching (FRAP) technique. The beaker assembly was set on a hot plate at the lowest heat setting with periodic monitoring of the temperature. A 0.8-μL aliquot was pipetted on a microscope slide (Thermo Scientific plain microscope slides, precleaned, 25 x 75 mm x 1 mm thick) and a cover-glass was placed on top (Corning, 22 x 22 mm of 1 mm thickness). The assembly was turned upside down and positioned on the flat stage of the FRAP instrument (*vide infra*).

Mouse Circulating Angiogenic Cell Staining

Perylene dye solution was prepared by dissolving 20 mg of perylene (Sigma Aldrich) in 8 mL of dimethyl sulfoxide DMSO (Sigma Aldrich) and stirred for at least five hours, such that its concentration was 10 mM. The solution was filtered into a sterile 50-mL tube and 100-mL aliquots were transferred to sterile 1-mL Eppendorf tubes, stored in a freezer. Each sample of isolated circulating angiogenic cells was adjusted to a total volume of ~100 μL with Hanks' Balanced Salt Solution (HBSS) (Sigma Aldrich). Thereafter, 3 μL of 10 mM thawed perylene solution (37 °C) was pipetted in and mixed to stain the cell membranes, for a final concentration of ~300 μM and incubated for 10 min. The suspension was centrifuged (10^3 G, 1 min, 20 °C, Eppendorf^{TM} Centrifuge 5425), and supernatant was removed carefully - ensuring the pellet remained unperturbed. About 20 μL HBSS was added to ensure multiple trials for fluidity measurements (*vide infra*). The stained samples, in Eppendorf^{TM} tubes, were placed in floating foams in a beaker with 37 °C-water and transferred to a laser instrument room for fluidity measurements. The beaker assembly was set on a hot plate at the lowest heat setting with periodic monitoring of the temperature. A 1-μL aliquot was pipetted on a microscope slide (Thermo Scientific plain microscope slides, precleaned, 25 x 75 mm x 1 mm thick) and a cover-glass was placed on top (Corning, 22 x 22 mm of 1 mm thickness). The assembly was turned upside down and positioned on the flat stage of the FRAP instrument.

Absorption and emission spectra of vesicle-containing solutions were too dilute and inadequate due to low volumes (approximately 1 mL). Therefore, absorption and emission spectra of perylene and rhodamine in the literature were used for guidance.[3, 4] Specifically, perylene was excited with 405-nm light and emitted around 480 nm, while rhodamine's λ_{ex} was 561 nm and emitted around $\lambda_{em} \sim 630$ nm during fluorescence recovery after photobleaching experiments. The instrument settings are described below.

UV-Visible Absorption

UV-Visible Absorption measurements were obtained using a Shimadzu UV-2600 Spectrophotometer. The system was given a few minutes to warm up before use, and two cuvettes were used with the reference located in the back compartment. The UVProbe 2.60 software was used in Spectrum mode to collect spectra, scanned from long to short wavelength, in automatic sampling intervals, with a baseline collected for the solvent.

Fluorescence

Fluorescence measurements were performed on a Jobin Yvon Horiba FluoroLog-3 Spectrofluorometer. The SpectrAcq computer system for data collection had to be turned off before proceeding, in order to avoid damaging it. The lamp power supply was turned on which starts a cooling fan, 30 seconds elapsed, and the “Main Lamp” switch was turned on. It was then safe to turn on the SpectrAcq computer which took ~1 minute to boot up. The Instrument Control Center (v 2.2.9.1, Copyright © 2000 Jobin Yvon, Inc.) software was used to collect emission scans, which required collection wavelength range, wavelength increment, integration time, and excitation wavelength values.

Measuring Translational Diffusion with Fluorescence Recovery After Photobleaching

The fluorescence recovery after photobleaching (FRAP) microscopy technique was developed in the 1970s[5-8] and regained prominence from the development of green fluorescence protein as a fluorescent label[9-14]. FRAP is used to characterize the mobility of fluorescent molecules at the micrometer scale. Specifically, the two-dimensional translational diffusion of a fluorescent probe may be obtained and related to the diffusion of the system of interest, such as a plasma membrane, proteins within, or artificial lipid bilayers.[15-21] The fluorescence intensity of a small area in a fluorescing region, also known as the region of interest (ROI), is first measured for a baseline (pre-bleach). Then, the spot is transiently photobleached by a high-intensity laser beam (stimulation) which causes molecules within that region to undergo irreversible loss of fluorescence (Figure 2.1). The ROI is continuously monitored as a function of time by a significantly attenuated beam (to prevent further bleaching), which results in a fluorescence recovery curve over time due to surrounding fluorophores diffusing into the region, while photobleached ones diffuse out. Other ROIs may be selected for reference and background measurements. An example of a cell undergoing the process is shown in Figure 2.2.

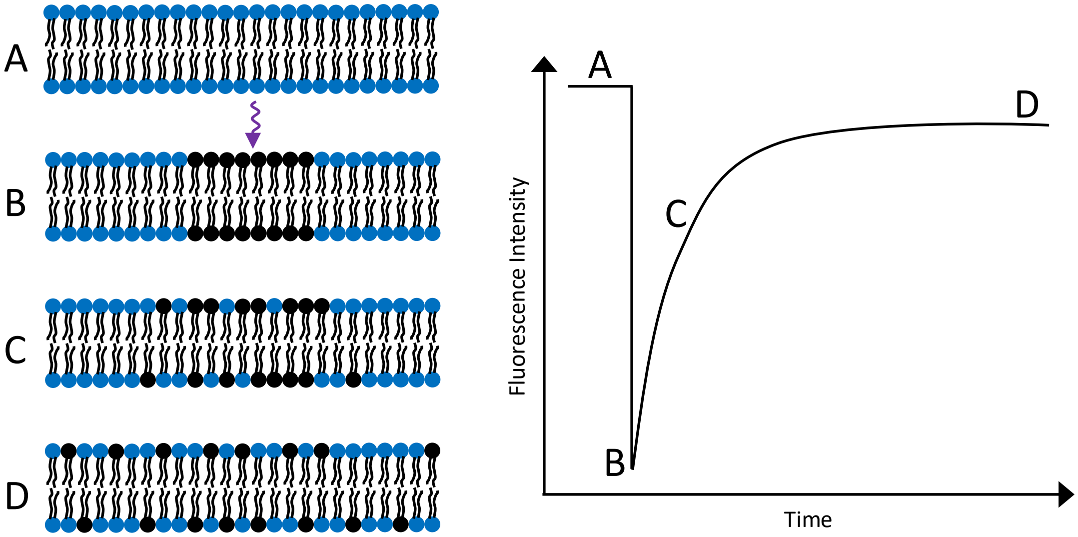

Figure 2.1. Illustration of Fluorescence Recovery after Photobleaching in a Simplified Lipid Bilayer. The bilayer is labeled with fluorophores (A), molecules in a region of interest are photobleached (B), and bleached and fluorescent molecules are exchanged over time (C, D).

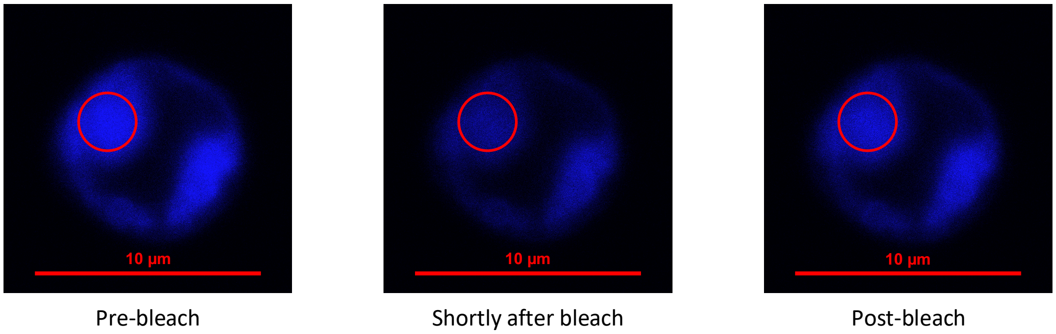

Pre-bleach

Shortly after bleach

Post-bleach

Figure 2.2. Images of a Cell during a Fluorescence Recovery after Photobleaching Measurement. The region of interest is photobleached, causing that spot to appear darker and as the surrounding perylene molecules diffuse into the ROI, the fluorescence intensity recovers.

The diffusion of particles undergoing Brownian motion may be described by the Einstein relation[17, 22]

$$D = \mu k_B T$$

where μ is the “mobility” of a particle and is inversely related to the friction coefficient f[23]

$$\mu = \frac{1}{f}$$

and

$$f = 6\pi\eta r$$

where η is the viscosity of the medium and r is the radius of the particle (assumed to be spherical). Therefore, we get the Stokes-Einstein equation

$$D = \frac{k_B T}{6\pi\eta r}$$

Diffusion may be classified as normal (Fickian) or anomalous (non-Fickian), explained in more detail in Chatper 3: Investigating Anomalous Diffusion in Heterogenous Supported Lipid Bilayers via Translational Diffusion.

A curve-fitting equation is then used to extract desired parameters, such as the recovery time constant and diffusion coefficient. Several models exist depending on the extent to which the fluorescent probe binds to the support, such as the reaction dominant (slow binding compared to diffusion and measurement period), pure diffusion (free diffusion and non-existent binding), and full-reaction diffusion (fast and relatively weak binding) models.[24, 25] The pure diffusion model was used in this work, where we assume the fluorescent probe (perylene) diffuses freely and there is no binding to the mica substrate. Thus, fluorescence recovery may be modeled by the equation derived by Soumpasis, from which the characteristic diffusion time τ_D may be extracted[25]

$$f(t) = e^{-\frac{\tau_D}{2t}}\left[I_o\left(\frac{\tau_D}{2t}\right) + I_1\left(\frac{\tau_D}{2t}\right)\right]$$

where I_o and I_1 are modified Bessel functions of the first kind and ω is the radius of the circular beam.

The translational diffusion constant can then be calculated from the equation below

$$D = \frac{\omega^2}{4\tau_D}$$

Instrumentation

The system rests on a flat laser table and is comprised of an inverted confocal laser scanning microscope (Nikon C2+). The microscope has a LED illuminator to acquire steady state fluorescence images, high-speed galvano scanners for precision and high-definition imaging, a motorized stage controlled with a joystick, objectives of 10X, 20X, 40X, 60X, and 100X magnification (Nikon), and a 3 PMT detector (400-700 nm). A laser system excites at 405, 488, 561, and 640 nm with 4′,6-diamidino-2-phenylindole (DAPI), fluorescein isothiocyanate (FITC), sulforhodamine 101 acid chloride (Texas Red), and cyanine 5 (Cy5), respectively. In the following chapters, perylene and rhodamine-tethered lipids were excited by the 405 and 561-nm lasers, respectively.

Software Settings

For cell membranes:

The system was accompanied by the NIS-Elements Acquisition imaging software (v 4.30). For cell membrane fluidity measurements, software settings consisted of pixel dwell 1.9, size 512, normal, DAPI checked, HV between 90-145 (typically ~125), offset of 10, and laser power 0.71. The 40X objective was used to locate cells and region of interest (ROI) was either 3 or 2 µm diameter for human or mouse samples, respectively, one used as the stimulating spot and the other as a standard, placed in a dark, non-fluorescent spot. The dimensions of the slightly oblong circulating angiogenic cell may be measured and usually have ~8 µm diameter. A continuous scanning time measurement was performed to ensure the cell did not move, indicated by a constant fluorescent intensity value over time. There was 1 minute of data acquisition (for 61 loops) at 1 sec intervals, bleaching for 1 second (4 loops) with no delay in intervals, and acquisition for another 5 min (301 loops) at 1 sec intervals. Data were saved as Microsoft Excel spreadsheets and fit using IGOR Pro software (WaveMetrics Inc.), with code courtesy of Dr. Yan Levitsky.

For supported lipid bilayers:

The supported lipid bilayer assembly was placed on the flat stage and 10X objective used with focal plane height of roughly 5,000 µm. Key settings included ROI diameters of 10, 20, or 30 µm diameter, one used as the stimulating spot and the other as a reference, placed over the whole region which encompassed the stimulating ROI as well. A continuous scanning time measurement was performed to ensure the bilayer was not moving too much for a measurement, indicated by a constant fluorescent intensity value over time. There was 1 minute of data acquisition (for 61 loops) at 1 sec intervals, bleaching for 1 second (4 loops) with no delay in intervals, and acquisition for another 5 min (301 loops) at 1 sec intervals. Data were saved as Microsoft Excel spreadsheets and fit using MATLAB (MathWorks ®), with code courtesy of Dr. Stephen Baumler.

REFERENCES

REFERENCES

1. Palmieri, V.; Lucchetti, D.; Gatto, I.; Maiorana, A.; Marcantoni, M.; Maulucci, G.; Papi, M.; Pola, R.; De Spirito, M.; Sgambato, A., Dynamic light scattering for the characterization and counting of extracellular vesicles: a powerful noninvasive tool. *Journal of Nanoparticle Research* **2014,** *16* (9), 1-8.

2. Stetefeld, J.; McKenna, S. A.; Patel, T. R., Dynamic light scattering: a practical guide and applications in biomedical sciences. *Biophysical Reviews* **2016,** *8* (4), 409-427.

3. Pillman, H. A.; Blanchard, G. J., Effects of Ethanol on the Organization of Phosphocholine Lipid Bilayers. *Journal of Physical Chemistry B* **2010,** *114*, 3840-3846.

4. Setiawan, I.; Blanchard, G. J., Ethanol-Induced Perturbations to Planar Lipid Bilayer Structures. *J. Phys. Chem. B* **2014,** *118*, 537-546.

5. Axelrod, D.; E., K. D.; Schlessinger, J.; Elson, E.; Webb, W. W., Mobility Measurement by Analysis of Fluorescence Photobleaching Recovery Kinetics. *Biophys. J.* **1976,** *16*, 1055-1069.

6. Elson, E. L.; Schlessinger, J.; Koppel, D. E.; Axelrod, D.; Webb, W. W., Measurement of Lateral Transport on Cell Surfaces. *Prog Clin Biol Res* **1976,** *9*, 137-147.

7. Jacobson, K.; Derzko, Z.; Wu, E. S.; Hou, Y.; Poste, G., Measurement of the Lateral Mobility of Cell Surface Components in Single, Living Cells by Fluorescence Recovery After Photobleaching. *J Supramol Struct* **1976,** *5* (4), 565-576.

8. Schlessinger, J.; Koppel, D. E.; Axelrod, D.; Jacobson, K.; Webb, W. W.; Elson, E. L., Lateral Transport on Cell Membranes: Mobility of Concanavalin A Receptors on Myoblasts. *Proc Natl Acad Sci U S A* **1976,** *73* (7), 2409-2413.

9. Reits, E. A.; Neefjes, J. J., From Fixed to FRAP: Measuring Protein Mobility and Activity in Living Cells. *Nat Cell Biol* **2001,** *3* (6), E145-147.

10. Lippincott-Schwartz, J.; Patterson, G. H., Development and Use of Fluorescent Protein Markers in Living Cells. *Science* **2003,** *300* (5616), 87-91.

11. Lippincott-Schwartz, J.; Altan-Bonnet, N.; Patterson, G. H., Photobleaching and Photoactivation: Following Protein Dynamics in Living Cells. *Nat Cell Biol* **2003**, S7-14.

12. Pucadyil, T. J.; Chattopadhyay, A., Confocal Fluorescence Recovery After Photobleaching of Green Fluorescent Protein in Solution. *J Fluoresc* **2006,** *16* (1), 87-94.

13. Zheng, C. Y.; Petralia, R. S.; Wang, Y. X.; Kachar, B., Fluorescence Recovery After Photobleaching (FRAP) of Fluorescence Tagged Proteins in Dendritic Spines of Cultured Hippocampal Neurons. *J Vis Exp* **2011,** (50), 1-3.

14. Lippincott-Schwartz, J.; Snapp, E. L.; Phair, R. D., The Development and Enhancement of FRAP as a Key Tool for Investigating Protein Dynamics. *Biophysical Journal* **2018,** *115* (7), 1146-1155.

15. Ishikawa-Ankerhold, H.; Ankerhold, R.; Drummen, G., *Encyclopedia of Life Sciences*. John Wiley & Sons, Ltd.: Chichester, 2014.

16. Meddens, M. B. M.; Keijzer, S.; Cambi, A., High Spatiotemporal Bioimaging Techniques to Study the Plasma Membrane Nanoscale Organization. *Fluorescence Microscopy* **2014**, 49-63.

17. Lorén, N.; Hagman, J.; Jonasson, J. K.; Deschout, H.; Bernin, D.; Cella-Zanacchi, F.; Diaspro, A.; McNally, J. G.; Ameloot, M.; Smisdom, N.; Nydén, M.; Hermansson, A. M.; Rudemo, M.; Braeckmans, K., Fluorescence Recovery After Photobleaching in Material and Life Sciences: Putting Theory Into Practice. *Q Rev Biophys* **2015,** *48* (3), 323-387.

18. Lakowicz, J. R., *Principles of Fluorescence Spectroscopy*. 3rd ed.; Springer: New York, 2006.

19. Wolf, D. E., Theory of fluorescence recovery after photobleaching measurements on cylindrical surfaces. *Biophys J* **1992,** *61* (2), 487-493.

20. Braeckmans, K.; Peeters, L.; Sanders, N. N.; De Smedt, S. C.; Demeester, J., Three-dimensional Fluorescence Recovery After Photobleaching With the Confocal Scanning Laser Microscope. *Biophysical Journal* **2003,** *85* (4), 2240-2252.

21. Lopez, A.; Dupou, L.; Altibelli, A.; Trotard, J.; Tocanne, J. F., Fluorescence Recovery After Photobleaching (FRAP) Experiments Under Conditions of Uniform Disk Illumination. Critical Comparison of Analytical Solutions, and a New Mathematical Method for Calculation of Diffusion Coefficient D. *Biophysical Journal* **1988,** *53* (6), 963-970.

22. Einstein, A., Über die von der molekularkinetischen Theorie der Wärme geforderte Bewegung von in ruhenden Flüssigkeiten suspendierten Teilchen. *Annalen der Physik* **1905,** *17*, 549–560.

23. Green, P., *Kinetics, Transport and Structure in Hard and Soft Materials*. CRC Press: New York, 2005.

24. Sprague, B. L.; Pego, R. L.; Stavreva, D. A.; McNally, J. G., Analysis of Binding Reactions by Fluorescence Recovery After Photobleaching. *Biophysical Journal* **2004,** *86* (6), 3473-3495.

25. Soumpasis, D. M., Theoretical analysis of fluorescence photobleaching recovery experiments. *Biophys. J.* **1983,** *41*, 95-97.

CHAPTER 3: EFFECTS OF ETHANOL AND N-BUTANOL ON STRUCTURAL COMPOSITION OF SUPPORTED LIPID BILAYERS VIA TRANSLATIONAL DIFFUSION

Abstract

The aim of the work was to understand how general anesthetics, such as short-chain alcohols, interact with the biological plasma membrane on the molecular level. Specifically, we studied the effects of varying concentrations of ethanol and *n*-butanol on the fluidity of planar mica supported lipid bilayers. The bilayer was composed of 1,2-dioleoyl-*sn*-phosphatidylcholine (DOPC), cholesterol, sphingomyelin, and perylene. Vesicle solutions were characterized by dynamic light scattering which gives particle size distributions; the average particle diameter was 133 nm. Translational diffusion constants were obtained utilizing the fluorescence recovery after photobleaching (FRAP) technique on the micrometer scale, and data were representative of a heterogeneous system. Overall, the diffusion constants increased with ethanol concentration, then decreased, and the structure appeared to have degraded in the vicinity of 0.8 M. A similar trend was observed for *n*-butanol but at lower concentrations owing to a longer aliphatic chain interacting to a greater extent with phospholipid tails; moreover, the integrity of the structure appeared to have deteriorated around 0.4 M. The results are consistent with a bilayer interdigitation phenomenon which could indirectly affect the function of integral membrane proteins, inducing anesthesia.

Introduction

A plasma membrane surrounds biological cells and is primarily composed of a bilayer of amphiphilic phospholipids, each of which contains a hydrophilic phosphate head group and hydrophobic fatty acid tails. The membrane selectively regulates which materials enter and exit the cell and the rate of diffusion. Thus, it plays key roles in cell signaling, communication, providing shape via the cytoskeleton, and protecting intracellular species from extracellular ones. In an effort to take advantage of such a system, we are interested in creating model plasma membrane systems with applications where they function in a biomimetic manner, such as chemical sensors.[1] One avenue of gaining control over these systems is through the aqueous overlayer where extracellular species, such as anesthetics, may come in contact with the lipid bilayer. These interactions are of significance because they affect the fluidity of the membrane, which direct the cell's function. Moreover, the findings may provide insight as to how anesthetics work on a molecular level, the mechanisms of which are not well understood.

While general anesthetics have been used for centuries, exactly how they work on the molecular level is somewhat of a mystery. One popular mechanism was proposed by Meyer and Overton in 1901 called the lipid theory.[2-3] They observed a correlation between the potency of general anesthetic agents and the degree to which they are soluble in fats, where potency is "the reciprocal of the concentration causing the loss of the reflex in 50 % of the animals or patients tested." A nearly linear plot results between the potency and oil:gas partition coefficient. Anesthetics can range from having simple molecular structures like those of gases nitrogen, argon, and xenon to the more complex alcohols, alkanes, and amines. Despite the wide variation, it seems that lipid solubility determines their anesthetic effect. Moreover, it is thought that general anesthetics accumulate in the hydrophobic compartments of the central nervous system, namely the plasma membrane of a nerve cell. A change in the membrane bilayer's fluidity and thickness may occur, but an indirect action is more likely. For instance, the lipid bilayer's structure may change in a way that alters how membrane integral proteins function, inducing anesthesia. Although the theory seemed to explain how anesthetics work, exceptions were found and there was accumulating evidence pointing toward general anesthetics interacting with proteins, termed the protein theory, proposed by Franks and Lieb in 1978.[4] In one instance, the firefly luciferase's function was inhibited by the general anesthetic bromoform by binding to a hydrophobic pocket on the enzyme.[5] Additionally, stereoisomers of anesthetic compounds are soluble in lipids to the same extent but have different anesthetic effects. These findings, along with more research, show that lipid solubility is not the sole determinant of anesthetic potency. Nonetheless, there is no widespread consensus as to how they work on the molecular level.

The focus of this work is on the effects of short-chain alcohols on a planar supported lipid bilayer. Ethanol has been used as a general anesthetic[6] and its hydroxyl group may participate in hydrogen bonding interactions with the lipid headgroups in a plasma membrane. Additionally, ethanol's hydrocarbons may interact with the acyl chains of lipids to an extent. Synthetic lipid bilayers are well-controlled, and the results from fluidity experiments aid in performing similar studies with live cell membranes. Previous work involved a planar phosphocholine lipid model bilayer comprised of 1,2-dimyristoyl-*sn*-phosphatidylcholine (DMPC) and a fluorescent probe perylene at 289 K (gel phase) and 303 K (fluid phase) (Figure 3.1).[7] The concentration of ethanol was varied in the system to study the extent to which it affects properties of the bilayer structure, via measuring rotational diffusion dynamics of the chromophore. Fluorescence lifetime and anisotropy decay data were obtained from time-correlated single-photon counting (TCSPC) measurements. It was revealed through data analyses that ethanol, around 0.6 M concentration, affects the organization of the C_{14} phosphocholine bilayer structure below and above the gel-to-fluid transition temperature (289 K and 303 K). The results were consistent with those in the literature on phospholipids undergoing interdigitation phase transitions in the gel phase.[8-14] The work showed the influence of ethanol on membrane fluidity and organization for synthetic phosphocholine bilayers.

In a different study by Setiawan, the effects of ethanol on the structure of planar lipid bilayer structures were studied.[15] However, in an effort to create a model plasma membrane system that could function in a biomimetic manner, a ternary model system was synthesized. It consisted of 1,2-dioleoyl-*sn*-phosphatidylcholine (DOPC), cholesterol, and sphingomyelin formed on mica (Figure 3.1). The rationale for such a composition was, in part, based on the observation of microscale phase segregation of cholesterol and phosphocholine domains, in the presence of sphingomyelin.[16-18] Akin to Pillman's work, the tethered fluorescent probe sulforhodamine-tagged-1,2-dioleoyl-*sn*-phosphatidylethanolamine (SR-DOPE) was used for time-resolved fluorescence measurements. Steady state fluorescence imaging and fluorescence lifetime imaging were performed using the TCSPC system, and fluorescence anisotropy decay imaging (FADI) data were obtained via an inverted confocal scanning microscope. Steady state fluorescence images and the orientational relaxation dynamics of the SR-DOPE chromophore showed that there were structural changes in the lipid bilayer structure in the vicinity of 0.8 M ethanol; its integrity was compromised at 1.5 M ethanol concentration. Similar experiments were performed using *n*-butanol where the model bilayer was disrupted over a greater extent on the scale of micrometers.[19] Noticeable changes in chromophore rotational dynamics occurred around 0.4 M concentration likely due to the more amphipathic character of *n*-butanol.

A common theme that arises from these studies hints toward the broader application in the field of anesthesia since short-chain alcohols may have anesthetic affects. Therefore, in this work, we are interested in measuring perylene diffusion over a range of distances, from sub-micron to sub-millimeter, providing insight into the compositional heterogeneity that characterizes these model bilayer structures. Specifically, Setiawan's model system served as a benchmark, with slight modifications, elucidated in the Experimental section (*vide infra*).[19] For instance, the mica support was rinsed with 60 μL (instead of 3 mL) of Tris® buffer, ethanol, or *n*-butanol to have sufficient fluorescence intensity during measurements.

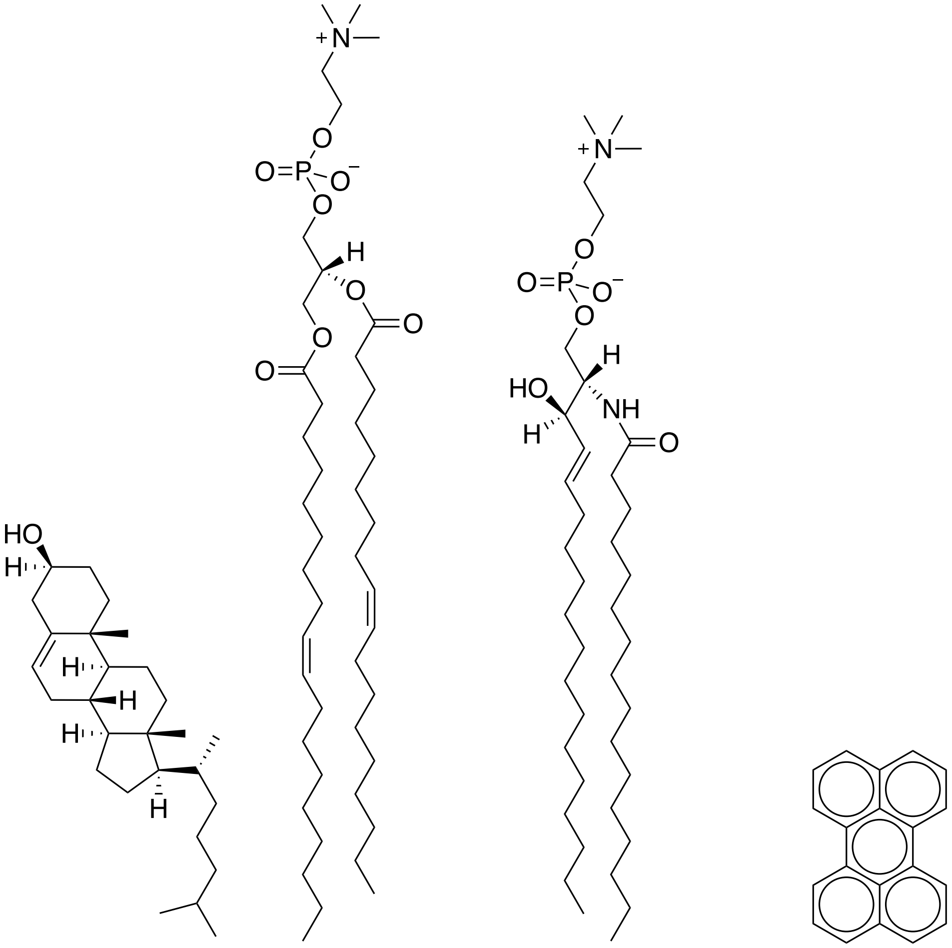

Figure 3.1. Molecular Structures of Model Bilayer Components. From left to right: cholesterol, DOPC, sphingomyelin, and perylene.

Experimental

Chemicals. Cholesterol (ovine wool), 1,2-dioleoyl-*sn*-glycero-3-phosphocholine (DOPC), and sphingomyelin (chicken egg) were purchased from Avanti® Polar Lipids, Inc.; perylene, calcium chloride, Trizma® hydrochloride, Trizma® base, and ethanol (200 proof, ACS grade) from Sigma-Aldrich; and *n*-butanol from Spectrum® Chemical. All compounds were used without further purification. Milli-Q® water (18 MΩ•cm) was used to prepare 10 mM Tris® buffer consisting of Trizma® HCl and Trizma® base (pH ~7.5). High grade mica (Ted Pella, Inc.) was the substrate.

Vesicle Preparation and Formation. The first step involves pipetting desired amounts of lipids and perylene (dissolved in chloroform) in a 20-mL glass vial. The volumes were commensurate with 10 mole % cholesterol, 47-49 mole % DOPC, 40 mole % sphingomyelin, and 1-3 mole % perylene. Thereafter, the mixture was dried under a stream of nitrogen gas for at least 20 minutes and Milli-Q water was added, such that the final lipid concentration was 1 mg/mL. The vial was capped (sealed with Parafilm®) and immersed in a liquid nitrogen bath for 5 minutes, followed by thawing in a 60 °C water bath for 5 minutes, and finally vortexed for 2 minutes; the freeze-thaw-vortex process was performed five times.

Vesicle Extrusion. After the five cycles, 0.5-mL aliquots of the vesicle solution were extruded 11 times with a mini extruder apparatus (Avanti® Polar Lipids, Inc.) at room temperature (Figure 3.2).[20] It consisted of two 1000-µL syringes (Hamilton GASTIGHT® #1001), two filter supports, and a 50-nm pore size polycarbonate membrane disc (Whatman® 19 mm diameter, Nuclepore™ PC hydrophilic track-etched filter).

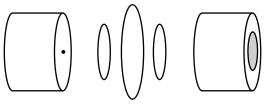

Figure 3.2. Avanti® Mini Extruder Diagram. The assembly parts are shown through which two syringes go, that face each other.[20]

Dynamic Light Scattering. The extruded solution was characterized using the Dynamic Light Scattering (DLS) technique, which gives particle size distributions. DLS measurements were obtained at 25 ºC using a Malvern Zetasizer Nano ZS. The instrument was warmed up for 30 minutes prior to acquiring data. A plastic cuvette (cell # ZEN0112) was used. DOPC was selected as the material and water as the dispersant. An example is shown in Figure 3.3.

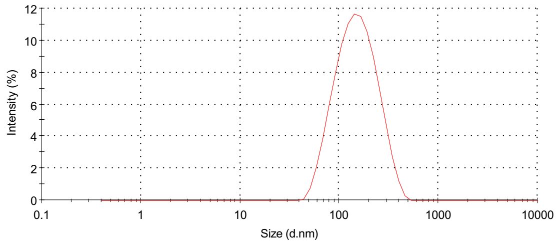

Figure 3.3. Particle Size Distribution of Extruded Solution. The y-axis represents random fluctuations in the intensity of light scattered from the solution, and the average diameter here is 133 nm.

Vesicle Deposition/Fusion to form SLBs. The extruded vesicle solution was at room temperature before deposition. First, a mica sheet was glued on a plastic petri dish containing a hole (for the FRAP instrument lens), then a thin layer of mica was peeled with a razor blade and immediately, 7 µL of 2 mM $CaCl_2$ solution were pipetted onto the surface, followed by 60 µL of the vesicle solution. The solutions stayed on the mica slide for 15 minutes, then depending on the system of interest, 60 µL Tris® buffer, 60 µL ethanol (0.3 - 1.5 M), or 60 µL *n*-butanol (0.1 - 0.6 M) were added. The petri dish assembly was sealed with Parafilm® and left for 1 hour to ensure planar bilayer formation.

Fluorescence Recovery After Photobleaching (FRAP). FRAP is a fluorescence microscopy technique that involves photobleaching a small area of fluorescent molecules, called region of interest (ROI), with a high laser intensity.[21, 22] The fluorescence intensity is then monitored over time, and the rate of recovery gives information on two-dimensional lateral diffusion and molecular movement in the system of interest, namely planar model lipid bilayers. The instrument consists of an inverted microscope and four lasers.

Briefly, the system is equipped with a confocal scanning microscope (Nikon C2+), that provides high resolution, and five objectives of 10X, 20X, 40X, 60X, and 100X, of which the 10X was used. The laser system excites at 405, 488, 561, and 640 nm with the dyes 4′,6-diamidino-2-phenylindole (DAPI), fluorescein isothiocyanate (FITC), sulforhodamine 101 acid chloride (Texas Red), and cyanine 5 (Cy5), respectively. DAPI was used for exciting the perylene fluorophore.

Samples were placed on a motorized stage. The circular ROI had a radius of 10 µm for stimulation and the entire area (including ROI) was selected as a reference. A continuous scanning time measurement was performed to ensure the bilayer was not moving significantly for fluidity measurements, indicated by a fairly constant fluorescent intensity value over time. Raw data were saved as Microsoft Excel spreadsheets, normalized, and fit using MATLAB software (MathWorks).

Results and Discussion

The central point of this work is to understand how anesthetics work on the molecular level by studying the effects of varying concentrations of ethanol and *n*-butanol on the fluidity of a planar lipid bilayer on mica. The results also provide insight to understanding membrane structure and dynamics. We obtain the information from magnitudes and distributions of translational diffusion constants via fluorescence recovery after photobleaching experiments (Figures 3.4, 3.5). Based on the Stokes-Einstein equation, we see how translational diffusion D (in $\mu m^2/s$) is related to viscosity, where η is the viscosity of the medium and r is the radius of the diffusing moiety (assumed to be spherical), namely perylene.[23-25]

$$D = \frac{k_B T}{6\pi\eta r}$$

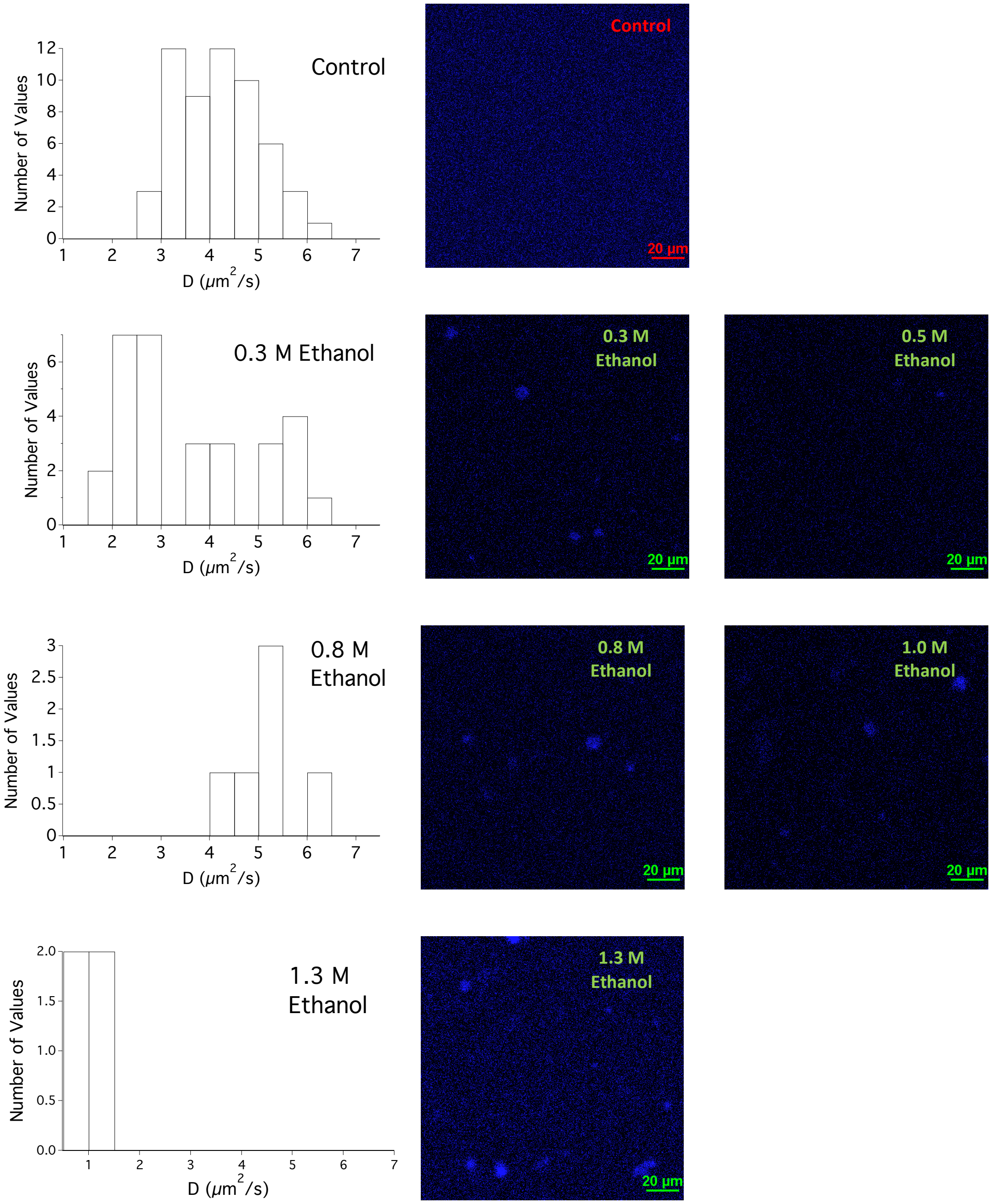

Figure 3.4. Histograms of Translational Diffusion Constants and Fluorescence Images of Control and Ethanol Supported Lipid Bilayers. The excitation wavelength is 405 nm and perylene emits around 480 nm.[7] The control has Tris® buffer in the aqueous overlayer, and ethanol concentrations range from 0.3 - 1.3 M.

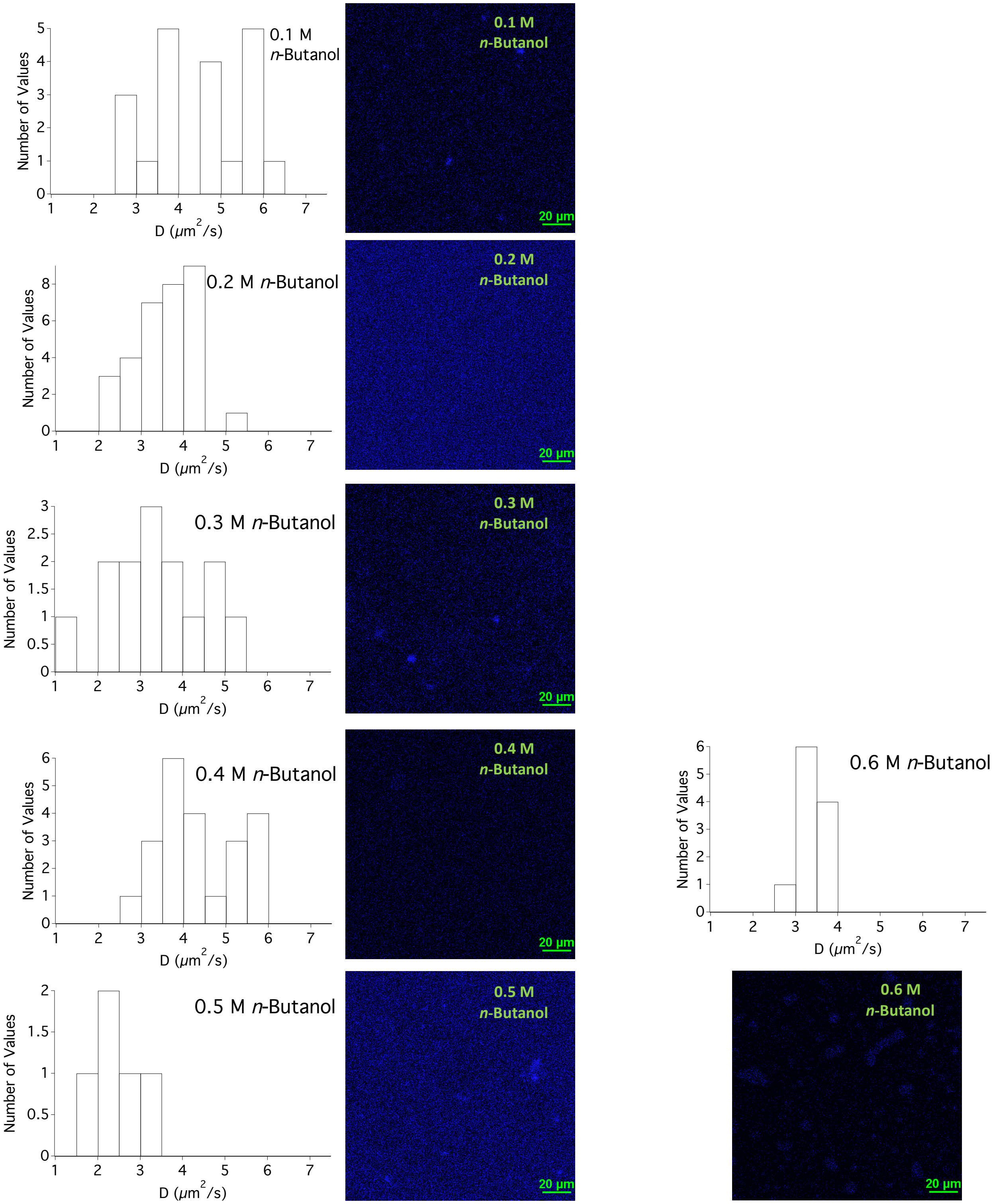

Figure 3.5. Histograms of Translational Diffusion Constants and Fluorescence Images of *n*-Butanol Supported Lipid Bilayers. The excitation wavelength is 405 nm and perylene emits around 480 nm.[7] The concentrations of *n*-butanol in the aqueous overlayer span 0.1 - 0.6 M.

The initial procedure of vesicle deposition to form the planar SLBs involved little to no rinsing of the mica support because the fluorescence intensity would decrease drastically if rinsed. However, there were bright spots around 10 μm in diameter which appeared throughout. Troubleshooting methods involved depositing solutions on mica in different orders, increasing perylene concentration, changing FRAP parameters, extruding via membranes of different pore sizes, filtering aqueous solutions (Milli Q water, Tris® buffer, and $CaCl_2$), sonicating vesicles instead of extruding, and utilizing glass surfaces. Literature searches revealed the presence of circular bright spots in other researchers' SLB systems which were attributed to unfused lipid vesicles.[26-28] Numerous trials later, an effective method was rinsing the aqueous overlayer with 60 μL of desired solution and waiting for an hour before collecting data.

For fluidity measurements of artificial lipid bilayers involving the perylene probe, the pure diffusion model was applied where perylene is thought to reside in the aliphatic chains due to its hydrophobicity.[7, 29] The model assumes free diffusion and relatively non-existent binding of the fluorophore to support:

$$f(t) = e^{-\frac{\tau_D}{2t}}\left[I_o\left(\frac{\tau_D}{2t}\right) + I_1\left(\frac{\tau_D}{2t}\right)\right]$$

$$\tau_D = \frac{\omega^2}{4D}$$

I_o and I_1 are modified Bessel functions, τ is the recovery time constant, ω is the radius of the bleaching spot, and D is the translational diffusion constant, explained by Soumpasis[23] and Baumler.[30]

While the benchmark for this work is Setiawan's ternary model system, the chromophores are different; sulforhodamine-tagged phospholipid (SR-DOPE) measures phospholipid headgroup diffusion, whereas perylene was used in this work, which is not bound and measures tail group mobility. As presumed in that work, the SR-DOPE chromophore was distributed equally between the top and bottom lipid leaflets and an aqueous layer on the mica support, and we too make the same assumption with perylene. Moreover, he utilized the fluorescence anisotropy decay imaging technique to obtain fluorescence images and chromophore rotational diffusion, whereas we used fluorescence recovery after photobleaching to measure chromophore translational diffusion. Translational diffusion is generally better and more useful here because we get information on the μm to mm length scales whereas rotational diffusion measurements provide information on the μm or smaller scales. Nevertheless, while the diffusion constant data are different, there are similarities.

The average translational diffusion value for the control system within one standard deviation is 4.2 ± 0.8 $\mu m^2/s$ (n = 56) and varied from 2.6 - 6.4 $\mu m^2/s$ (Table 3.1). Although the fluorescence image appears to show an even distribution, further analysis from a histogram of the diffusion values revealed a wide distribution, indicative of a heterogeneous nature of the supported lipid bilayer (Figure 3.4), which was also observed by Setiawan.[15] Thereafter, ethanol was applied to the aqueous overlayer at different concentrations, and significant changes were immediately observed.

Table 3.1. Translational Diffusion Constants (D) for the Control Supported Lipid Bilayer System. Samples A-F represent experiments performed on individually cleaved mica slides and n is the number of measurements. Bilayers are composed of 10 mole % cholesterol, 40 mole % sphingomyelin, 47 mole % DOPC and 3 mole % perylene (A-D) or 49 and 1 mole % DOPC and perylene, respectively (E-F). Data are represented as mean ± one standard deviation.

Sample	D ($\mu m^2/s$)	n
A	4.3 ± 1.0	13
B	4.0 ± 0.6	8
C	3.7 ± 0.5	10
D	4.8 ± 0.8	8
E	3.7 ± 0.8	8
F	4.7 ± 0.5	9

From images, circular bright spots were present at every concentration of ethanol tested, potentially characteristic of unfused vesicles and/or perylene aggregates (Figure 3.4).[26-28] They did not interfere with the regions of interest at 0.3 M, making it possible to obtain diffusion constants. The values also have a wide range of 1.6 - 6.2 μm^2/s, with the possibility of areas in the planar bilayer that had both more fluid- or more rigid-like structures. Upon increasing the ethanol concentration to 0.5 M, the bright spots moved too quickly and interfered with data collection leading us to believe the system was more fluid. A reasonable explanation is that the hydroxyl groups of ethanol undergoes hydrogen bonding interactions with those of the lipids, resulting in dilation of the head groups. Surprisingly for 0.8 M ethanol, images showed both slow- and fast-moving spots with diameters of 5-10 μm and some greater than 20 μm giving more insight to the heterogeneous nature of the system. The images also hint that the structure was starting to degrade, which was also noted by Pillman and Setiawan.[7, 15] Nonetheless, it was possible to collect few diffusion values which had a high range of 4.3 - 6.1 μm^2/s, indicative of a more fluid system as predicted. From concentrations of 1.0 M ethanol and above, there was difficulty collecting data, despite many attempts, so the structure seemed to have degraded significantly, consistent with Setiawan's work.[15] Even fewer values were obtained at 1.5 M, but the low values of 0.6 – 1.3 μm^2/s are meaningful, discussed later (*vide infra*). In order to gain more insight into the structural dynamics of the bilayer system, similar experiments were performed using *n*-butanol.

Although the diffusion constants are on a similar order of magnitude, the images give more information. The morphological differences, compared to ethanol application, were strikingly different. This is not surprising as *n*-butanol has two more carbon atoms than ethanol, allowing it to penetrate farther into the acyl chains of the lipids. As a result, more diffusion values were obtained due to the absence of fast-moving spots, only a few appeared at 0.3 M *n*-butanol and patches of bright areas appeared at 0.6 M showing physical disruption of the bilayer, and there are wider distributions of values at lower concentrations than for the system exposed to ethanol (Figure 3.5). The fluorescence image at 0.4 M is drastically different than the rest, and Setiawan had also noticed loss of fluorescence signal here, which he attributed to the bilayer detaching from the mica support.[19] As with the ethanol system, the *n*-butanol analog also exhibits a similar trend of diffusion values increasing with concentration, then decreasing. Both alcohols participate in hydrogen bonding and van der Waals interactions with the lipid headgroup and acyl chains to different extents, respectively. Taken together, it is thought that at high concentrations, dilation of the lipid headgroup occurs and the "gallery" region between phospholipid tails disappear, leading to bilayer interdigitation (Figure 3.6).[7-15, 19, 31-40]

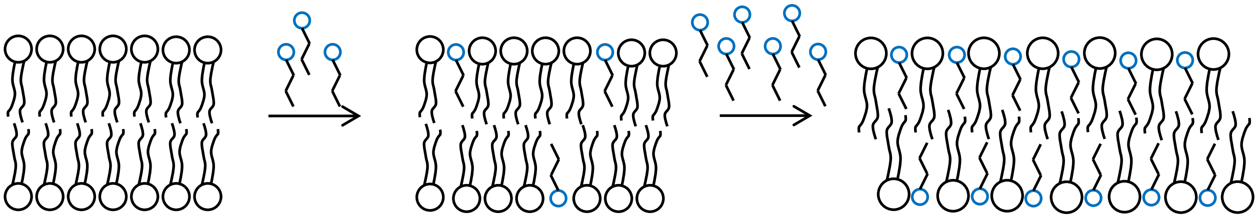

Figure 3.6. Simplified Illustration of Lipid Interdigitation. The molecules on top of arrows represent ethanol or *n*-butanol.

Conclusions

We have performed fluidity measurements, utilizing fluorescence recovery after photobleaching, on planar lipid bilayers on mica with Tris buffer, ethanol, and *n*-butanol as liquid overlayers. The model was composed of cholesterol, DOPC, sphingomyelin, and perylene. The diverse spread of translational diffusion constants showed a heterogeneous distribution of molecules in the membrane. However, there was a trend of increasing fluidity with increasing concentrations of the short-chain alcohols until high concentrations, where fluidity decreased. The results suggest that the leaflets dilate to a point, then interpenetrate which makes the system rigid and can prevent a live cell from functioning properly. Although care was taken to obtain reproducible results, heterogeneity makes it a challenge to discover potential outliers.

It was imperative that variables were kept constant, such as pH, temperature, and type of substrate, but key factors accounting for variations in data could be how mica slides were peeled. Dynamic Light Scattering measurements were performed prior to fluidity measurements to ensure the same particle size distribution (Figure 3.3). However, the contamination profile of lab environments and effects of lipids oxidizing are factors worth investigating. Moreover, other characterization techniques, like transmission electron microscopy would be useful. Moving forward, the effects of variables such as pH and ionic strength of aqueous overlayer solution are worth pursuing. From a macroscopic perspective, how general anesthetics work on the physiological system are known, but there can be side effects such as memory loss, nausea, headache, nerve damage which vary in severity and frequency. Understanding the molecular mechanisms may provide insight to reduce harmful risks and/or synthesis of more effective general anesthetics.

REFERENCES

REFERENCES

1. Siontorou, C. G.; Nikoleli, G.-P.; Nikolelis, D. P.; Karapetis, S. K., Artificial Lipid Membranes: Past, Present, and Future. *Membranes* **2017,** *7*, 38.

2. Antkowiak, B., How do general anaesthetics work? . *Naturwissenschaften* **2001,** *88*, 201-213.

3. Overton, C. E., *Studien Über Die Narkose: Zugleich Ein Beitrag Zur Allgemeinen Pharmakologie*. Jena Fischer: 1901.

4. Franks, N. P.; Lieb, W. R., Where do general anaesthetics act? *Nature* **1978,** *274* (5669), 339-342.

5. Franks, N. P.; Jenkins, A.; Conti, E.; Lieb, W. R.; Brick, P., Structural Basis for the Inhibition of Firefly Luciferase by a General Anesthetic. *Biophysical Journal* **1998,** *75* (5).

6. Wong, S. M. E.; Fong, E.; Tauck, D. L.; Kendig, J. J., Ethanol as a General Anesthetic: Actions in Spinal Cord. *European Journal of Pharmacology* **1997,** *329*, 121-127.

7. Pillman, H. A.; Blanchard, G. J., Effects of Ethanol on the Organization of Phosphocholine Lipid Bilayers. *Journal of Physical Chemistry B* **2010,** *114*, 3840-3846.

8. Vierl, U.; Löbbecke, L.; Nagel, N.; Cevc, G., Solute Effects on the Colloidal and Phase Behavior of Lipid Bilayer Membranes: Ethanol-Dipalmitoylphosphatidylcholine Mixtures. *Biophysical Journal* **1994,** *67* (3), 80572-80577.

9. Rowe, E. S., Lipid Chain Length and Temperature Dependence of Ethanol-Phosphatidylcholine Interactions. *Biochem.* **1983,** *22*, 3299-3305.

10. Bondar, O. P.; Rowe, E. S., Role of Cholesterol in the Modulation of Interdigitation in Phosphatidylethanols. *Biochimica et Biophysica Acta* **1998,** *1370* (2), 207-217.

11. Lobbecke, L.; Cevc, G., Effects of Short-Chain Alcohols on the Phase Behavior and Interdigitation of Phosphatidylcholine Bilayer Membranes. *Biochim. Biophys. Acta* **1995,** *1237*, 59.

12. McIntosh, T. J.; Lin, H.; Li, S.; Huang, C., The Effect of Ethanol on the Phase Transition Temperature and the Phase Structure of Monounsaturated Phosphatidylcholines. *Biochimica et Biophysica Acta* **2001,** *1510* (1-2), 219-230.

13. Bartucci, R.; Páli, T.; Marsh, D., Lipid Chain Motion in an Interdigitated Gel Phase: Conventional and Saturation Transfer ESR of Spin-Labeled Lipids in Dipalmitoylphosphatidylcholine-Glycerol Dispersions. *Biochemistry* **1993,** *32* (1), 274-281.

14. Hata, T.; Matsuki, H.; Kaneshina, S., Effect of local anesthetics on the bilayer membrane of dipalmitoylphosphatidylcholine: interdigitation of lipid bilayer and vesicle-micelle transition. *Biophysical Chemistry* **2000,** *87* (1), 25-36.

15. Setiawan, I.; Blanchard, G. J., Ethanol-Induced Perturbations to Planar Lipid Bilayer Structures. *J. Phys. Chem. B* **2014,** *118*, 537-546.

16. de Almeida, R. F. M.; Fedorov, A.; Prieto, M., Sphingomyelin/ Phosphatidylcholine/ Cholesterol Phase Diagram: Boundaries and Composition of Lipid Rafts. *Biophys. J.* **2003,** *85*, 2406-2416.

17. de Almeida, R. F. M.; Loura, L.; Prieto, M., Membrane Lipid Domains and Rafts: Current Applications of Fluorescence Lifetime Spectroscopy and Imaging. *Chem. Phys. Lipids* **2009,** *157*, 61-77.

18. Marques, J. T.; Viana, A. S.; de Almeida, R. F. M., Effects on Binary and Ternary Supported Lipid Bilayers with Gel/Fluid Domains and Lipid Rafts. *Biochim. Biophys. Acta* **2011,** *1808*, 405-411.

19. Setiawan, I.; Blanchard, G. J., Structural Disruption of Phospholipid Bilayers over a Range of Length Scales by n-Butanol. *J. Phys. Chem. B* **2014,** *118*, 3085-3093.

20. https://avantilipids.com/product/610000 Avanti Polar Lipids.

21. Axelrod, D.; E., K. D.; Schlessinger, J.; Elson, E.; Webb, W. W., Mobility Measurement by Analysis of Fluorescence Photobleaching Recovery Kinetics. *Biophys. J.* **1976,** *16*, 1055-1069.

22. Ishikawa-Ankerhold, H.; Ankerhold, R.; Drummen, G., *Encyclopedia of Life Sciences*. John Wiley & Sons, Ltd.: Chichester, 2014.

23. Soumpasis, D. M., Theoretical analysis of fluorescence photobleaching recovery experiments. *Biophys. J.* **1983,** *41*, 95-97.

24. Kijewska, K.; Blanchard, G. J., Using Diffusion To Characterize Interfacial Heterogeneity. *Langmuir* **2017,** *33* (5), 1155-1161.

25. Brilliantov, N. V.; Denisov, V. P.; Krapivsky, P. L., Generalized Stokes-Einstein-Debye relation for charged Brownian particles in solution. *Physica a-Statistical Mechanics and Its Applications* **1991,** *175* (2), 293-304.

26. Keller, C. A.; Kasemo, B., Surface specific kinetics of lipid vesicle adsorption meadured with a quartz crystal microbalance. *Biophys. J.* **1998,** *75*, 1397-1402.

27. Keller, C. A.; Glasmastar, K.; Zhdanov, V. P.; Kasemo, B., Formation of supported membranes from vesicles. *Phys. Rev. Lett.* **2000,** *84*, 5443-5446.

28. Smith, E. A.; Coym, J. W.; Cowell, S. M.; Tokimoto, T.; Hruby, V. J.; Yamamura, H. I.; Wirth, M. J., Lipid bilayers on polyacrylamide brushes for inclusion of membrane proteins. *Langmuir* **2005,** *21*, 9644-9650.

29. Lapinski, M. M.; Blanchard, G. J., Interrogating the role of liposome size in mediating the dynamics of a chromophore in the acyl chain region of a phospholipid bilayer. *Chem. Phys. Lipids* **2008,** *153*, 130-137.

30. Baumler, S. M. Diffusional motion as a gauge of interfacial fluidity and adhesion of supported model membrane films. Michigan State University, 2017.

31. Hutterer, R.; Hof, M., Probing Ethanol-Induced Phospholipid Phase Transitions by the Polarity Sensitive Fluorescence Probes Prodan and Patman. *Z. Phys. Chem.* **2002,** *216*, 333-346.

32. Komatsu, H.; Rowe, E. S., Effect of Cholesterol on the Ethanol-Induced Interdigitated Gel Phase in Phosphatidylcholine: Use of Fluorophore Pyrene-Labeled Phosphatidylcholine. *Biochem* **1991,** *30*, 2463-2470.

33. Nambi, P.; Rowe, E. S.; McIntosh, T. J., Studies of the Ethanol-Induced Interdigitated Gel Phase in Phosphatidylcholines Using the Fluorophore 1,6-Diphenyl-1,3,5-hexatriene. *Biochem* **1988,** *27*, 9175-9182.

34. Roth, L. G.; Chen, C., Thermodynamic Elucidation of Ethanol-Induced Interdigitation of Hydrocarbon Chains in Phosphatidylcholine Bilayer Vesicles. *J. Phys. Chem.* **1991,** *95*, 7955-7959.

35. Rowe, E. S.; Cutrera, T. A., Differential Scanning Calorimetric Studies of Ethanol Interactions with Distearoylphosphatidylcholine: Transition to the Interdigitated Phase. *Biochem.* **1990,** *29*, 10398-10404.

36. Zeng, J.; Chong, P. L., Interactions between Pressure and Ethanol on the Formation of Interdigitated DPPC Liposomes: A Study with Prodan Fluorescence. *Biochem.* **1991,** *30*, 9485-9491.

37. Jianxun, M.; Jie, Y.; Huang, C.; Zhifeng, S., Alcohol Induces Interdigitated Domains in Unilamellar Phosphatidylcholine Bilayers. **1994,** *33*, 9981–9985.

38. Patra, M.; Salonen, E.; Terama, E.; Vattulainen, I.; Faller, R.; Lee, B. W.; Holopainen, J.; Karttunen, M., Under the Influence of Alcohol: The Effect of Ethanol and Methanol on Lipid Bilayers. *Biophysical Journal* **2006,** *90* (4), 1121-1135.

39. Reeves, M. D.; Schawel, A. K.; Wang, W.; Dea, P., Effects of Butanol Isomers on Dipalmitoylphosphatidylcholine Bilayer Membranes. *Biophysical Chemistry* **2007,** *128* (1), 13-18.

40. Kranenburg, M.; Vlaar, M.; Smit, B., Simulating Induced Interdigitation in Membranes. *Biophysical Journal* **2004,** *87* (3), 1596-1605.

CHAPTER 4: INVESTIGATING ANOMALOUS DIFFUSION IN HETEROGENOUS SUPPORTED LIPID BILAYERS VIA TRANSLATIONAL DIFFUSION

Abstract

Utilizing fluorescence recovery after photobleaching (FRAP), insight was obtained about translational diffusion constants on the micrometer scale of mica supported lipid bilayers composed of cholesterol, 1,2-dioleoyl-*sn*-phosphatidylcholine (DOPC), sphingomyelin, and ceramide, with perylene or 1,2-dioleoyl-*sn*-glycero-3-phosphoethanolamine-N-(lissamine rhodamine B sulfonyl) as the fluorescent probe. Lipid vesicles were formed and extruded via 50, 100, 200, and 400-nm polycarbonate membrane discs. Ceramide-based systems offered resistance during extrusion, and though they have lower diffusion constants than the control, the distribution of values is indicative of a heterogeneous system. Furthermore, a rhodamine-based system and size-dependence study show anomalous diffusion behavior which represents the complexity of mammalian plasma membranes. In the rhodamine batch, dark spots are cholesterol domains and bright ones are likely phospholipids. It is possible different domains, such as liquid-ordered (L_o) and liquid-disordered (L_d), exist in the systems that are rich in cholesterol and sphingomyelin.

Introduction

A biological cell is the smallest fundamental unit of life and the selectively permeable plasma membrane surrounding it protects the cell the from extracellular species, aids in cell signaling, and mediates cellular processes. It is primarily composed of phospholipids with other molecules interspersed throughout, such as cholesterol, proteins, and carbohydrates. The fluidity of the membrane plays a key role for enzymes and transport molecules to function properly, and its function may be studied by performing experiments on simplified model lipid bilayers, the parameters of which are well-controlled. There are various kinds of artificial membranes[1, 2], such as black lipid membranes (BLM)[3-7], polymer-cushioned lipid bilayers[8-14], hybrid bilayers[15-21], tethered lipid bilayers[22-29], suspended lipid bilayers[30, 31], supported vesicular layers[32, 33], supported lipid bilayer patches[34], and supported lipid bilayers (SLB)[35-41]. All have advantages and disadvantages; for example, while BLMs are well suited for electrical characterization, they generally have poor lifetimes of less than an hour[42]. We choose SLBs for our experiments (*vide infra*) because they are stable for long-term experiments, amenable to multiple physical characterization techniques, and there is ample groundwork in the Blanchard research laboratories, for novel experiments, with components relevant to this work shown in Figure 4.1.[35-41] We received the inspiration for including ceramide in SLBs from the work of Chakravarthy *et al.* who focused on mitigating ceramide levels in synthetic and mice circulating angiogenic cell membranes.[43] Their work is ultimately geared toward increasing the armamentarium of the effective treatment options for people afflicted with diabetic retinopathy (DR). This complication of diabetes affects 5.3 million adults in the U.S. and 24,000 of them go blind each year; 60 percent are affected after within 10 years of their diabetic diagnosis and 80 percent within 15 years of their diagnosis.[44-46] A circulating angiogenic cell (CACs) is a bone marrow-derived reparative cell that promotes angiogenesis (development of new blood vessels) but whose membrane fluidity is compromised in dyslipidemia which patients with DR may be inflicted with.[47] Acid sphingomyelinase (ASM) is an enzyme that catalyzes the hydrolysis of sphingomyelin to ceramide, and the latter may intercalate into the plasma membrane, making it more rigid (Figure 4.2).[43, 48] Therefore, inhibiting ASM in diabetic CACs was shown to improve membrane fluidity, and the cells egressed from the bone marrow toward damaged retinal vessels.[43]

We, therefore, synthesized supported lipid bilayers and varied the lipid composition to study the effects of ceramide on the fluidity of the planar membrane and aimed to control the system, with the hopes of correlating the results to live cell membranes. The fluidity was measured using the fluorescence recovery after photobleaching technique, described herein.

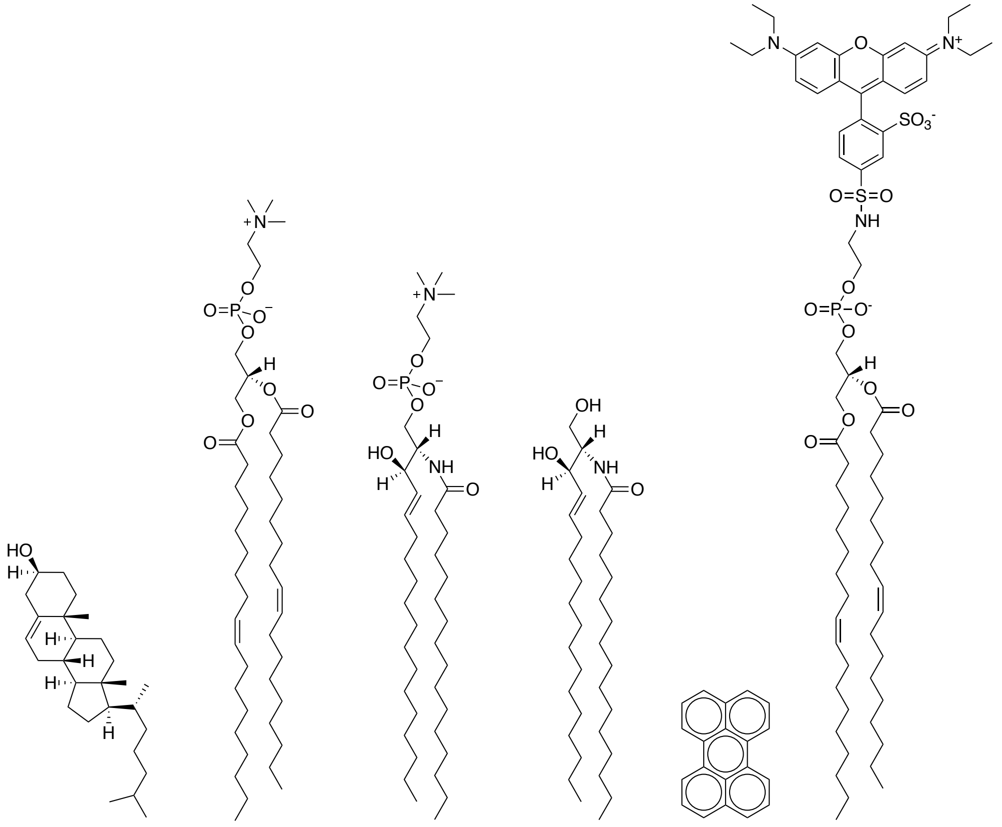

Figure 4.1. Molecular Structures of Lipids and Fluorescent Probes. From left to right: cholesterol, 1,2-dioleoyl-*sn*-phosphatidylcholine (DOPC), sphingomyelin, ceramide, perylene, and 1,2-dioleoyl-*sn*-glycero-3-phosphoethanolamine-N-(lissamine rhodamine B sulfonyl).

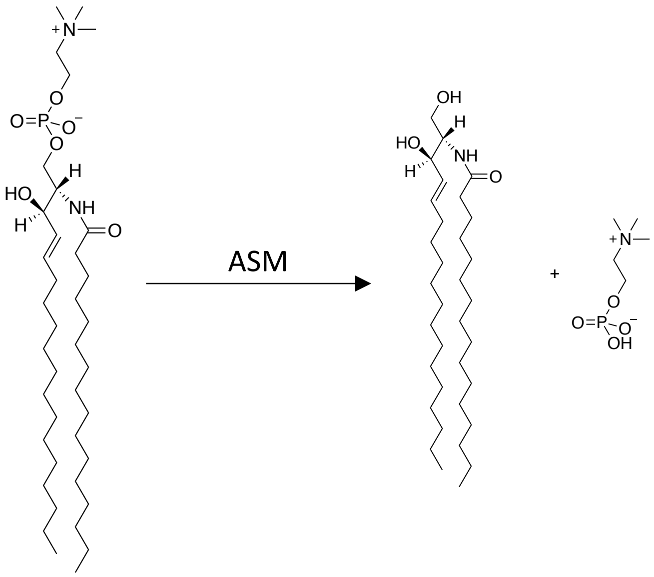

Figure 4.2. Reaction of Sphingomyelin to Ceramide and Phosphorylcholine. The enzyme acid sphingomyelinase (ASM) catalyzes the breakdown via hydrolysis.

Experimental

Materials. Lipids and rhodamine-tethered probe were purchased from Avanti® Polar Lipids and used without further purification. Perylene, calcium chloride, Trizma® hydrochloride, and Trizma® base were purchased from Sigma-Aldrich. A 10 mM Tris® buffer (Trizma® HCl and Trizma® base, pH ~7.5) was prepared with Milli-Q® water (18 MΩ•cm). The solid substrate was high grade mica (Ted Pella, Inc.).

Vesicle Formation and Extrusion. The control system (Batch 1) consisted of 10 mol % cholesterol (ovine wool), 40 mol % sphingomyelin (chicken egg), 47-49 mol % DOPC, and 1-3 mol % perylene. The ceramide system (Batch 2) consisted of 10 mol % cholesterol, 20 mol % sphingomyelin, 20 mol % ceramide, 47 mol % DOPC, and 3 mol % perylene. The rhodamine-based system (Batch 3) consisted of 10 mol % cholesterol (ovine wool), 40 mol % sphingomyelin (chicken egg), 49 mol % DOPC, and 1 mol % 1,2-dioleoyl-*sn*-glycero-3-phosphoethanolamine-

N-(lissamine rhodamine B sulfonyl). Appropriate amounts of constituents, present in chloroform, were dried under $N_{2\,(g)}$ and Tris® buffer was added to result in 1 mg/mL lipid concentration. The mixture underwent five freeze-thaw-vortex cycles of 5, 5, and 2 minutes, respectively; liquid nitrogen was used for freezing and a 60 °C water bath for heating.[39, 40, 43, 49] The vesicle solution of the control was extruded 11 times through a 50-nm polycarbonate membrane disc, ceramide system through a 400-nm filter followed by 200-nm, and rhodamine system through a 100 nm filter. The particle size distribution was characterized by Dynamic Light Scattering measurements, which showed average diameters of the control, ceramide, and rhodamine-based solutions of 133, 145, and 131 nm, respectively.

Planar Bilayer Formation via Vesicle Deposition/Fusion. A hole on a plastic petri dish was cut and a mica slide was glued to the dish for support. Thereafter, a mica sheet was meticulously peeled, followed by addition of 7 μL of $CaCl_2$ and 60 μL of extruded vesicle solution, which sit for 15 minutes before adding 60 μL of Tris® buffer. The dish assembly was covered tightly with Parafilm® and one hour elapsed before performing fluorescence recovery after photobleaching measurements. For Batch 3, the surface was rinsed with a few milliliters of Tris® buffer after the one-hour period.

Translational Diffusion Measurements. The fluorescence recovery after photobleaching microscopy technique was utilized to measure the mobility of the fluorescent probe perylene. The fluorescing molecules in a region of interest (ROI) on a plasma membrane are irreversibly photobleached with high laser intensity (405 nm herein).[50-52] Thereafter, some surrounding fluorophores may diffuse translationally into the ROI, while bleached ones exit. The fluorescence recovery is monitored over time and the resulting curve can be fit to appropriate models for recovery a time constant (τ), which may be converted to translational diffusion constants (D). The instrumental setup was described elsewhere.[53] Briefly, the system consists of an inverted confocal microscope (Nikon C2+), moveable stage, laser systems (405, 488, 561, and 640 nm), an LED illuminator, and standard objectives (Nikon). Data were analyzed with a pure diffusion model (discussed below) using MATLAB software (MathWorks).

Results and Discussion

The goal of this work was to synthesize model lipid bilayers that could mimic a cell membrane and to perform fluidity measurements of those systems. On the macroscopic level, there was incredible resistance during extrusion of ceramide-containing vesicles through membranes with pore diameters of 50 and 100 nm. The amino and hydroxyl groups on ceramide participate in hydrogen bonding interactions with those of the lipids, rigidifying the system (Figure 4.1). Further proof was obtained from fluorescence recovery after photobleaching (FRAP) experiments. Fluorescence recovery curves were fit to a pure diffusion (of perylene) model described by Soumpasis and Baumler, from which fluorescence recovery time constants, τ, were obtained[54, 55]

$$frap(t) = e^{-\frac{\tau_D}{2t}}\left[I_o\left(\frac{\tau_D}{2t}\right) + I_1\left(\frac{\tau_D}{2t}\right)\right]$$

$$\tau_D = \frac{\omega^2}{4D}$$

where I_o and I_1 are modified Bessel functions of the first kind and ω is the ROI radius. The τ value was converted to the translational diffusion constant, D, of perylene. D, in turn, is related directly to the fluidity of the synthetic bilayer and is inversely related to the viscosity, η, of the medium - seen from the Stokes-Einstein equation below

$$D = \frac{k_B T}{6\pi\eta r}$$

where r is the radius of the diffusing molecule.[53, 54, 56]

Mammalian plasma membranes consist of several hundred distinct lipids and proteins, along with carbohydrates.[57] Recent advancements in powerful characterization techniques, such as mass spectrometry, enables the elucidation of some of the complexity.[58-62] We synthesized a simplified model composed of DOPC, sphingomyelin (SM), ceramide (cer), cholesterol (chol), and one-three mole percent of perylene as a fluorescent tag. This control system was presented in our previous work[63], and fluorescence images appear identical (Figure 4.3). However, the control has an average value within one standard deviation of 4.2 ± 0.8 $\mu m^2/s$ (n = 56) while the ceramide system's is 2.8 ± 0.8 $\mu m^2/s$ (n = 113), which was evidence for ceramide's effect of making the membrane stiffer. Although the average values are different, we noticed great variations and gained more insight from plotting diffusion values as a histogram, which shows that the system is heterogeneous (Figure 4.3).

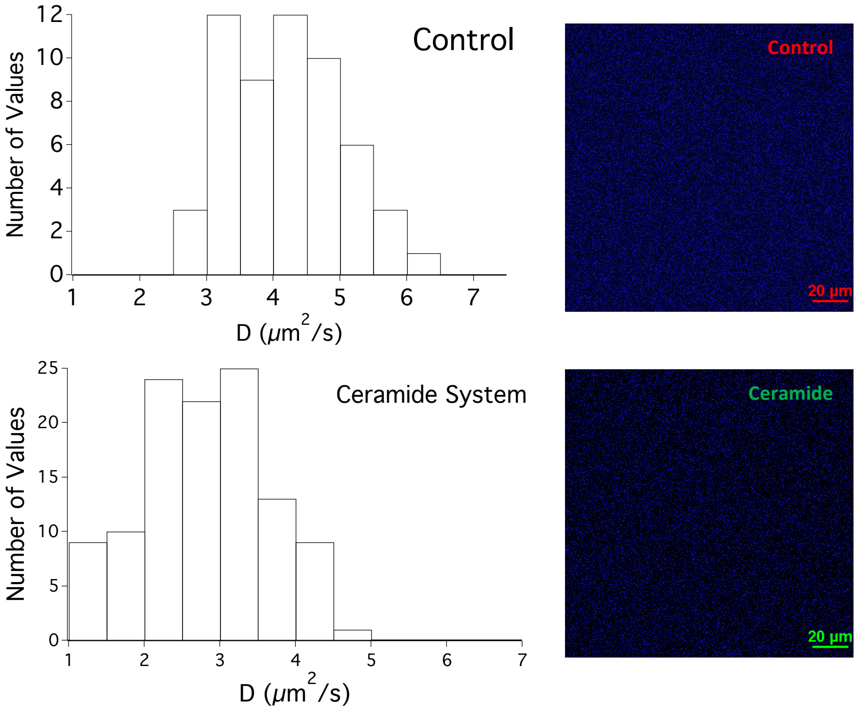

Figure 4.3. Histograms of Translational Diffusion Constants along with Fluorescence Images of Supported Lipid Bilayers. Top: control system representing 56 measurements; bottom: ceramide-based system with 113 measurements. The histogram and image of the control was also presented in our previous unpublished work.[63] The perylene dye was excited at 405 nm, which emits around 480 nm.[64]

Heterogeneity has been observed even in single-component lipid bilayers by Nojimata and Iwata who utilized picosecond time-resolved fluorescence spectroscopy to study rotational dynamics of *trans*-stilbene in their models.[65] Specifically, our ternary control (DOPC, SM, Chol) and Batch 2 (DOPC, SM, Chol, cer) models both exhibited heterogeneity, also observed in similar systems by González-Ramírez who varied the mole percentages of N-palmitoyl derivatives of SM, cer, chol, and dipalmitoylphosphatidylcholine.[66] Moreover, in artificial biomembranes rich in chol and SM, it was shown that liquid-ordered (L_o) and liquid-disordered (L_d) domains exist and freely floating lipid rafts may be present in L_o states.[67-70] While the domains have certainly been observed, the elusive nature of the postulated rafts as well as their nanoscopic dimensions[71-73] make it difficult to detect by the FRAP technique, namely due to its insufficient spatial resolution and ensemble measuring nature.[50, 74, 75] In an effort to probe head group mobility, the perylene probe in Batch 1 (control) was replaced by one mole percent of a sulforhodamine tagged lipid, 1,2-dioleoyl-*sn*-glycero-3-phosphoethanolamine-N-(lissamine rhodamine B sulfonyl) (18:1 Liss Rhod PE) (Figure 4.4).

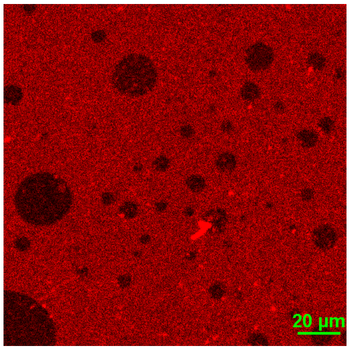

Figure 4.4. Fluorescence Image of Supported Lipid Bilayer containing Rhodamine-PE Fluorophore. The dark spots are cholesterol domains and bright ones are mostly phospholipids. The rhodamine molecule was excited at 561 nm, which emits around 630 nm.[39]

Fluorescence images were similar to Setiawan's, where the dark spots are indicative of cholesterol and bright ones surrounding them are representative of the rhodamine-PE probe with DOPC (Figure 4.4).[39] Unfortunately, it was challenging to measure the fluidity with consistency because the dark regions of varying dimensions (potentially due to lipid aggregates) moved constantly and interfered with ROIs, often precluding data collection. Nonetheless, the varying diameters and distributions of spots in the fluorescence images give some insight of the heterogeneity. Furthermore, we sought to understand the heterogeneous nature of these synthetic bilayers by conducting size-dependence measurements on Batch 2 (ceramide-based model).

The translational diffusion constants as a function of spot size we obtained exhibited a deviation from Fickian, or normal, diffusion (Figure 4.5). According to normal diffusion, the diffusion coefficient should be constant regardless of spot size. However, the trend we see is indicative of anomalous diffusion behavior which was also observed by Kijewska on monolayer systems.[53] For a two-dimensional system where particles exhibit Brownian motion, Gaussian diffusion may be modeled by the Einstein equation[76],

$$\langle r^2 \rangle = 4Dt$$

where $\langle r^2 \rangle$ represents the mean square displacement, D is the translation diffusion coefficient, and t is time. On the other hand, anomalous non-Gaussian diffusion may be represented by the modified equation,

$$\langle r^2 \rangle = 4Dt^{\alpha}$$

in which the case $\alpha < 1$, known as anomalous subdiffusion, has been observed and simulated in plasma membranes and in supported lipid bilayer systems.[76-81] Ratto and Longo had noticed via Monte Carlo simulations of lipid bilayers that diffusion is normal, given a long period of time, but anomalous at short times.[76] While proteins and diverse obstructions can cause anomalous diffusion[82], the phenomenon was observed in our simplified ceramide SLB. Other contributing factors could be the existence of different lipid phases (gel or liquid-like) and phase segregations.

A potential way of characterizing heterogeneity could be placing bounds, such as length scales of diffusion and size distribution of scattering, in models. Information on the boundaries may be gathered from atomic force microscopy studies.

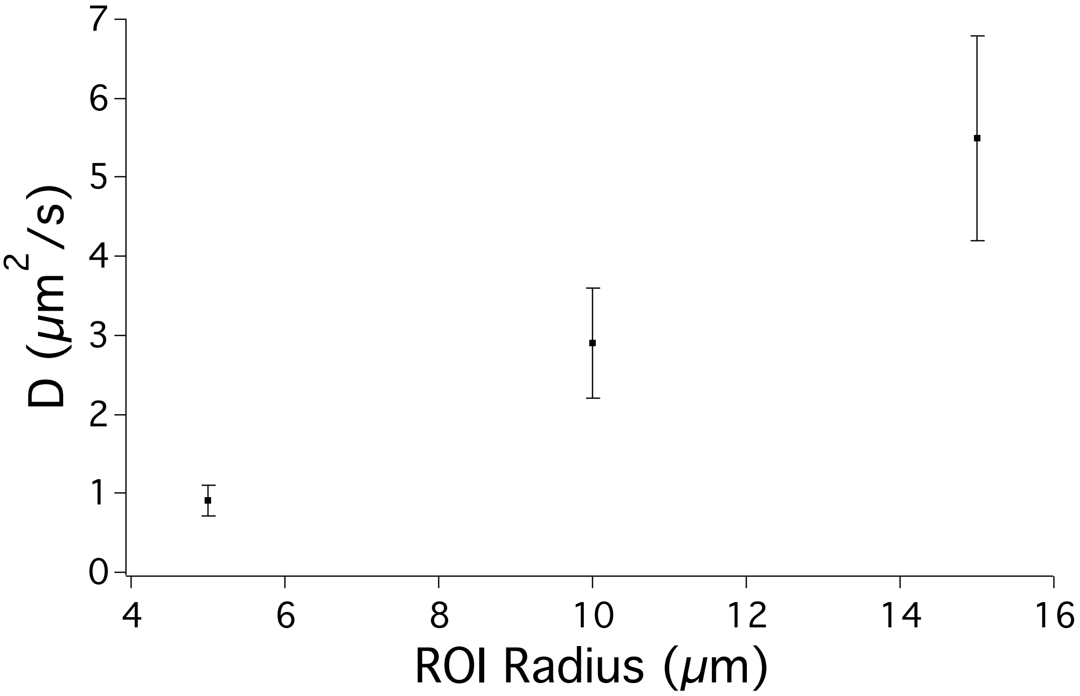

Figure 4.5. Plot of Diffusion Constant for Ceramide-Based Supported Lipid Bilayer as a function of Region of Interest (ROI) Radius. Diffusion coefficients increase as bleaching spot size is increased, implying anomalous diffusion behavior. The number of diffusion measurements are 7, 34, and 12 for radii of 5, 10, and 15 μm, respectively.

Conclusions

Three different lipid bilayer systems supported on mica were studied. Batch 1 (control system) consisted of cholesterol, sphingomyelin, DOPC, and perylene and a histogram of the translational diffusion values, obtained from FRAP experiments, was indicative of a heterogeneous distribution. Batch 2 was similar to the control but also included ceramide, which drastically rigidified the vesicle solution, noticed from resistance in extrusion. Additionally, the histogram of diffusion constants was skewed toward lower values, which is sensible since ceramide may intercalate into the bilayer. The third batch was similar to the control but perylene was replaced with a rhodamine-tethered lipid probe and exhibited dark spots of cholesterol and bright spots of mainly phosphocholines. Thereafter, we probed Batch 2 further by changing the spot size and noticed that the diffusion constant increased with spot radius, indicative of anomalous diffusion.

Even by simplifying our model of the plasma membrane by excluding proteins, complexities are present in lipid bilayers due to possible lipid and dye aggregates, phase segregation, and/or lipid rafts; it is important to understand how those variables are involved in giving the membrane its heterogeneous nature.

The bright spots in the rhodamine system were unexplored in our work but increased in size upon increasing laser intensity irradiation by Setiawan and Blanchard (private communication). It is possible that the system was being heated, then annealing occurred, resulting in microcrystalline lipid domains. It would be worthwhile to investigate this concept further with controlled experiments.

When preparing the supported lipid bilayers, the method of vesicle and bilayer preparation can impact results significantly. Scientists have been working on advancing this area with unique and novel techniques, such the bicelle and solvent-assisted lipid bilayer (SALB) methods.[83, 84] Moving forward, it would be useful to alter lipid profiles and concentrations. For instance, cholesterol is known to regulate membrane fluidity over a range of low and high temperatures by preventing phospholipids from clustering and by decreasing fluidity, respectively. The effects of other variables such as pH, temperature, and ionic strength may be studied as well.

REFERENCES

REFERENCES

1. Castellana, E. T.; Cremer, P. S., Solid supported lipid bilayers: From biophysical studies to sensor design. *Surface Science Reports* **2006,** *61* (10), 429-444.

2. Richter, R. P.; Bérat, R.; Brisson, A. R., Formation of Solid-Supported Lipid Bilayers: An Integrated View. *Langmuir* **2006,** *22* (8), 3497–3505.

3. Mueller, P.; Rudin, D. O.; Tien, H. T.; Wescott, W. C., Reconstitution of Cell Membrane Structure in vitro and its Transformation into an Excitable System. *Nature* **1962,** *194* (4832), 979-980.

4. Mueller, P.; Rudin, D. O.; Tien, H. T.; Wescott, W. C., Methods for the Formation of Single Bimolecular Lipid Membranes in Aqueous Solution. *J. Phys. Chem.* **1963,** *67* (2), 534-535.

5. Tien, H. T.; Ottova-Leitmannova, A., *Membrane Biophysics: As Viewed from Experimental Bilayer Lipid Membranes*. 1st ed.; Elsevier Science: Amsterdam, 2000; Vol. 5.

6. Tien, H. T.; Carbone, S.; Dawidowicz, E. A., Formation of “Black” Lipid Membranes by Oxidation Products of Cholesterol. *Nature* **1966,** *212* (5063), 718-719.

7. Beerlink, A.; Mell, M.; Tolkiehn, M.; Salditt, T., Hard x-ray phase contrast imaging of black lipid membranes. *Appl. Phys. Lett.* **2009,** *95* (203703), 0-3.

8. Sackmann, E., Supported Membranes: Scientific and Practical Applications. *Science* **1996,** *271* (5245), 43-48.

9. Zhang, L.; Longo, M. L.; Stroeve, P., Mobile Phospholipid Bilayers Supported on a Polyion/Alkylthiol Layer Pair. *Langmuir* **2000,** *16* (11), 5093–5099.

10. Shen, W. W.; Boxer, S. G.; Knoll, W.; Frank, C. W., Polymer-Supported Lipid Bilayers on Benzophenone-Modified Substrates. *Biomacromolecules* **2000,** *2* (1), 70–79.

11. Elender, G.; Kühner, M.; Sackmann, E., Functionalisation of Si/SiO2 and Glass Surfaces With Ultrathin Dextran Films and Deposition of Lipid Bilayers. *Biosens Bioelectron* **1996,** *11* (6-7), 565-577.

12. Baumgart, T.; Offenhäusser, A., Polysaccharide-Supported Planar Bilayer Lipid Model Membranes. *Langmuir* **2002,** *19* (5), 1730-1737.

13. Tanaka, M.; Sackmann, E., Polymer-supported membranes as models of the cell surface. *Nature* **2005,** *437* (7059), 656-663.

14. Wong, J. Y.; Park, C. K.; Seitz, M.; Israelachvili, J., Polymer-cushioned bilayers. II. An investigation of interaction forces and fusion using the surface forces apparatus. *Biophys J* **1999,** *77* (3), 1458-68.

15. Plant, A. L.; Brigham-Burke, M.; Petrella, E. C.; O'Shannessy, D. J., Phospholipid/alkanethiol bilayers for cell-surface receptor studies by surface plasmon resonance. *Analytical Biochemistry* **1995,** *226* (2), 342-348.

16. Plant, A. L., Self-assembled phospholipid/alkanethiol biomimetic bilayers on gold. *Langmuir* **1993,** *9* (11), 2764-2767.

17. Plant, A. L., Supported Hybrid Bilayer Membranes as Rugged Cell Membrane Mimics. *Langmuir* **1999,** *15* (15), 5128-5135.

18. Rao, N. M.; Plant, A. L.; Silin, V.; Wight, S.; Hui, S. W., Characterization of biomimetic surfaces formed from cell membranes. *Biophys J* **1997,** *73* (6), 3066-77.

19. Rao, C.; Tutumluer, E.; Kim, I. T., Quantification of Coarse Aggregate Angularity Based on Image Analysis. *Transportation Research Record* **2002,** *02* (3124), 117-124.

20. Hubbard, J. B.; Silin, V.; Plant, A. L., Self Assembly Driven by Hydrophobic Interactions at Alkanethiol Monolayers: Mechanisms of Formation of Hybrid Bilayer Membranes. *Biophysical Chemistry* **1998,** *75* (3), 163-176.

21. Kastl, K.; Ross, M.; Gerke, V.; Steinem, C., Kinetics and Thermodynamics of Annexin A1 Binding to Solid-Supported Membranes: A QCM Study. *Biochemistry* **2002,** *41* (31), 10087–10094.

22. Cornell, B. A.; Braach-Maksvytis, V. L. B.; King, L. G.; Osman, P. D. J.; Raguse, B.; Wieczorek, L.; Pace, R. J., A biosensor that uses ion-channel switches. *Nature* **1997,** *387* (6633), 580-583.

23. Cornell, B. A.; Krishna, G.; Osman, P. D.; Pace, R. D.; Wieczorek, L., Tethered-bilayer lipid membranes as a support for membrane-active peptides. *Biochem Soc Trans* **2001,** *29* (4), 613–617.

24. Beyer, D.; Elender, G.; Knoll, W.; Kiihner, M.; Maus, S.; Ringsdorf, H.; Sackmann, E., Influence of Anchor Lipids on the Homogeneity and Mobility of Lipid Bilayers on Thin Polymer Films. *Angewandte Chemie International Edition* **1996,** *35* (15), 1682-1685.

25. Hausch, M.; Zentel, R.; Knoll, W., Synthesis and characterization of hydrophilic lipopolymers for the support of lipid bilayers. *Macromolecular Chemistry and Physics* **1999,** *200* (1), 174-179.

26. Naumann, C.; Prucker, O.; Lehmann, T.; Rühe, J.; Knoll, W.; Frank, C. W., The Polymer-Supported Phospholipid Bilayer: Tethering as a New Approach to Substrate-Membrane Stabilization. *Biomacromolecules* **2002,** *3* (1), 27-35.

27. Naumann, R.; Schmidt, E. K.; Jonczyk, A.; Fendler, K.; Kadenbach, B.; Liebermann, T.; Offenhäusser, A.; Knoll, W., The peptide-tethered lipid membrane as a biomimetic system to incorporate cytochrome c oxidase in a functionally active form. *Biosensors and Bioelectronics* **1999,** *14* (7), 651-662.

28. Seitz, M.; Ter-Ovanesyan, E.; Hausch, M.; Park, C. K.; Zasadzinski, J. A.; Zentel, R.; Israelachvili, J. N., Formation of Tethered Supported Bilayers by Vesicle Fusion onto Lipopolymer Monolayers Promoted by Osmotic Stress. *Langmuir* **2000,** *16* (14), 6067-6070.

29. Seitz, M.; Wong, J. Y.; Park, C. K.; Alcantar, N. A.; Israelachvili, J. N., Formation of tethered supported bilayers via membrane-inserting reactive lipids. *Thin Solid Films* **1998,** *327–329*, 767–771.

30. Römer, W.; Lam, Y. H.; Fischer, D.; Watts, A.; Fischer, W. B.; Göring, P.; Wehrspohn, R. B.; Gösele, U.; Steinem, C., Channel Activity of a Viral Transmembrane Peptide in Micro-BLMs: Vpu1-32 from HIV-1. *J. Am. Chem. Soc.* **2004,** *126* (49), 16267–16274.

31. Römer, W.; Steinem, C., Impedance Analysis and Single-Channel Recordings on Nano-Black Lipid Membranes Based on Porous Alumina. *Biophys J* **2004,** *86* (2), 955-965.

32. Svedhem, S.; Pfeiffer, I.; Larsson, C.; Wingren, C.; Borrebaeck, C.; Höök, F., Patterns of DNA-labeled and scFv-antibody-carrying Lipid Vesicles Directed by Material-Specific Immobilization of DNA and Supported Lipid Bilayer Formation on an Au/SiO2 Template. *Chembiochem* **2003,** *4* (4), 339-343.

33. Yoshina-Ishii, C.; Boxer, S. G., Arrays of Mobile Tethered Vesicles on Supported Lipid Bilayers. *Journal of the American Chemical Society* **2003,** *125* (13), 3696-3697.

34. Miller, E.; Stubbington, L.; Dinet, C.; Staykova, M., Biophysical insights from supported lipid patches. *Advances in Biomembranes and Lipid Self-Assembly* **2019,** *29*, 23-48.

35. Oberts, B. P.; Blanchard, G. J., Formation of Air-Stable Supported Lipid Monolayers and Bilayers. *Langmuir* **2009,** *25* (5), 2962-2970.

36. Domińska, M.; Krysiński, P.; Blanchard, G. J., Interrogating Interfacial Organization in Planar Bilayer Structures. *Langmuir* **2008,** *24* (16), 8785–8793.

37. Dominska, M.; Mazur, M.; Greenough, K. P.; Koan, M. M.; Krysiński, P. G.; Blanchard, G. J., Probing Organization and Communication at Layered Interfaces. *Bioelectrochemistry* **2007,** *70* (2), 421-434.

38. Greiner, A. J.; Pillman, H. A.; Worden, R. M.; Blanchard, G. J.; Ofoli, R. Y., Effect of Hydrogen Bonding on the Rotational and Translational Dynamics of a Headgroup-Bound Chromophore in Bilayer Lipid Membranes. *J Phys Chem B* **2009,** *113* (40), 13263-13268.

39. Setiawan, I.; Blanchard, G. J., Ethanol-Induced Perturbations to Planar Lipid Bilayer Structures. *J. Phys. Chem. B* **2014,** *118*, 537-546.

40. Setiawan, I.; Blanchard, G. J., Structural Disruption of Phospholipid Bilayers over a Range of Length Scales by n-Butanol. *J. Phys. Chem. B* **2014,** *118*, 3085-3093.

41. Mize, H. E.; Blanchard, G. J., Interface-Mediation of Lipid Bilayer Organization and Dynamics. *Phys Chem Chem Phys* **2016,** *18* (25), 16977-16985.

42. Khan, M. S.; Dosoky, N. S.; Williams, J. D., Engineering Lipid Bilayer Membranes for Protein Studies. *Int J Mol Sci* **2013,** *14* (11), 21561-21597.

43. Chakravarthy, H.; Navitskaya, S.; O'Reilly, S.; Gallimore, J.; Mize, H.; Beli, E.; Wang, Q.; Kady, N.; Huang, C.; Blanchard, G. J.; Grant, M. B.; Busik, J. V., Role of Acid Sphingomyelinase in Shifting the Balance Between Proinflammatory and Reparative Bone Marrow Cells in Diabetic Retinopathy. *Stem Cells* **2016,** *34* (4), 972-983.

44. https://www.diabetes.org/ American Diabetes Association.

45. Fong, D. S.; Aiello, L.; Gardner, T. W.; King, G. L.; Blankenship, G.; Cavallerano, J. D.; Ferris, F. L.; Klein, R., Retinopathy in Diabetes. *Diabetes Care* **2004,** *27* (1), S84-S87.

46. Chew, E. Y.; Ambrosius, W. T.; Davis, M. D.; Danis, R. P.; Gangaputra, S.; Greven, C. M.; Hubbard, L.; Esser, B. A.; Lovato, J. F.; Perdue, L. H.; Goff, D. C.; Cushman, W. C.; Ginsberg, H. N.; Elam, M. B.; Genuth, S.; Gerstein, H. C.; Schubart, U.; Fine, L. J., Effects of Medical Therapies on Retinopathy Progression in Type 2 Diabetes. *The New England Journal of Medicine* **2010,** *363* (3), 233-244.

47. Kady, N.; Yan, Y.; Salazar, T.; Wang, Q.; Chakravarthy, H.; Huang, C.; Beli, E.; Navitskaya, S.; Grant, M.; Busik, J., Increase in Acid Sphingomyelinase Level in Human Retinal Endothelial Cells and CD34+ Circulating Angiogenic Cells Isolated From Diabetic Individuals Is Associated With Dysfunctional Retinal Vasculature and Vascular Repair Process in Diabetes. *Journal of Clinical Lipidology* **2017,** *11* (3), 694-703.

48. Jiang, M.; Huang, S.; Duan, W.; Liu, Q.; Lei, M., Inhibition of Acid Sphingomyelinase Activity Ameliorates Endothelial Dysfunction in db/db Mice. *Bioscience Reports* **2019,** *39* (4), 1-10.

49. Lapinski, M. M.; Blanchard, G. J., The Role of Phospholipid Headgroups in Mediating Bilayer Organization. Perturbations Induced by the Presence of a Tethered Chromophore. *Chem Phys Lipids* **2007,** *150* (1), 12-21.

50. Meddens, M. B. M.; Keijzer, S.; Cambi, A., High Spatiotemporal Bioimaging Techniques to Study the Plasma Membrane Nanoscale Organization. *Fluorescence Microscopy* **2014**, 49-63.

51. Axelrod, D.; E., K. D.; Schlessinger, J.; Elson, E.; Webb, W. W., Mobility Measurement by Analysis of Fluorescence Photobleaching Recovery Kinetics. *Biophys. J.* **1976,** *16*, 1055-1069.

52. Ishikawa-Ankerhold, H.; Ankerhold, R.; Drummen, G., *Encyclopedia of Life Sciences*. John Wiley & Sons, Ltd.: Chichester, 2014.

53. Kijewska, K.; Blanchard, G. J., Using Diffusion To Characterize Interfacial Heterogeneity. *Langmuir* **2017,** *33* (5), 1155-1161.

54. Soumpasis, D. M., Theoretical analysis of fluorescence photobleaching recovery experiments. *Biophys. J.* **1983,** *41*, 95-97.

55. Baumler, S. M. Diffusional motion as a gauge of interfacial fluidity and adhesion of supported model membrane films. Michigan State University, 2017.

56. Brilliantov, N. V.; Denisov, V. P.; Krapivsky, P. L., Generalized Stokes-Einstein-Debye relation for charged Brownian particles in solution. *Physica a-Statistical Mechanics and Its Applications* **1991,** *175* (2), 293-304.

57. Heimburg, T., Coupling of chain melting and bilayer structure: domains, rafts, elasticity and fusion. *Membrane Science and Technology* **2003,** *7*, 269-293.

58. Frick, M.; Hofmann, T.; Haupt, C.; Schmidt, C., A novel sample preparation strategy for shotgun lipidomics of phospholipids employing multilamellar vesicles. *Analytical and Bioanalytical Chemistry* **2018,** *410* (18), 4253-4258.

59. Gupta, K.; Li, J.; Liko, I.; Gault, J.; Bechara, C.; Wu, D.; Hopper, J. T. S.; Giles, K.; Benesch, J. L. P.; Robinson, C. V., Identifying key membrane protein lipid interactions using mass spectrometry. *Nat Protoc* **2018,** *13* (5), 1106-1120.

60. Harkewicz, R.; Dennis, E. A., Applications of Mass Spectrometry to Lipids and Membranes. *Annu Rev Biochem* **2011,** *80*, 301-325.

61. Bolla, J. R.; Agasid, M. T.; Mehmood, S.; Robinson, C. V., Membrane Protein-Lipid Interactions Probed Using Mass Spectrometry. *Annual Review of Biochemistry* **2019,** *88*, 85-111.

62. Schey, K. L.; Grey, A. C.; Nicklay, J. J., Mass Spectrometry of Membrane Proteins: A Focus on Aquaporins. *Biochemistry* **2013,** *52* (22), 3807-3817.

63. Hossain, M.; Blanchard, G. J., Effects of Ethanol and *n*-Butanol on Structural Composition of Supported Lipid Bilayers via Translational Diffusion (manuscript in preparation).

64. Pillman, H. A.; Blanchard, G. J., Effects of Ethanol on the Organization of Phosphocholine Lipid Bilayers. *Journal of Physical Chemistry B* **2010,** *114*, 3840-3846.

65. Nojima, Y.; Iwata, K., Viscosity Heterogeneity inside Lipid Bilayers of Single-Component Phosphatidylcholine Liposomes Observed with Picosecond Time-Resolved Fluorescence Spectroscopy. *J. Phys. Chem. B* **2014,** *118* (29), 8631–8641.

66. González-Ramírez, E. J.; Artetxe, I.; García-Arribas, A. B.; Goñi, F. M.; Alonso, A., Homogeneous and Heterogeneous Bilayers of Ternary Lipid Compositions Containing Equimolar Ceramide and Cholesterol. *Langmuir* **2019,** *35* (15), 5305-5315.

67. Simons, K.; Ehehalt, R., Cholesterol, lipid rafts, and disease. *J Clin Invest* **2002,** *110* (5), 597-603.

68. Quinn, P. J.; Wolf, C., The Liquid-Ordered Phase in Membranes. *Biochim Biophys Acta* **2009,** *1788* (1), 33-46.

69. Lingwood, D.; Simons, K., Lipid Rafts as a Membrane-Organizing Principle. *Science* **2010,** *327* (5961), 46-50.

70. Veiga, M. P.; Arrondo, J. L.; Goñi, F. M.; Alonso, A.; Marsh, D., Interaction of Cholesterol With Sphingomyelin in Mixed Membranes Containing Phosphatidylcholine, Studied by Spin-Label ESR and IR Spectroscopies. A Possible Stabilization of Gel-Phase Sphingolipid Domains by Cholesterol. *Biochemistry* **2001,** *40* (8), 2614-2622.

71. Pralle, A.; Keller, P.; Florin, E. L.; Simons, K.; Hörber, J. K., Sphingolipid-cholesterol Rafts Diffuse as Small Entities in the Plasma Membrane of Mammalian Cells. *J Cell Biol* **2000,** *148* (5), 997-1008.

72. Eggeling, C.; Ringemann, C.; Medda, R.; Schwarzmann, G.; Sandhoff, K.; Polyakova, S.; Belov, V. N.; Hein, B.; von Middendorff, C.; Schönle, A.; Hell, S. W., Direct observation of the nanoscale dynamics of membrane lipids in a living cell. *Nature* **2008,** *457* (7233), 1159-1162.

73. Lajoie, P.; Goetz, J. G.; Dennis, J. W.; Nabi, I. R., Lattices, rafts, and scaffolds: domain regulation of receptor signaling at the plasma membrane. *J Cell Biol* **2009,** *185* (3), 381–385

74. Kenworthy, A. K.; Nichols, B. J.; Remmert, C. L.; Hendrix, G. M.; Kumar, M.; Zimmerberg, J.; Lippincott-Schwartz, J., Dynamics of Putative Raft-Associated Proteins at the Cell Surface. *J Cell Biol* **2004,** *165* (5), 735-746.

75. Lagerholm, B. C.; Weinreb, G. E.; Jacobson, K.; Thompson, N. L., Detecting Microdomains in Intact Cell Membranes. *Annu Rev Phys Chem* **2005,** *56*, 309-336.

76. Ratto, T. V.; Longo, M. L., Anomalous Subdiffusion in Heterogeneous Lipid Bilayers. *Langmuir* **2003,** *19* (5), 1788–1793.

77. Coker, H. L. E.; Cheetham, M. R.; Kattnig, D. R.; Wang, Y. J.; Garcia-Manyes, S.; Wallace, M. I., Controlling Anomalous Diffusion in Lipid Membranes. *Biophysical Journal* **2019,** *116* (6), 1085-1094.

78. Saxton, M. J., A Biological Interpretation of Transient Anomalous Subdiffusion. I. Qualitative Model. *Biophys J* **2007,** *92* (4), 1178-1191.

79. Golan, Y.; Sherman, E., Resolving mixed mechanisms of protein subdiffusion at the T cell plasma membrane. *Nature Communications* **2017,** *8* (1), 1-15.

80. Saxton, M. J., Wanted: A Positive Control for Anomalous Subdiffusion. *Biophysical Journal* **2012,** *103* (12), 2411-2422.

81. Saxton, M. J., Anomalous subdiffusion in fluorescence photobleaching recovery: a Monte Carlo study. *Biophys J* **2001,** *81* (4), 2226-2240.

82. Duncan, A. L.; Reddy, T.; Koldsø, H.; Hélie, J.; Fowler, P. W.; Chavent, M.; Sansom, M. S. P., Protein crowding and lipid complexity influence the nanoscale dynamic organization of ion channels in cell membranes. *Sci Rep* **2017,** *7*, 1-15.

83. Jackman, J. A.; Cho, N. J., Supported Lipid Bilayer Formation: Beyond Vesicle Fusion. *Langmuir* **2020,** *36* (6), 1387-1400.

84. Ferhan, A. R.; Yoon, B. K.; Park, S.; Sut, T. N.; Chin, H.; Park, J. H.; Jackman, J. A.; Cho, N. J., Solvent-assisted Preparation of Supported Lipid Bilayers. *Nat Protoc* **2019,** *14* (7), 2091-2118.

CHAPTER 5: SELECTIVE LXR AGONIST DMHCA CORRECTS RETINAL AND BONE MARROW DYSFUNCTION IN TYPE 2 DIABETES

This chapter is a modified version of a publication accepted and adapted with permission from:

Vieira, C. P.[1*]; Fortmann, S. D.[1*]; Hossain, M.[£4]; Longhini, A. L.[£1]; Hammer, S. S.[3]; Asare-Bediako, B.[1]; Crossman, D. K.[2]; Sielski, M. S.[1]; Adu-Agyeiwaah, Y.[1]; Dupont, M.[1]; Floyd, J. L.[1]; Calzi, S. L.[1]; Lydic, T.[5]; Welner, R. S.[6]; Blanchard, G. J.[4]; Busik, J. V.[3¥]; Grant, M. B.[1¥] Selective LXR agonist DMHCA corrects retinal and bone marrow dysfunction in type 2 diabetes. *JCI Insight*, **2020**, *5 (13)*, 1-21.

Institutions: [1]Department of Ophthalmology and Visual Sciences, School of Medicine, and [2]Department of Genetics, Hematology and Oncology[6] University of Alabama at Birmingham, Birmingham Alabama, 35294

Authorship note: CPV and SDF are co–first authors. MH and ALL are co–second authors. JVB and MBG are co–senior authors.

[3]Department of Physiology, [4]Chemistry and [5]Collaborative Mass Spectrometry Core, Michigan State University, East Lansing, MI 48824
*Equal contribution to first authorship
£ Equal contribution to second authorship
¥ Equal contribution to senior authorship

Abstract

In diabetic dyslipidemia, cholesterol accumulates in the plasma membrane, decreasing fluidity and thereby suppressing the ability of cells to transduce ligand-activated signaling pathways. Liver X receptors (LXRs) make up the main cellular mechanism by which intracellular cholesterol is regulated and play important roles in inflammation and disease pathogenesis. N, N-dimethyl-3β-hydroxy-cholenamide (DMHCA), a selective LXR agonist, specifically activates the cholesterol efflux arm of the LXR pathway without stimulating triglyceride synthesis. In this study, we use a multisystem approach to understand the effects and molecular mechanisms of DMHCA treatment in type 2 diabetic (db/db) mice and human circulating angiogenic cells (CACs), which

are hematopoietic progenitor cells with vascular reparative capacity. We found that DMHCA is sufficient to correct retinal and BM dysfunction in diabetes, thereby restoring retinal structure, function, and cholesterol homeostasis; rejuvenating membrane fluidity in CACs; hampering systemic inflammation; and correcting BM pathology. Using single-cell RNA sequencing on lineage$^-$sca1$^+$c-Kit$^+$ (LSK) hematopoietic stem cells (HSCs) from untreated and DMHCA-treated diabetic mice, we provide potentially novel insights into hematopoiesis and reveal DMHCA's mechanism of action in correcting diabetic HSCs by reducing myeloidosis and increasing CACs and erythrocyte progenitors. Taken together, these findings demonstrate the beneficial effects of DMHCA treatment on diabetes-induced retinal and BM pathology.

Introduction

The landmark ACCORD Eye study demonstrated that, in individuals with type 2 diabetes (T2D) and dyslipidemia, tight glycemic control supplemented with fenofibrate/statin combination significantly reduced the progression of diabetic retinopathy (DR) compared with statin supplement alone.[1] Subgroup analysis of the dyslipidemia cohort revealed that elevated LDL-cholesterol was the only individual lipid measurement that was significantly associated with worse DR progression. These data establish diabetic dyslipidemia, and hypercholesterolemia specifically, as risk factors for DR and support the notion that therapies targeting lipid metabolism are clinically efficacious in T2D.

Serum cholesterol, which reflects the cholesterol exchange between tissues, is the clinical measurement used to estimate an individual's total cholesterol level. However, the overwhelming majority of cholesterol is distributed in the cell membranes of peripheral tissues where it accounts for 30-50 % of the plasma membrane molar ratio.[2] Statins, the first line treatment for hypercholesterolemia, predominantly target cholesterol biosynthesis, and thereby decrease circulating LDL as well as peripheral cholesterol biosynthesis.[3] However, statins have a lesser effect on the efflux of intracellular cholesterol in peripheral tissues such as the retina.[4,5] In diabetic dyslipidemia, cholesterol accumulation leads to reduced membrane fluidity, inflammation, and disease pathogenesis.[6,7] Increases in membrane cholesterol promote stabilization of membrane microdomains, such as lipid rafts, which allow, for example, cytokine receptor clustering leading to increased intracellular second messenger signaling and amplification of inflammatory cytokine signaling.[8,9] In addition, cholesterol can affect membrane fluidity that is of particular importance for BM-derived cell trafficking and mobility.[10]

Liver X receptors (LXR) are the main cellular mechanism by which intracellular cholesterol is regulated. These nuclear receptors transcriptionally regulate genes involved in lipid metabolism to homeostatically balance the endogenous biosynthesis, dietary uptake, metabolism, and elimination of lipids.[11] LXR activation is induced by elevated intracellular cholesterol and stimulates cholesterol removal through reverse cholesterol transport.[12,13] In addition, LXR activation maintains the composition and physical properties of the cell membrane through the coupled regulation of phospholipid and cholesterol metabolism.[14] Activation of LXR is signaled through direct binding of endogenous lipid ligands, such as oxysterols and other cholesterol derivatives, as well as intermediate precursors in the cholesterol biosynthesis pathway.[11,12] Synthetic chemical agonists of LXR have been developed for therapeutic intervention, and while they have proven efficacious in diabetic animal models,[15-19] their undesirable adverse effect profile, including hypertriglyceridemia and hepatic steatosis, has hampered clinical development[20,21].

N, N-dimethyl-3β-hydroxy-cholenamide (DMHCA) is a synthetic oxysterol that induces gene-specific modulation of LXR.[22-24] Mechanistically, DMHCA activates LXR through direct agonism as well as the inhibition of desmosterol reduction, the final step in the predominant cholesterol biosynthesis pathway, leading to the accumulation of the potent LXR agonist desmosterol.[25, 26] During endogenous LXR activation, compensatory fatty acid biosynthesis is stimulated through the transcriptional induction of SREBP1c, leading to elevated triglyceride levels.[26] Intriguingly, DMHCA selectively activates the cholesterol efflux arm of the LXR pathway, through the induction of ATP-binding cassette transporter (ABCA1), with minimal effect on SREBP1c compared to other LXR agonists, such as T0901317 and GW3965.[25-29] Thus, DMHCA has lower risk for the undesirable adverse effects that plagued previous LXR modulators, while retaining the ability to lower circulating LDL and restore peripheral cholesterol homeostasis.[22,28]

LXR signaling plays an important role in inflammation and disease.[30] In the retina, LXR depletion causes retinal/optic nerve degeneration[31], formation of acellular capillaries[18], and retinal pigment epithelial changes[32], suggesting that LXR is required for normal retinal maintenance and that its absence results in pathologies spanning the entire retina. Interestingly, in the diabetic retina, LXR expression is downregulated, and activation of LXR using a chemical agonist is sufficient to reduce gliosis and the formation of acellular capillaries[18,19]. LXR activation also displays potent antiinflammatory effects, which are mediated, in part, by altering the composition of the plasma membrane.[33] By selectively regulating the cholesterol content of specific membrane microdomains, LXR inhibits signaling through TLRs 2, 4, and 9.[33] In diabetes, gut barrier dysfunction is an early event that increases circulating bacterial antigens, leading to enhanced activation of TLRs on endothelium and promoting chronic systemic inflammation.[34] Thus, LXR agonists, such as DMHCA, have the potential added benefit of hampering widespread inflammation in diabetes.

Additional features of diabetes are vascular insufficiency and deficient wound healing. Circulating CD34$^+$ vascular reparative cells, also known as circulating angiogenic cells (CACs), play an important role in promoting vascular integrity and maintenance.[35] These cells require a complex network of intercellular signaling to home to areas of injury and provide trophic support that promotes vascular repair. In diabetes, these cells are defective, are low in number, and their levels inversely correlate with the presence of microvascular complications, such as DR.[36,37] Cell replacement treatments using nondiabetic-derived vascular reparative cells have proven efficacious in DR mouse models[38], but drug treatments are needed that target and rejuvenate this population of circulating cells. In diabetic mice, LXR activation has been shown to restore the equivalent population of vascular reparative cells by enhancing their migration and suppressing oxidative stress and inflammatory gene expression.[18] Moreover, in LXR–double-KO mice fed a high-fat diet, circulating vascular reparative cells are dysfunctional, decreased in number, and show an increased cellular cholesterol content.[39] Interestingly, these mice also demonstrated alterations in hematopoietic stem and progenitor cells (HS/PCs), suggesting that LXR's effects may extend to the hematopoietic stem cell (HSC) compartment.[40] Together, these studies suggest that LXR modulators like DMHCA can positively impact multiple tissues and cell types in diabetes.

In this study, we use a multisystem approach to understand the effects and molecular mechanisms of DMHCA treatment in T2D db/db mice and human vascular reparative cells. Using lipidomics, single-cell membrane fluidity assays, flow cytometry, and single-cell RNA sequencing (scRNA-seq), we characterize the effects of diabetes and DMHCA treatment on the retina, circulating immune cells, and BM compartment.

Experimental

A detailed description of electroretinogram (ERG), qPCR, immunofluorescence staining, cytokines quantification, and BM analysis is included in Supplemental Methods.

Human study. Study subjects were recruited as healthy controls (n = 19) or patients with diabetes (n = 19) with either no retinopathy or with different stages of DR. Subjects were enrolled according to the criteria presented in Supplemental Table 5.1.The degree of DR was assessed using color fundus imaging and fluorescence angiography. Peripheral blood was obtained for plasma collection and CD34$^+$ cell isolation.

Human CD34$^+$ cell preparation. A total of 120 mL of peripheral blood was diluted with PBS (1:1). Then, every 25 mL–diluted blood sample was gently overlaid on 12.5 mL Ficoll-Paque Plus (catalog 17–1440-02, GE Healthcare) in 50-mL tubes. After centrifugation at 800 g for 30 minutes, the buffy coat was transferred into a new 50-mL tube and washed 3 times with PBS supplemented with 2 % FBS and 1 mM EDTA. Peripheral blood mononuclear cells were then enriched for CD34$^+$ cells by the human CD34$^+$ selection Kit (catalog 18056, Stemcell Technologies) using EasySep magnets.

Membrane fluidity. CACs isolated from control or diabetic mice and CD 34$^+$ cells were left untreated or treated with DMHCA at 10 µM overnight (16-18 hrs) in StemSpan SFEM + CC 110 media at 37 °C.

Perylene stock solution (1 mM) was prepared in dimethyl sulfoxide DMSO (Sigma Aldrich), aliquoted and stored in a -80 °C freezer. CACs were stained with 10 µM perylene for 10 min, centrifuged (0.8 or 1 x 10^3 G, 10 min, 20 °C, Fisher Scientific AccuSpin Micro 17R) to concentrate and locate cells more easily with a confocal microscope later and kept at 37 °C until use. A 0.8-μL aliquot was pipetted on a microscope slide (Thermo Scientific plain microscope slides, precleaned, 25 x 75 mm x 1 mm thick) and a cover-glass was placed on top (Corning, 22 x 22 mm of 1 mm thickness). The assembly was turned upside down and positioned on the flat stage of the FRAP instrument (*vide infra*).

FRAP Measurements. FRAP was performed as previously described.[71,72] Samples were placed on a motorized stage of a confocal scanning microscope (Nikon C2+), and images using 40X objective and 405-nm excitation laser. NIS-Elements Acquisition imaging software (v 4.30) was used for FRAP experiments, with settings of pixel dwell 1.9, size 512, normal, DAPI checked, high voltage (HV) between 90-145 (typically ~125), offset of 10, and laser power 0.71. The 40X objective was used to locate cells and region of interest (ROI) was either 3 or 2 μm diameter for human or mouse samples, respectively, one used as the stimulating spot and the other as a standard, placed in a dark, non-fluorescent spot. A continuous scanning time measurement was performed to ensure the cell did not move, indicated by a constant fluorescent intensity value over time. There was 1 minute of data acquisition (for 61 loops) at 1 sec intervals, bleaching for 1 second (4 loops) with no delay in intervals, and acquisition for another 5 min (301 loops) at 1 sec intervals. Data were fit using IGOR Pro software (WaveMetrics Inc.).

Experiment design for murine studies. Male B6.BKS(D)-Lepr^{db}/J (stock no. 000697) homozygous Lepr$^{db/db}$ were diabetic, and heterozygous Lepr$^{db/m}$ were used as controls (denoted as db/db and db/m, respectively). All mice were obtained from The Jackson Laboratory and housed in the institutional animal care facilities at the University of Alabama at Birmingham

(IACUC 20917) with strict 12-hour/12-hour light/dark cycle. Animals were considered as diabetic and used in the DMHCA treatment if the serum glucose level was above 250 mg/dL on 2 consecutive measurements. Animals have been randomly assigned to experimental groups. The animals received DMHCA (Avanti Polar Lipids) in their chow (8 mg/kg body weight/day or base diet). The animals were fed the test diets for 6 months after diabetic onset. The db/m and db/db mice were each divided in 2 subgroups, with half the mice in each group receiving control chow and the other half receiving DMHCA containing chow.

Lipid extraction. Mouse retinas were subjected to monophasic lipid extraction in methanol/chloroform/ water (2:1:0.74, v:v:v) as previously described.[73]

Analysis of free and total sterol content. Sterols and oxysterols were analyzed by high-resolution/accurate mass LC-MS using a Shimadzu Prominence HPLC equipped with an in-line solvent degassing unit, autosampler, column oven, and 2 LC-20AD pumps, coupled to a Thermo Fisher Scientific LTQ-Orbitrap Velos mass spectrometer. Lipid extracts were used directly for analysis of free sterols and oxysterols or were subjected to alkaline hydrolysis of sterol esters for analysis of total cellular sterols as previously described.[74] Gradient conditions, peak finding, and quantitation of sterols and oxysterols were performed as previously described.[75] Sterol and oxysterol identifications were performed by comparison of retention time, exact mass, and MS/MS profiles to authentic standards purchased from Steraloids.

Acellular capillaries. Eyes were fixed in 2 % formalin, and trypsin digest was performed for analysis of acellular capillaries as previously published.[76]

CFU. Analysis of CFUs was performed as previously published.[77]

Flow cytometry analysis. A total of 2×10^6 cells isolated from BM and 100 µL of peripheral blood was incubated with Ammonium Chloride solution (Stemcell Technologies, catalog 07850) for 14 minutes on ice to lyse RBCs. The cells were washed twice with PBS 2 % FBS and incubated with a cocktail of primary antibodies for 30 minutes at 4 °C in the dark; for the panel of antibodies for myeloid analysis, refer to Supplemental Table 5.2. To quantify precursor cells in the BM, 1×10^6 cells were incubated with a cocktail of antibodies containing c-Kit (CD117), viability dye 510, FcyRII/III, Sca-1, lineage cocktail, CD34, FLT3 (CD135), and CD127; for the panel of antibodies for precursor analysis, refer to Supplemental Table 5.3. After washing, the cells were acquired on BD FACSCelesta. Retina cells were isolated by incubating the entire retina with the digesting buffer (RPMI 5 % FBS, 10 µg/ mL collagenase D, and 300 U/mL DNase) for 1 hour at 37 °C. The suspension of cells was filtrated in a 40-µm cell strainer and incubated with a cocktail of antibodies containing anti-F4/80, viability dye 510, Ly6G, CD45, CD11b, CCR2, CD133, CD206, Ly6C, and Flk-1; for the list of antibodies, refer to Supplemental Table 5.4. All the flow cytometry analyses were performed using FlowJo software (Tree Star Inc.).

10X Genomics single cells. For scRNA-seq, BM single-cell suspensions were generated from 9-month-old untreated and DMHCA-treated db/db mice. Briefly, BM cells were aspirated from femur samples and filtered through 40 µm mesh. Single-cell suspensions were column enriched for Sca-1^+, FACS sorted using lineage$^-$ and c-Kit1^+ markers and assayed for viability using trypan blue. Viable cells were then run through the 10X genomics platform for droplet-based single-cell barcoding and cDNA generation. Illumina HiSeq was used for cDNA sequencing. The 10X Genomics Software Cell Ranger (version 3.1.0) was used for quality control of sequencing reads, FASTQ file generation, and demultiplexing. The STAR software was used for read alignment using the mouse mm10 reference genome.

scRNA-seq data analysis. For scRNA-seq data analysis, multiple software platforms were used, including Scanpy, Monocle, and Seurat.[78] For transcript quality control, Scanpy was used to plot histograms of total counts per cell and genes per cell, which were then used to identify cutoffs that eliminated doublets and damaged cells. Additionally, a mitochondrial gene percentage cutoff of 20 % was used to further eliminate damaged cells. After quality control, 5103 cells were recovered from the untreated diabetic group and 5152 cells from the DMHCA-treated group, for a total of 10,255 cells. The 2 treatment groups were then concatenated to form a single data file, and a minimum cutoff of 10 cells per gene was used to eliminate lowly represented genes. Normalization was performed using Scran, which employs a pooling-based size factor estimation method to normalize single-cell transcript data across heterogenous cell populations.[79] Scanpy was then used to perform complete cell cycle regression using the cell cycle genes identified by Tirosh *et al.*.[80] ComBat was used for batch correction with cell cycle scores included as covariates.[81] Scanpy was then used to select 4500 highly variable genes, and the uniform manifold approximation and projection (UMAP) plot was generated using a resolution of 0.8. Subclustering was then performed to arrive at the final UMAP representation of 13 clusters. Scanpy was used to identify marker genes for each cluster. The assignment of cluster identities was guided by the expression of lineage-specific marker genes identified in previous scRNA-seq data sets on murine HSCs.[82] In the case of undefined cell populations, clusters were identified based on their unique expression patterns and the presence/absence of lineage-specific markers. Compositional analysis was done using Scanpy.

To identify differentially expressed genes across total samples or specific cluster subpopulations, Model-based Analysis of Single-cell Transcriptomics (MAST) was used and the analysis included the technical covariate number of genes expressed per cell.[83] An FDR cutoff of 0.01 was used in the total sample DGE, while a cutoff of 0.05 was used in the subpopulation analyses. Pathway enrichment analysis was performed using Ingenuity Pathways Analysis (IPA; QIAGEN), with all canonical pathways used in the total sample DGE and secondary messenger/intracellular signaling pathways in the subpopulation analyses.

Transcription factor activity was analyzed with the pySCENIC package using the preprocessed raw count matrices.[84] Pseudotime trajectory analysis was performed using Monocle with the naive B cell population removed and max components set to 3. PAGA analysis was performed using the preprocessed data file with the threshold set to 0.07. Seurat was used to graph the violin plots.

Statistics. All data sets were assessed for normality against a Gaussian Distribution via the Shapiro-Wilks test. Data composed of more than 2 individual groups that were determined to be normally distributed were subjected to a 1-way parametric ANOVA with Tukey’s test for multiple comparisons. Data composed of more than 2 individual groups that were determined to be nonnormally distributed were subjected to a Kruskal-Wallis test with multiple comparison correction via Dunn’s test. A value of $P < 0.05$ was considered to be statistically significant for all tests. All values are expressed as mean ± SEM. Statistical tests were performed using statistics software (GraphPad Software).

Study approval. All human studies were approved by the IRBs at the University of Alabama (IRB-300000068). All mice were housed in the institutional animal care facilities at the University of Alabama at Birmingham (IACUC 20917).

Results

Systemic DMHCA treatment restores cholesterol homeostasis in the diabetic retina. Dysregulation of the delicate balance between cholesterol biosynthesis, uptake, and removal leads to accumulation of cholesterol in the diabetic retina. To test whether selective LXR agonism, using systemic DMHCA treatment (Figure 5.1A), is sufficient to reduce the levels of cholesterol in the retina, T2D db/db mice were treated with oral DMHCA for 6 months after the onset of diabetes. Liquid chromatography–mass spectrometry (LC-MS) was performed on lipid extracts from whole retina to quantify sterol levels before (nonesterified cholesterol and sterol metabolites) and after alkaline hydrolysis (esterified and nonesterified cholesterol).

The retinal sterol profiles of db/m heterozygous controls, db/db diabetic mice, and db/db diabetic mice treated with DMHCA are represented by the heatmap in Figure 5.1B. DMHCA significantly increased endogenous LXR ligands, desmosterol, and total oxysterols in the diabetic retina, consistent with the drug's mechanism of action (Figure 5.1, C and D). The total cholesterol content of the diabetic retina was over 2 magnitudes higher than db/m control, consistent with diabetic dyslipidemia (Figure 5.1E). DMHCA treatment reduced total retinal cholesterol by over a magnitude in the diabetic animals, bringing it back to baseline levels (Figure 5.1E). Compared with db/m controls, DMHCA also significantly reduced nonesterified cholesterol (Figure 5.1F).

In addition to inhibition of cholesterol synthesis, DMHCA increased cholesterol removal through activation of LXR-induced reverse cholesterol transport and modified cholesterol metabolism to favor the synthesis of more soluble oxysterols. Indeed, DMHCA treatment increased free oxysterols by > 50 % (Figure 5.1D). In addition to DMHCA and desmosterol, many other oxysterol species serve as endogenous LXR agonists.[41] Consistent with LXR agonism, DMHCA treatment increased the LXR-controlled transcriptional expression of the cholesterol efflux pump ABCA1 by over 100 % in the diabetic retina (Figure 5.1G). Together, these data demonstrate the dramatic shift in the cholesterol metabolism in the diabetic retina and provide support that systemic DMHCA treatment can restore cholesterol homeostasis in the retina.

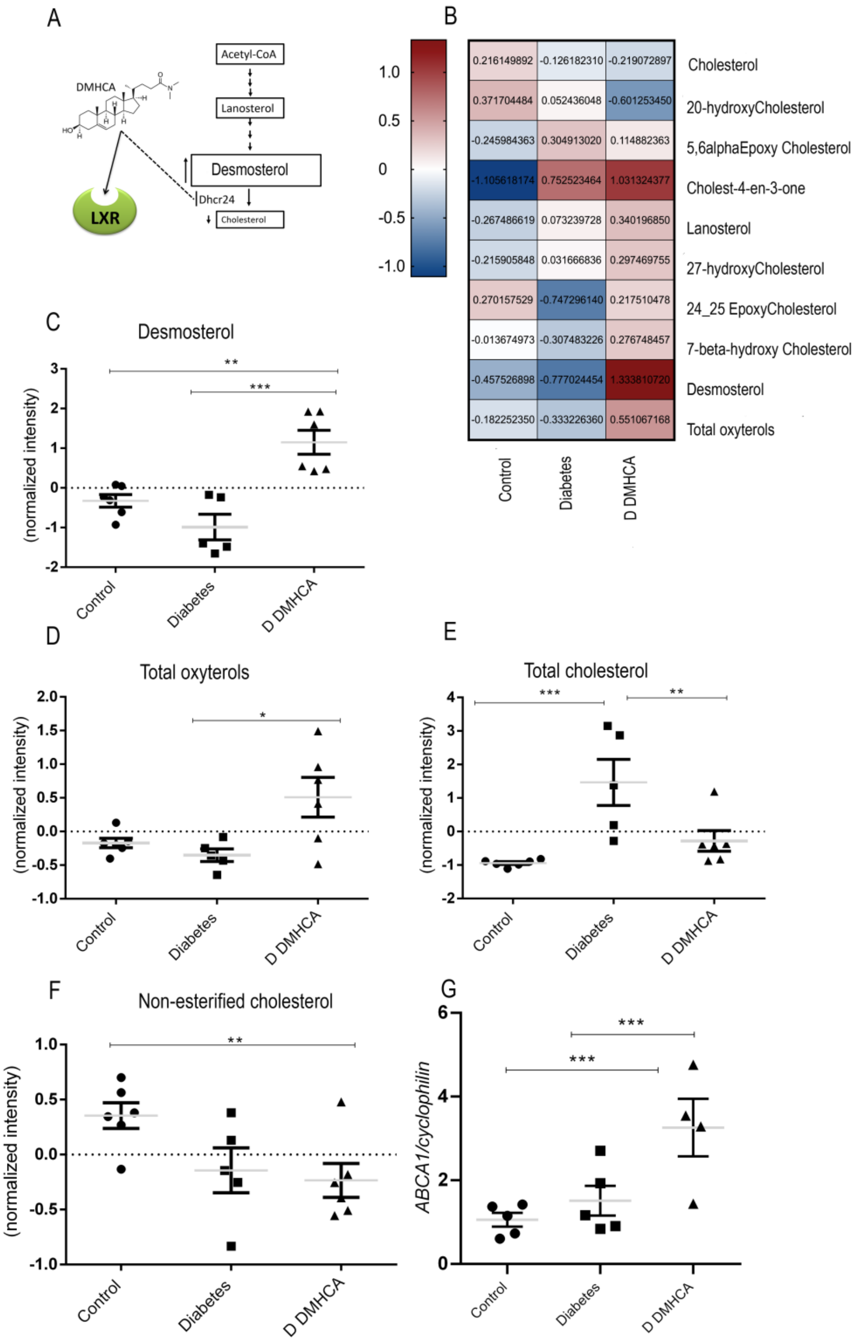

	Control	Diabetes	D DMHCA
Cholesterol	0.216149892	-0.126182310	-0.219072897
20-hydroxyCholesterol	0.371704484	0.052436048	-0.601253450
5,6alphaEpoxy Cholesterol	-0.245984363	0.304913020	0.114882363
Cholest-4-en-3-one	-1.105618174	0.752523464	1.031324377
Lanosterol	-0.267486619	0.073239728	0.340196850
27-hydroxyCholesterol	-0.215905848	0.031666836	0.297469755
24_25 EpoxyCholesterol	0.270157529	-0.747296140	0.217510478
7-beta-hydroxy Cholesterol	-0.013674973	-0.307483226	0.276748457
Desmosterol	-0.457526898	-0.777024454	1.333810720
Total oxyterols	-0.182252350	-0.333226360	0.551067168

Figure 5.1. DMHCA restores cholesterol homeostasis in diabetic retina. (**A**) Schematic representation of DMHCA structure and function. (**B**) Compounds selected by One-way ANOVA with p-value threshold of 0.05 are shown in the heatmap of LC-MS quantified free retinal sterols from 9 month old mice. Quantification of desmosterol (**C**), total oxysterols (**D**), total cholesterol (**E**), and non-esterified cholesterol (**F**). Data are LC-MS peaks normalized to internal standards, log transformed and Pareto-scaled, presented as mean ± SEM. (**G**) RT-qPCR of retinal ABCA1 mRNA expression. $*P < 0.05$; $**P < 0.03$ $***P < 0.01$ analyzed using One-Way parametric ANOVA with Tukey's Test for multiple comparisons.

DMHCA rescues diabetes-induced membrane rigidity in circulating vascular reparative cells in mice and humans. In diabetes, buildup of cholesterol impedes the fluidity of the plasma membrane, causing a pathologic increase in the rigidity of the cell.[41-44] To test whether the observed improvements in cholesterol metabolism with DMHCA treatment could rescue this diabetic phenotype, we used an ex vivo imaging approach to quantify the effects of DMHCA on membrane fluidity of stem/progenitor cells from diabetic individuals and mice. For human studies, peripheral $CD34^+$ cells, a vascular reparative population, were collected from 19 individuals with T2D and from 19 nondiabetic control subjects (Supplemental Table 5.1); supplemental materials are located after the references section. We chose to focus on $CD34^+$ cells because membrane fluidity is especially important in this population, which require membrane flexibility to egress from the BM and a complex network of lipid rafts to transduce activation signals. Compared with the control cells (n = 136), the membrane fluidity of diabetic $CD34^+$ cells (n = 89) - as assessed by fluorescence recovery after photobleaching (FRAP) - was significantly reduced (Figure 5.2, A and B). This is consistent with the well-described dysfunction of $CD34^+$ in diabetes, leading to a reduced ability to correct chronic vascular injury such as occurs in DR. Remarkably, ex vivo treatment of diabetic $CD34^+$ cells with DMHCA for 16–18 hours restored the fluidity of the membranes to baseline nondiabetic levels (Figure 5.2B). These data demonstrate that DMHCA restores the structure, and presumably function, of dysfunctional $CD34^+$ vascular reparative cells.

A similar approach was used to assess the ex vivo ability of DMHCA to correct the membrane fluidity of CACs in diabetic mice. CACs were defined as $CD45^+CD11b^-CD133^+FLK1^+$ peripheral circulating cells (Supplemental Figure 5.1). Compared with control cells (n = 11), CACs from db/db mice (n = 12) showed increased membrane rigidity, similar to what was observed in diabetic human–derived CD34$^+$ cells (Figure 5.2, C and D). After 16-18 hours of ex vivo DMHCA treatment, the membrane fluidity of diabetic CACs (n = 17) was rescued to above-baseline nondiabetic levels (Figure 5.2D). These data complement those observed in the human studies and demonstrate the potent ability of DMHCA to acutely correct membrane rigidity.

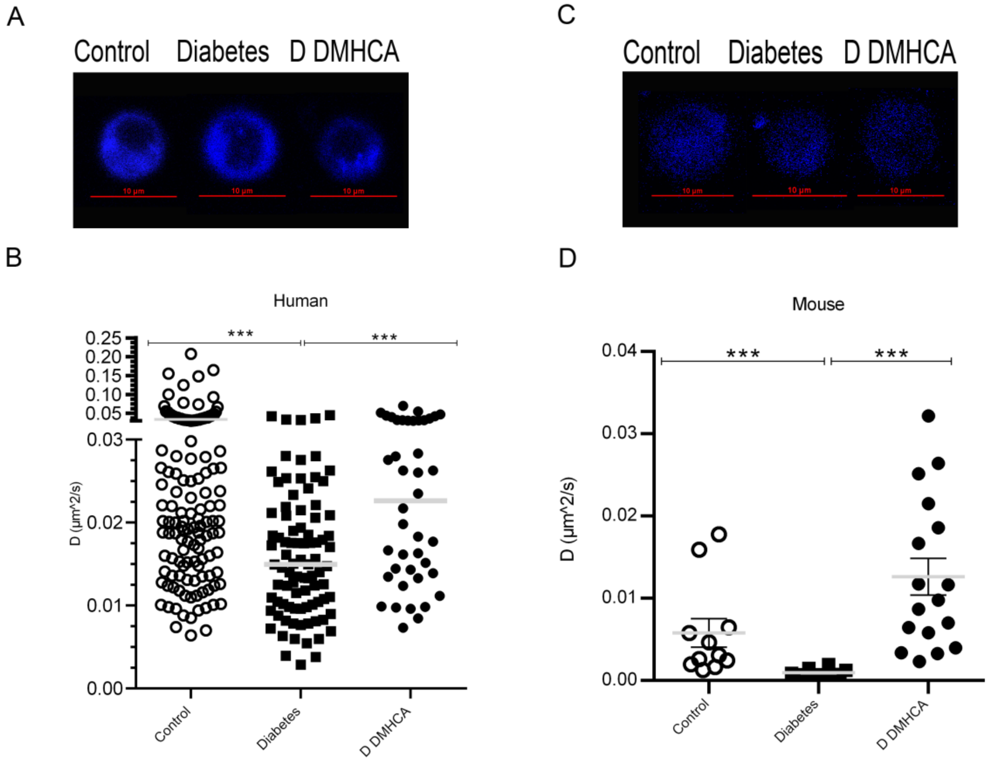

Figure 5.2. DMHCA rescues membrane fluidity in circulating vascular reparative cells in humans and mice. (**A** and **B**) CD34$^+$ cells were enriched from peripheral blood samples from nondiabetic (n = 19) and type 2 diabetic (n = 19) patients. Representative single-cell images of membrane staining from nondiabetic, diabetic (untreated), and DMHCA-treated diabetic CD34$^+$ cells (**A**). Translational diffusion values from patient-derived CD34$^+$ circulating vascular reparative cells. Control, nondiabetic cells (n = 136); diabetes, untreated diabetic cells (n = 89); D DMHCA, DMHCA-treated diabetic cells (n = 42) (**B**). (**C** and **D**) CACs were isolated from BM of nondiabetic (db/m; n = 11) and diabetic (db/db; n = 29) mice. Representative single-cell images of membrane staining from nondiabetic, diabetic (untreated), and DMHCA-treated diabetic CACs (**C**). Translational diffusion values from CACs. Control, nondiabetic cells (n = 11); diabetes, untreated diabetic cells (n = 12); D DMHCA, DMHCA-treated diabetic cells (n = 17) (**D**). Data are presented as mean ± SEM. $^*P < 0.05$; $^{**}P < 0.03$; $^{***}P < 0.01$. Analyzed using Kruskal-Wallis test with multiple comparison correction via Dunn's test.

DMHCA slows the progression of DR in db/db mice. Given the remarkable ability of DMHCA to restore cholesterol homeostasis in the diabetic retina and to rescue the membrane fluidity of circulating vascular reparative cells in diabetes, we next sought to explore the functional impact of these beneficial effects on the progression of DR. Similar to humans, diabetic db/db mice develop progressive retinal pathology that shares many key features with DR, including increased infiltration of proinflammatory leukocytes, formation of acellular capillaries, and reduced visual response.[45,46] To assess the antiinflammatory effects of DMHCA on the diabetic retina, flow cytometry was used to quantify the relative percentages of infiltrating monocytes/macrophages. To isolate macrophages and monocytes, $CD45^+CD11b^+$ cells were gated on the macrophage marker F4/80 (Supplemental Figure 5.2). Macrophages were further gated on CD206 to isolate M1-like $CD206^–$ macrophages and M2-like $CD206^+$ macrophages, while monocytes were gated on CCR2 to isolate classical $CCR2^–$ monocytes from nonclassical $CCR2^+$ monocytes (Supplemental Figure 5.2). Compared with control, diabetes induced a relative increase in classical monocytes and proinflammatory M1-like macrophages and a decrease in nonclassical monocytes and reparative M2-like macrophages (Figure 5.3, A and B). Systemic DMHCA treatment rescued nearly all of these defects in the proinflammatory state of the diabetic retina. DMHCA reduced the relative proportion of classical monocytes to below baseline, restored the proportion of nonclassical monocytes to baseline, and increased the proportion of reparative M2-like macrophages (Figure 5.3, A and B).

Consistent with these data, the absolute number of leukocytes in retinal cross-sections stained with CD45 were increased in untreated diabetes compared with control, and DMHCA treatment significantly reduced the number of infiltrating $CD45^+$ leukocytes (Figure 5.3C). Furthermore, the transcript level of CCL-2, a hypoxia-induced monocyte chemoattractant, was significantly increased in the untreated diabetic retina compared with control, and DMHCA restored the CCL-2 transcript level to baseline (Figure 5.3D).

A hallmark feature of DR is microvascular dropout, which promotes retinal ischemia in diabetes. Compared with control, the number of acellular capillaries in the untreated diabetic retina was significantly increased (Figure 5.3E). DMHCA protected the diabetic retina from microvascular dropout, reducing the number of acellular capillaries to baseline levels (Figure 5.3E). These data further support the structural benefits allowed by DMHCA treatment on the diabetic retina. To assess whether these structural improvements have functional significance in DR, electroretinography was used to quantify the visual response of the retina. Compared with control, the untreated diabetic retina showed significant decreases in scotopic a-and b-waves, consistent with diabetes-induced visual dysfunction (Figure 5.3F). DMHCA treatment restored visual function in the diabetic animals and increased scotopic b-waves closer to baseline levels (Figure 5.3F). Together, these data demonstrate the beneficial effects of DMHCA treatment on the inflammatory state, vascular integrity, and visual function of the diabetic retina.

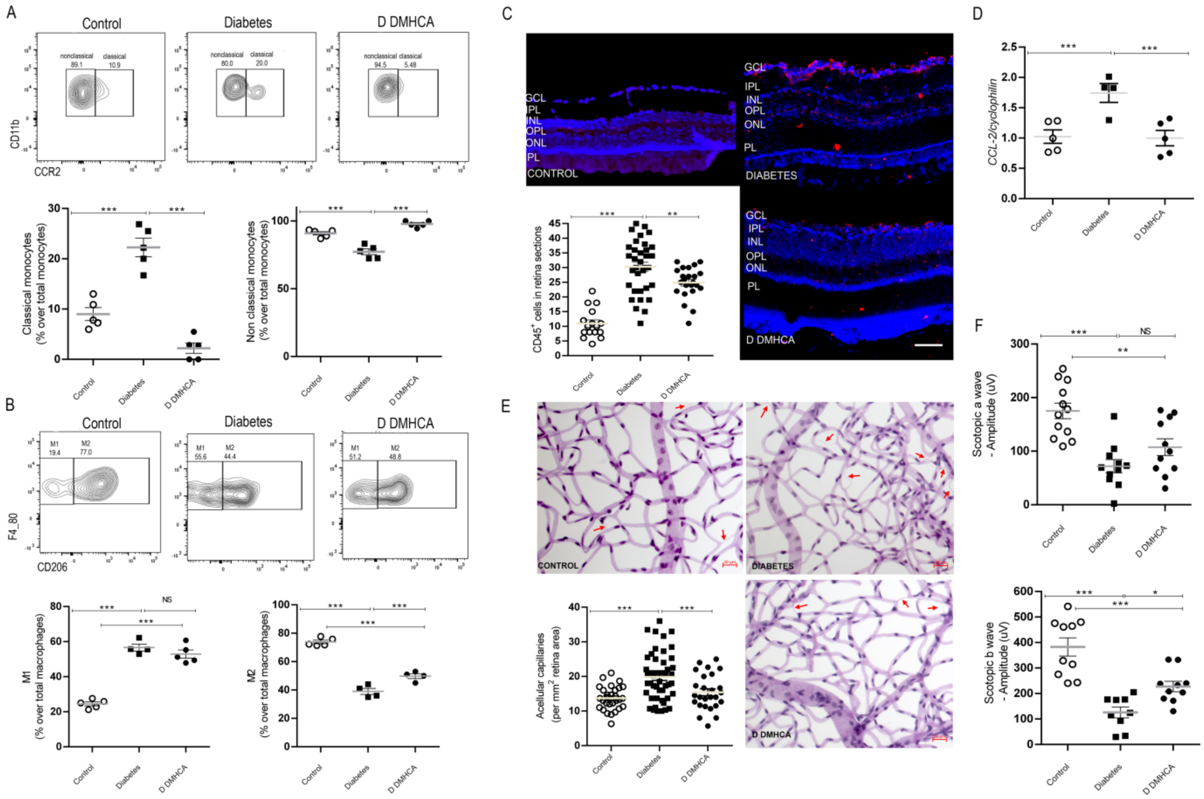

Figure 5.3. DMHCA retards the development of diabetic retinopathy in db/db mice. (**A**) The presence of inflammatory and antiinflammatory cells in the retina were determined by flow cytometry. Monocytes were defined by $CD45^{+}CD11b^{+}Ly6G^{-}F4/80^{-}$ cells, classical monocytes were determined as $CCR2^{+}$ cells, and nonclassical monocytes as $CCR2^{-}$. (B) The macrophages were defined as $CD45^{+}CD11b^{+}Ly6G^{-}F4/80^{+}$ cells, and then the $CD206^{-}$ cells were gated to quantify M1 macrophages and the $CD206^{+}$ to quantify M2 macrophages. (C) Immunofluorescence staining of retinal cross-sections for $CD45^{+}$ cells. GCL, ganglion cell layer; IPL, inner plexiform layer; INL, inner nuclear layer; OPL, outer plexiform layer; ONL, outer nuclear layer; PL, photoreceptor layer. (D) qPCR on retinal CCL-2 mRNA expression. (E) Trypsin digested retinal flat mounts for acellular capillary quantification. (F) Retinal visual response assessed by electroretinography. Scotopic a- and b-waves were quantified at an intensity of 0 db flash (3 $cd/m^2/s$). Data are the mean ± SEM. $^{**}P < 0.03$ $^{***}P < 0.01$. Analyzed using 1-way parametric ANOVA with Tukey's test for multiple comparisons.

DMHCA reduces the proinflammatory state of the BM and increases the egression of vascular reparative cells into the peripheral circulation. In diabetes, low-level chronic inflammation alters the homeostatic balance of nearly all tissues, including the BM microenvironment.[47] Myeloidosis, defined as an increase in the proportion of myeloid-derived leukocytes, is a common feature in diabetic BM and promotes the systemic inflammatory phenotype.[48] Based on the observed antiinflammatory effects of DMHCA on the diabetic retina, we asked whether the benefits afforded by systemic DMHCA treatment extended to the level of the BM microenvironment and the systemic circulation. Compared with control, cytometry bead array and ELISA analyses of BM supernatants from untreated diabetic mice displayed significant increases in the protein levels of secreted proinflammatory molecules, including TNF-α, IL-3, and CCL-2. Remarkably, DMHCA treatment restored the levels of BM-derived TNF-α and IL-3 to baseline and significantly reduced CCL-2 production by > 50 % (Figure 5.4, A–C). These data are consistent with DMHCA's ability to hamper the proinflammatory microenvironment of the diabetic BM.

Next, flow cytometry was used to profile specific populations of leukocytes in the BM and peripheral circulation (Supplemental Figure 5.3). Compared with control, diabetes induced a significant increase in the number of circulating monocytes but surprisingly had no effect on the total monocyte population of the BM (Figure 5.4D). DMHCA treatment significantly reduced the number of circulating monocytes in diabetic mice (Figure 5.4E). We next focused on vascular reparative cells in the BM and circulation. As previously reported, diabetes induced a significant decrease in the total proportion of CACs in the BM and peripheral circulation (Figure 5.4, F and G). Compared with untreated diabetic mice, DMHCA significantly increased the number of CACs in the BM and peripheral circulation (Figure 5.4, F and G). These findings complement the previous data showing enhanced membrane fluidity in DMHCA-treated CACs and suggest that the improvements in membrane fluidity may account for the observed increase in CAC egression into the peripheral circulation.

Taken together, these data demonstrate that systemic DMHCA treatment has the additional benefit of preventing diabetes-induced myeloidosis and enhancing the egression of vascular reparative cells into the peripheral circulation.

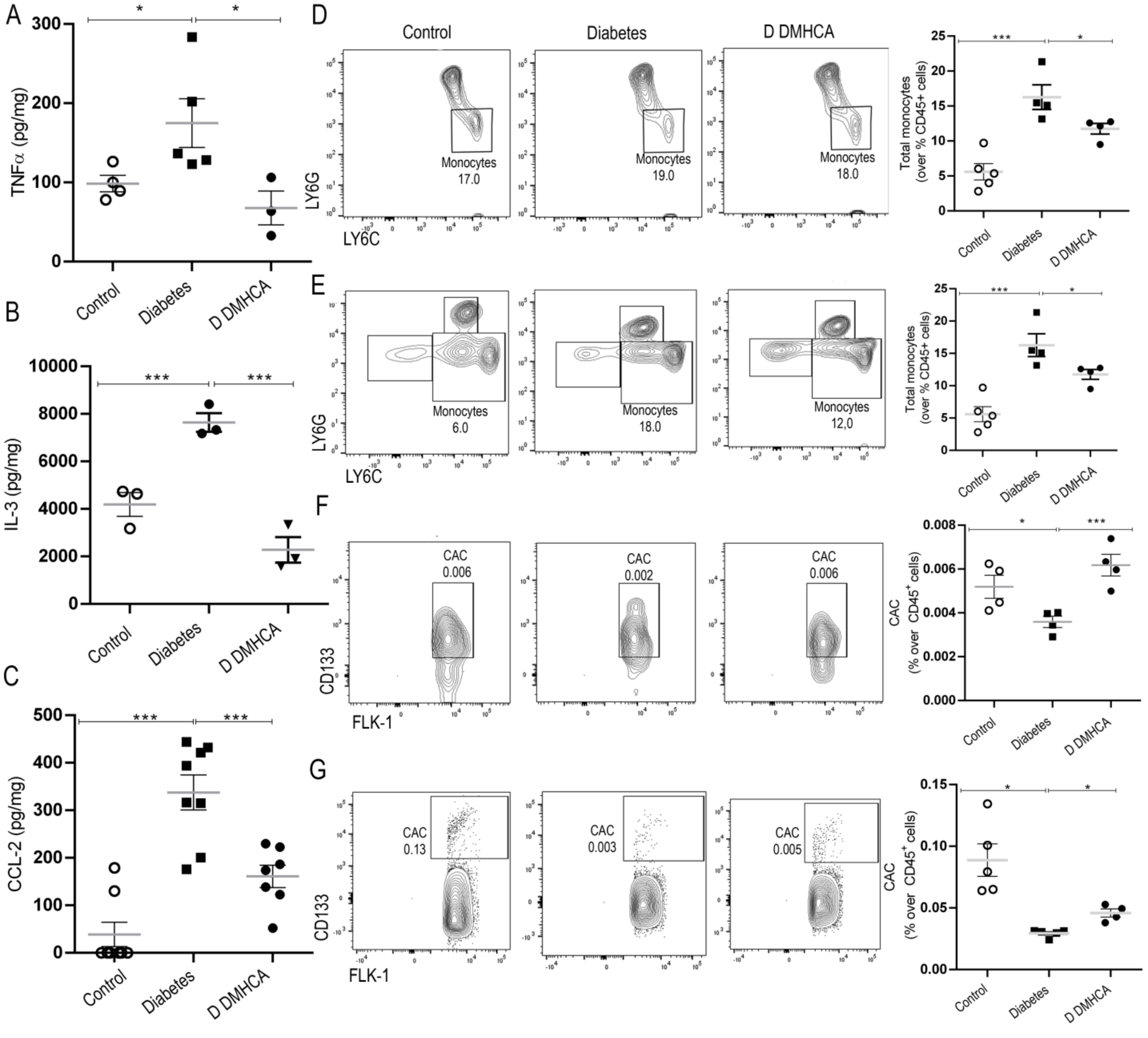

Figure 5.4. DMHCA reduces the inflammation in BM and increases the migration of vascular reparative cells into the systemic circulation. (**A**–**C**) TNF-α (**A**) and CCL-2 (**C**) were quantified by Cytometry beads array, and IL-3 was quantified by ELISA (**B**). (**D** and **E**) Monocytes from BM (**D**) and peripheral blood (**E**) were quantified by flow cytometry and defined as CD45$^+$CD11b$^+$Ly6G$^-$LY6C$^+$ cells. (**F** and **G**) Flow cytometry analysis of levels of circulating angiogenic cells (CAC) were determined as CD45$^+$CV11b$^-$CD133$^+$FLK1$^+$ cells of BM (**F**) and peripheral blood (**G**). Data are the mean ± SEM. *$P < 0.05$; ***$P < 0.01$ analyzed using 1-way parametric ANOVA with Tukey's test for multiple comparisons.

DMHCA acts at the level of HS/PCs to correct diabetic myeloidosis. To better understand the mechanism by which DMHCA normalizes the composition of circulating leukocytes, we next focused on the HSC compartment. During hematopoiesis, differentiation signals instruct HSCs to favor specific lineages, and a homeostatic balance of these signals is necessary to maintain equilibrium of circulating cells. In certain pathologic states, this balance becomes uneven, leading to the accumulation of a particular lineage, such as in diabetic myeloidosis. To explore the HSC compartment, we gated on lineage$^{–}$SCA1^{+}c-KIT^{+} (LSK) BM cells (Supplemental Figure 5.4). CD34^{+}FLT3^{+} multipotent progenitors (MPPs) accounted for the largest majority of LSK cells, followed by CD34^{+}FLT3$^{–}$ short-term HSCs (ST-HSCs) and finally CD34$^{–}$FLT3$^{–}$ long-term HSCs (LT-HSCs). Compared with controls, untreated diabetic LSK cells displayed decreased ST-HSCs and LT-HSCs and increased MPPs (Figure 5.5, A-D). In the treated diabetic cohort, DMHCA significantly reduced the proportion of MPPs back to baseline and increased LT-HSCs (Figure 5.5, A, B, and D). These data support the notion that DMHCA is sufficient to restore the HSC compartment in diabetes toward a nondiabetic state.

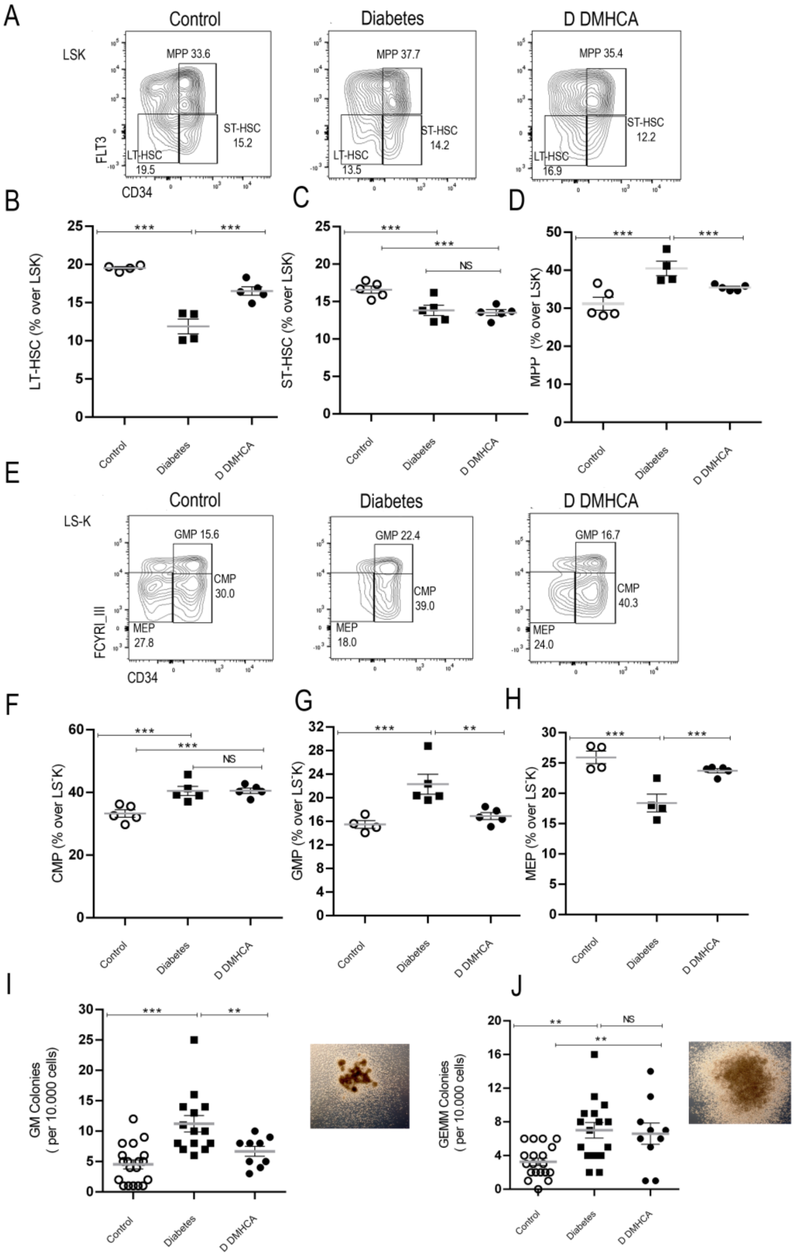

Figure 5.5. DMHCA corrects hematopoietic stem and progenitor dysfunction in db/db mice. (**A**–**H**) BM HSC (**A**–**D**) and HPC (**E**–**H**) was assessed by flow cytometry. HSCs were defined as Lin$^-$ Sca1$^+$c-Kit$^+$ (LSK) BM cells (**A**). LT-HSCs were defined as CD34$^-$FLT3$^-$ (**B**), ST-HSCs as CD34$^+$FLT3$^-$ (**C**), and MPPs as CD34$^+$FLT3$^+$ (**D**). HPCs were defined as LSK BM cells (**E**). CMPs were defined as CD32/CD16$^-$CD34$^+$ (**F**), GMPs as CD32/CD16$^+$CD34$^+$ (**G**), and MEPs as CD32/CD16$^-$CD34$^-$ (**H**). CFU assays for ex vivo differentiation of cultured HPCs (**I** and **J**). Granulocyte, macrophage (GM) CFUs (**I**) and granulocyte, erythroid, macrophage, megakaryocyte (GEMM) CFUs (**J**). Data are presented as mean ± SEM. $^{**}P < 0.03$; $^{***}P < 0.01$. Analyzed using 1-way parametric ANOVA with Tukey's test for multiple comparisons.

Lineage-committed progenitor populations (LSK) were examined next to determine the effect of DMHCA on hematopoietic lineage flux (Figure 5.5E). CD32/CD16–CD34+ common myeloid progenitors (CMPs) accounted for the largest percentage of cells, followed by CD32/CD16$^+$CD34$^+$ granulocyte myeloid progenitors (GMPs) and finally CD32/CD16$^-$CD34$^-$ megakaryocyte-erythrocyte progenitors (MEPs). Untreated diabetic mice showed an increase in CMPs and GMPs and a decrease in MEPs, consistent with diabetic myeloidosis (Figure 5.5, F–H). Again, DMHCA treatment corrected many of the defects observed in the lineage-committed progenitor populations in diabetes. DMHCA significantly reduced the number of GMPs, suggesting a decrease in the production of neutrophils and monocytes (Figure 5.5G). This is consistent with our previous observations demonstrating reduced circulating monocytes with DMHCA treatment and suggests that the mechanism relates, at least partially, to the ability of DMHCA to correct diabetic myeloidosis. In addition, DMHCA treatment significantly increased the proportion of MEPs to baseline levels, suggesting an increase in the production of erythrocytes and megakaryocytes (Figure 5.5H).

Finally, we assessed the differentiation ability of BM-derived stem and progenitor cells using an ex vivo culture assay. BM from control, diabetic, and DMHCA-treated mice was enriched for progenitor markers and grown in culture for 12 days, after which the number of CFUs was counted. In BM from untreated diabetic mice, there were significantly more granulocyte, erythroid, macrophage, megakaryocyte CFUs (GEMM-CFUs) and granulocyte, macrophage CFUs (GM-CFUs) compared with control, again consistent with diabetic myeloidosis (Figure 5.5I). In diabetic mice treated with DMHCA, the number of GM-CFUs was reduced to baseline levels, while no effect was observed on GEMM-CFUs (Figure 5.5J).

Together, these data suggest that DMHCA acts at the level of HS/PCs to fundamentally shift diabetic hematopoiesis toward a more normal nondiabetic state. Remarkably, this effect is sufficient to suppress diabetic myeloidosis.

Single-cell analysis of diabetic HSCs in DMHCA-treated mice. To gain mechanistic insight into DMHCA's ability to influence diabetic HSCs and progenitors, scRNA-seq was performed on LSK sorted BM cells. Briefly, LSK cells were pooled from 3 age-matched mice for each cohort (untreated db/db and DMHCA treated db/ db). Raw-count matrices from the 2 groups were preprocessed separately to remove low-quality cells and then merged for further processing using size-factor normalization, cell cycle regression, and empirical Bayes modeling for batch correction. A total of 5103 cells were recovered from the untreated diabetic group and 5152 cells from the DMHCA-treated diabetic group, for a total of 10,255 HSCs. Unsupervised clustering revealed 13 distinct clusters (Figure 5.6A). The largest population of cells, accounting for 27 % of the total combined sample, was multipotent stem cells (Figure 5.6E). These cells were identified by high expression of the stem cell markers CTLA2A, HLF, and CD34 and the absence of lineage-specific gene expression (Figure 5.6B). Gene expression patterns of all major lineages were represented in the single-cell analysis, albeit at varying levels. These include DC progenitors (CD74, H2-AA, and H2-EB1 high), erythrocyte progenitors (HBB-BT high), lymphoid progenitors (DNTT high), monocyte progenitors (IRF8 and LY86 high), megakaryocyte/basophil progenitors (VWF and GATA2 high), neutrophil progenitors (MPO and CTSG high), and pre-B and T cell progenitors (EBF1/CD19 high and TRBC1 high, respectively) (Figure 5.6, B and C).

While the cluster distributions appear similar between the 2 groups (Figure 5.6D), differences are noted in the proportions of individual clusters (Figure 5.6E). In the DMHCA treatment group, multipotent stem cells decreased by 8.8 % (Figure 5.6E). This is consistent with our previous finding that DMHCA reduces the pathologic increase of MPPs in diabetic BM. Additionally, DMHCA increased the relative proportion of erythrocyte progenitors by 39 % (Figure 5.6E). This is consistent with our previous observation of increased MEPs in DMHCA-treated BM. Interestingly, a potentially novel population of stem cells was identified, which we refer to as AP1-high stem cells. This relatively small population, accounting for roughly 3 % of the total sample, was identified as expressing high levels of the activator protein 1 (AP1) complex - including FOS, FOSB, JUN, JUNB, and JUND - and largely lacked expression of lineage-specific genes (Figure 5.6B). In the DMHCA treatment group, this AP1-high stem cell population was increased by 54 % (Figure 5.6E). Moreover, DMHCA treatment unexpectedly increased the relative proportion of both pre-B and naive B cells (Figure 5.6E). Last, of note is the lack of change observed in the neutrophil and monocyte progenitor populations (Figure 5.6E). This suggests that DMHCA's ability to influence these cells and correct diabetic myeloidosis may occur at a later stage in hematopoiesis.

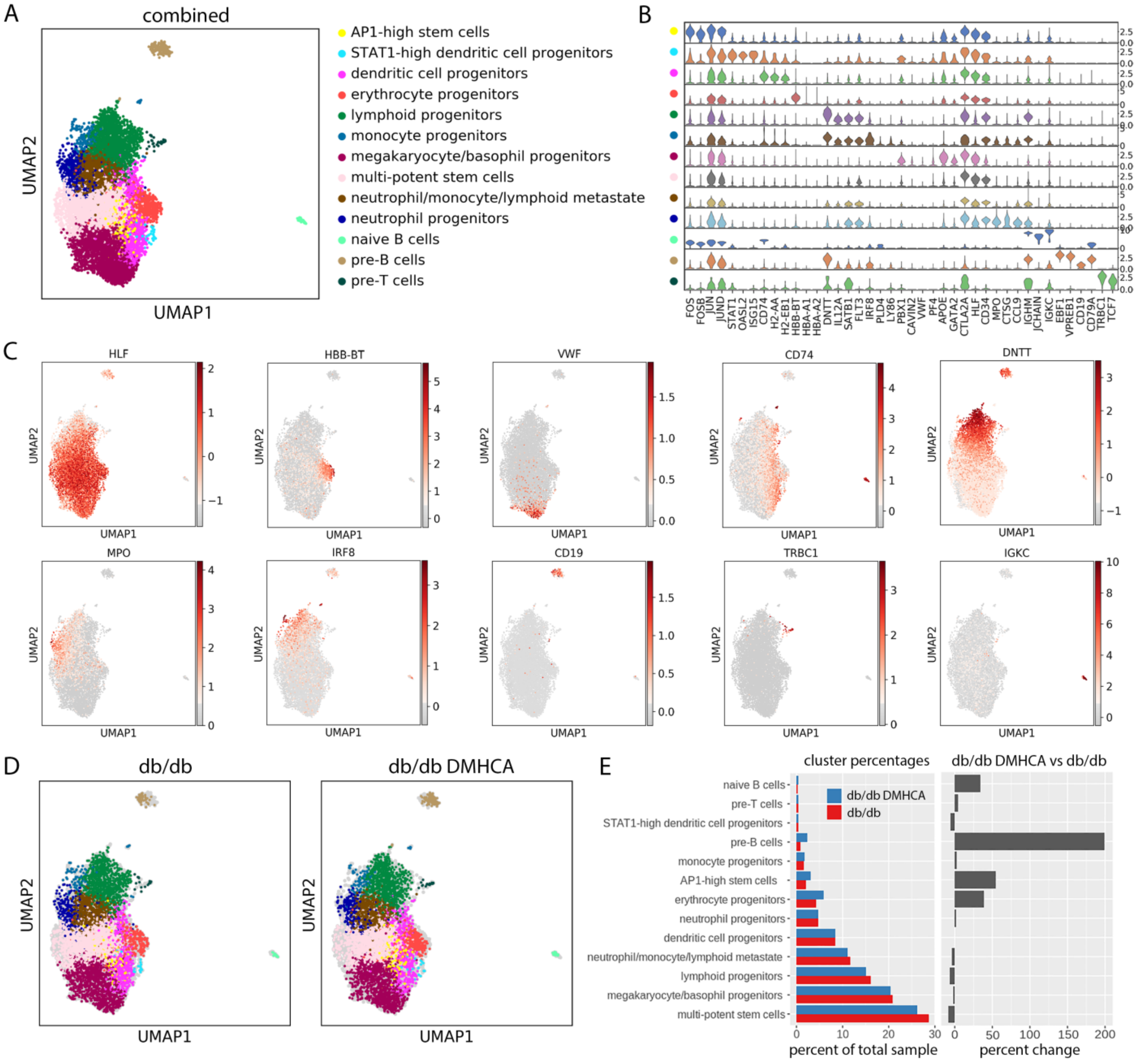

Figure 5.6. Single-cell RNA-seq analysis of untreated and DMHCA treated diabetic HSCs. (**A**) UMAP representation of scRNA-seq from LSK sorted HSCs reveals 13 distinct clusters. (**B**) Violin plots of lineage-specific gene expression across all 13 clusters. (**C**) Spatial representation of lineage-specific gene expression. (**D**) UMAP cluster representations of untreated (db/db) and DMHCA treated (db/db DMHCA) diabetic HSCs. (**E**) Cluster proportions of all 13 cell populations in untreated and DMHCA-treated samples.

DMHCA treatment increases expression of immediate early-response genes. To probe the transcriptional pathways responsible for DMHCA's effect on diabetic HSCs, we performed differential gene expression (DGE) analysis on the total DMHCA-treated group compared with the untreated control. Using an FDR cutoff of 0.01 and accounting for technical covariates, we identified 1048 differentially expressed genes (Figure 5.7A). The majority of DGEs were increased with DMHCA and included, among others, genes associated with immediate early response (FOS, FOSB, FOSL2, JUN, JUNB, JUND, ATF4, EGR1, EGR3, MYC, IER3, MCL1), LXR activation (APOE, FASN, PTGES3, HNRNPAB, SLC3A2, ETF1, RANBP1, PRDX2), and lineage specification (HBB-BT, CD19) (Figure 5.7B). Pathway enrichment analysis identified the 3 most highly upregulated pathways as EIF2 signaling, elF4/p70S6K signaling, and mTOR signaling (Figure 5.7C). Notably, the NRF2 oxidative stress response, hypoxia signaling, and oxidative phosphorylation were also upregulated (Figure 5.7C). To confirm that DMHCA induced LXR activation in HSCs, we performed a transcription factor activity analysis using the pySCENIC package, which calculates motif enrichments from the regulatory regions of all expressed genes to infer the activity level of known transcription factors. Using this approach, we found that LXRβ activity was increased in the DMHCA-treated cohort, while LXRα activity was below the level of detection for both (Figure 5.7D). These findings are consistent with DMHCA's ability to activate LXR.

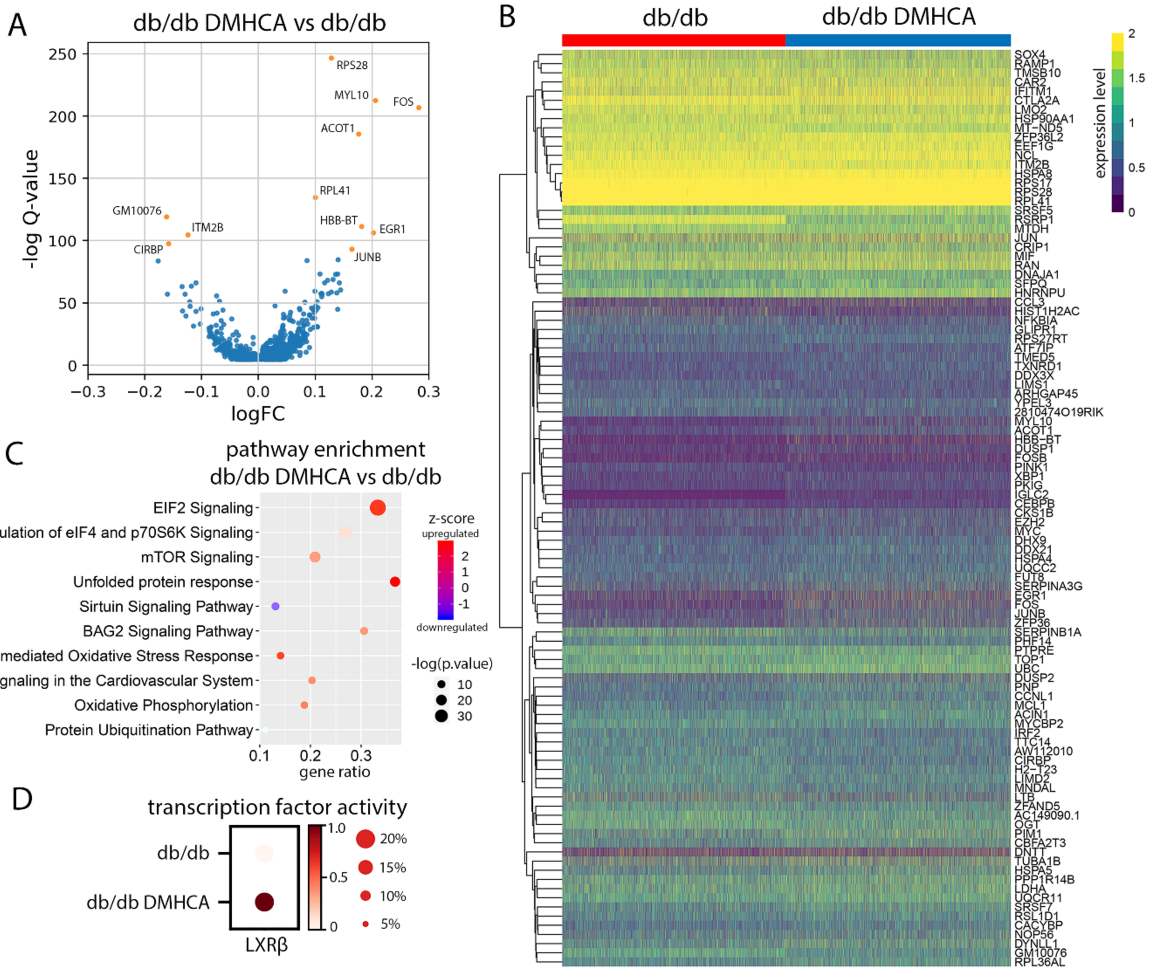

Figure 5.7. DMHCA treatment increases expression of immediate early response genes. (**A**) Differentially expressed genes in DMHCA treated diabetic HSCs. (**B**) Heatmap of the top 100 log (fold change) genes from the DGE analysis. (**C**) Top 10 pathways from IPA pathway enrichment analysis. (**D**) Transcription factor activity analysis of LXRβ in untreated and DMHCA-treated db/db mice.

DMHCA treatment enhances flux down the erythrocyte progenitor lineage. Similar to most differentiation processes, hematopoiesis proceeds across a spectrum of gene expression changes rather than in discrete discernible steps. Thus, single-cell profiles of HSCs represent individual snapshots in time, where each cell falls somewhere along the differentiation spectrum. Pseudotime trajectory analysis relies on the identification of specific gene expression patterns within the data set to map the trajectory of cells along specific lineages. Using this technique, we identified 2 main differentiation pathways - one leading to megakaryocytes, erythrocytes, and DCs and another to peripheral circulating leukocytes (Figure 5.8A). Partition-based graph abstraction (PAGA) analysis uses a similar approach to physically map cells along a spectrum of gene expression changes and provides enhanced resolution. PAGA analysis of the combined data set revealed a similarly distinct split between megakaryocytes/basophils and erythrocytes and peripheral leukocytes, including lymphoid, monocyte, neutrophil, pre-B, and pre-T progenitors (Figure 5.8B). Differentiation along the peripheral leukocyte division mostly precedes through a transition state characterized by low-level expression of several lineage-specific genes, which we refer to as a neutrophil/monocyte/ lymphoid metastate (Figure 5.8C). This metastate then trifurcates into neutrophil, lymphoid, and pre–T cell progenitors (Figure 5.8C). Finally, monocyte progenitors derive from the neutrophil progenitor population, while pre-B cells derive from lymphoid progenitors (Figure 5.8C).

Interestingly, our analysis suggests that differentiation along the dendritic lineage appears more closely related to the megakaryocyte/basophil and erythrocyte family and may actually represent a distinct division arising directly from the HSC compartment (Figure 5.8C). In addition, we further analyzed the potentially novel AP1-high stem cell population to better understand to which lineages these cells contribute. PAGA analysis revealed that AP1-high stem cells are derived directly from HSCs and predominantly give rise to erythrocyte progenitors and, to a lesser degree, megakaryocyte/basophil and DC progenitors (Figure 5.8C). Consistent with our current view of differentiation, maturation along the aforementioned lineages occurs through a gradual increase in lineage-specific genes (Figure 5.8D).

Last, we separated the PAGA analysis into the 2 discrete sample groups and found that DMHCA enhanced flux down the erythrocyte progenitor lineage (Figure 5.8E). Compositional analysis comparing cellular densities between conditions confirmed the increase in erythrocyte progenitor density in DMHCA-treated BM (Figure 5.8F). Impressively, DMHCA not only expanded the proportion of erythrocyte progenitors, but also increased the expression of the hemoglobin β adult t chain (HBB-BT) (Figure 5.8, G and H). Together, these data suggest that, at the earliest stage of hematopoiesis, DMHCA treatment enhances the overall production and robustness of erythrocyte progenitors.

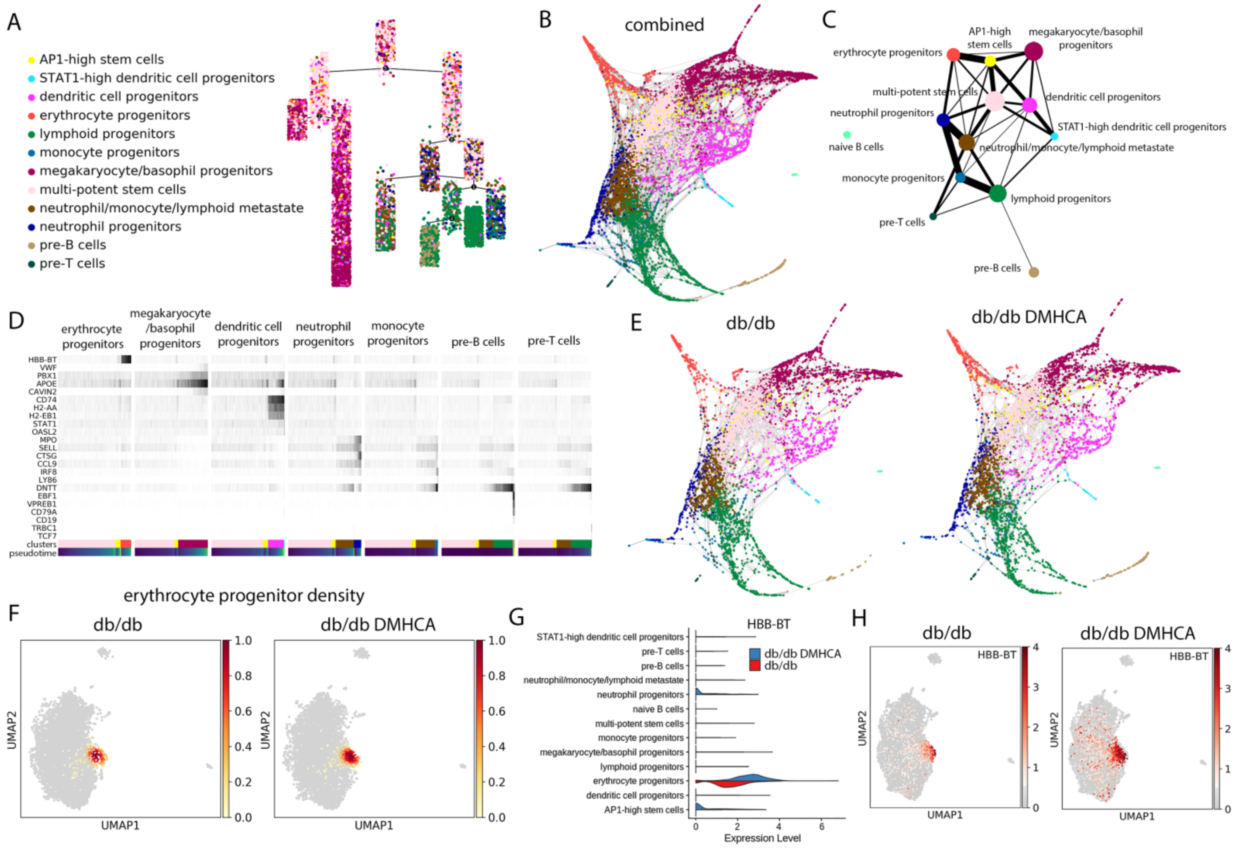

Figure 5.8. Trajectory analysis of HSC differentiation reveals increased erythrocyte progenitor flux with DMHCA treatment. (**A**) Pseudotime trajectory analysis identifies early partitioning of 2 distinct HSC differentiation pathways. (**B**) Diffusion embedding of PAGA analysis. (**C**) Ball-and-stick representation of PAGA analysis. Circle size represents number of cells, and line thickness represents connectivity between 2 groups of cells. (**D**) Gene expression changes of lineage-specific genes along pseudotime differentiation of 7 lineages. (**E**) Diffusion embedding of PAGA analysis separated by sample. (**F**) Compositional analysis showing density graphs of erythrocyte progenitors in untreated and DMHCA-treated diabetic HSCs. (**G**) Violin plots comparing HBB-BT gene expression across samples. (**H**) Spatial representation of HBB-BT gene expression across samples.

DMHCA enhances signaling in the AP1-high stem cell and erythrocyte progenitor populations. We next focused on the AP1-high stem cell and erythrocyte progenitor populations to better understand how DMHCA influences these clusters. Compositional analysis confirmed an increase in the density of the AP1-high stem cell population with DMHCA treatment (Figure 5.9A). Based upon our trajectory analysis, which identified the AP1-high stem cell population as precursors to erythrocyte progenitors, the increase in AP1-high stem cells is consistent with the observed enhancement in erythrocyte flux. We next performed a DGE analysis comparing the AP1- high stem cell populations in untreated and DMHCA-treated mice. Owing to the relatively small number of cells in this population (261 cells total), only 9 genes were found to be differentially expressed and included, among others, the AP1 genes FOS and FOSB and the Krüppel-like family of transcription factors (KLFs) KLF6 and KLF2 (Figure 5.9B). Pathway enrichment analysis focusing on intracellular and secondary messenger signaling identified the ERK and MAPK pathways as the most enriched, followed by glucocorticoid and JAK/STAT signaling (Figure 5.9C).

Next, we performed a DGE analysis comparing the erythrocyte progenitor populations in untreated and DMHCA-treated mice. Across 517 cells, 48 differentially expressed genes were identified (Figure 5.9D). Of note, these included genes involved in the immediate early response (FOS, FOSB, MYC, and IER2), hemoglobin synthesis (HBB-BT), and ribosome synthesis (RPS29, RPS19, RPS28, RPL37, and RPL14) (Figure 5.9D). Using these 48 differentially expressed genes, we performed pathway enrichment focusing on intracellular and secondary messenger signaling. Similar to the AP1-high stem cell population, glucocorticoid, ERK5, and JAK/STAT pathways were significantly enriched (Figure 5.9E).

However, unlike the AP1-high population, the largest enrichment in erythrocyte progenitors was related to translation initiation (EIF2 and EIF4/p70S6K signaling) (Figure 5.9E).

Last, we examined the distribution of AP1 genes across the 13 clusters of the untreated and DMHCA-treated diabetic mice. FOS, which encodes the c-Fos protein, is predominantly expressed in the AP1- high stem cell and naive B cell populations (Figure 5.9, F and G). DMHCA increased FOS expression in nearly all clusters, including most strongly the AP1-high stem cell and naive B cell populations (Figure 5.9, F and G). FOSB expression is highly specific to the AP1-high stem cell and naive B cell populations, and DMHCA increased FOSB in these 2 clusters (Figure 5.9, F and G). JUNB is expressed to varying degrees in all clusters but is predominantly found in the AP1-high stem cell and naive B cell populations (Figure 5.9, F and G). DMHCA treatment increased JUNB expression in all clusters, especially the AP1-high stem cell and naive B cell populations (Figure 5.9, F and G). Last, JUN (c-Jun) and JUND are highly expressed in all clusters, and DMHCA caused a pan-increase in their transcriptional expression (Figure 5.9, F and G).

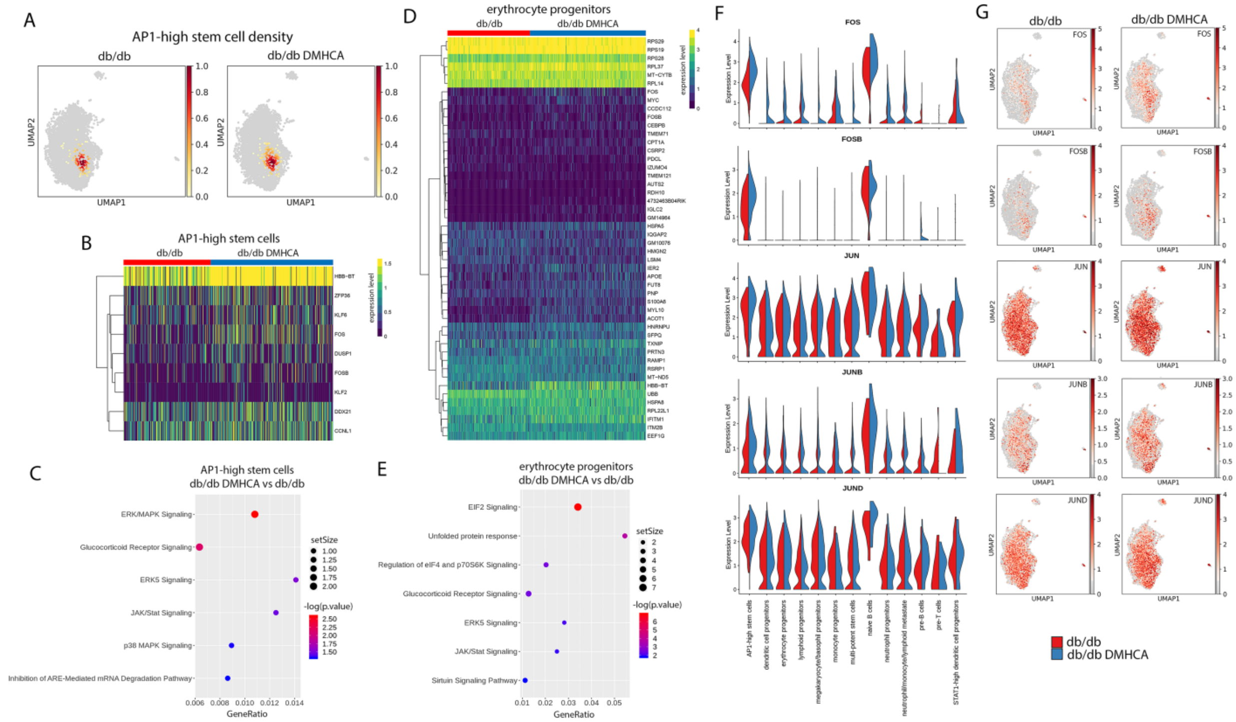

Figure 5.9. DMHCA induces subpopulation gene expression changes and enhances AP-1 signaling. (**A**) Compositional analysis showing density graphs of AP-1 high stem cells in untreated and DMHCA treated diabetic HSCs. (**B**) Heatmap of differentially expressed genes in AP1-high stem cells from untreated and DMHCA treated HSCs. (**C**) Significantly enriched secondary/intracellular signaling pathways in DMHCA treated AP1-high stem cells from IPA pathway enrichment analysis. (**D**) Heatmap of differentially expressed genes in erythrocyte progenitors from untreated and DMHCA treated HSCs. (**E**) Significantly enriched secondary/intracellular signaling pathways in DMHCA treated erythrocyte progenitors from IPA pathway enrichment analysis. (**F**) Violin plots comparing expression of AP-1 complex genes across samples and clusters. (**G**) Spatial representation of AP-1 complex gene expression across samples.

Discussion

Given the selective nature of DMHCA's mechanism of LXR agonism, which promotes cholesterol efflux and hampers systemic inflammation with less induction of hypertriglyceridemia compared with earlier agents, we chose DMHCA for our studies. In aged diabetic db/db mice, DMHCA treatment restores retinal cholesterol homeostasis, slows the development of DR, hampers chronic systemic inflammation, and corrects BM dysfunction. In circulating vascular reparative cells from diabetic patients and db/db mice, DMHCA rejuvenates membrane fluidity and promotes BM egression.

Normally, the retina maintains cholesterol homeostasis by an intricate balance between cholesterol production via local biosynthesis[49-53] and uptake of lipoprotein particles from the circulation, which is opposed by cholesterol efflux via the reverse cholesterol transport pathway or through metabolism of cholesterol to more soluble oxysterols by cytochrome P450s 27A1 and 46A1.[53-57] We have previously reported a reduction in LXR levels in the diabetic retina and in retinal endothelial and retinal pigment epithelial cells isolated from diabetic donor tissue.[19] Moreover, we have demonstrated that genetic LXR downregulation produces retinal phenotypes similar to DR in the absence of diabetes. Reduction in LXR expression in diabetes leads to a decrease in reverse cholesterol transport Moreover, diabetes-induced decrease in the production of natural LXR agonists, oxysterols, further exacerbates retinal cholesterol removal in diabetes. The present study using highly sensitive quantitative LC-MS to measure free and total sterols in the diabetic retina confirmed the effect of diabetes on retinal cholesterol removal pathways and provides insights into the dysfunctional cholesterol homeostasis observed in diabetes. Indeed, we have demonstrated that the total level of cholesterol was significantly increased in the diabetic retina. An increase in cholesterol biosynthesis markers in the retina shows loss of cholesterol homeostasis, with increased cholesterol biosynthesis in spite of already increased cholesterol levels. Remarkably, systemic treatment with DMHCA showed improvement in many aspects of retinal cholesterol metabolism disrupted by diabetes. DMHCA is a synthetic LXR agonist that also inhibits Dhcr24, the enzyme that catalyzes the last step of cholesterol biosynthesis. Indeed, DMHCA treatment led to accumulation of lanosterol and desmosterol and a decrease in cholesterol in the retina due to inhibition of the last step of cholesterol biosynthesis.

In addition to inhibition of cholesterol biosynthesis, we observed that DMHCA reversed diabetes-induced downregulation of LXR-mediated reverse cholesterol transport. DMHCA promotes LXR activation by acting as a direct synthetic agonist, as well as increasing the levels of another potent LXR agonist, desmosterol. DMHCA or desmosterol agonism initiates LXR binding to and promoter activity of the cholesterol efflux pump ABCA1, further contributing to the reduction of retinal cholesterol levels through an increase in cholesterol efflux. Moreover, DMHCA treatment increased free oxysterols showing that DMHCA promotes retinal cholesterol removal by yet another mechanism - through shifting cholesterol metabolism to favor more soluble oxysterols that rapidly diffuse to the systemic circulation and are converted to bile acids by the liver.[57] Overall, our data demonstrate that DMHCA treatment can restore cholesterol homeostasis in the retina through both inhibition of cholesterol biosynthesis and activation of cholesterol efflux by RCT and oxysterol pathways.

To test whether the lipidomic benefits afforded by LXR agonism are sufficient to provide structural and functional benefit in diabetes, we assessed retinal function and membrane fluidity in circulating vascular reparative cells derived from diabetic subjects and mice. We found that DMHCA-treatment corrected several retinopathy endpoints in db/db mice, including reduced vascular dropout and enhanced visual function. Remarkably, in diabetic human derived CD34$^+$ cells, acute ex vivo treatment with DMHCA was sufficient to restore membrane fluidity correcting diabetes-induced dysfunction of circulating vascular reparative cells. Interestingly, DMHCA treatment also reduced leukocyte trafficking to the diabetic retina, providing compelling evidence of DMHCA's anti-inflammatory effects in diabetes.

To test whether DMHCA's antiinflammatory effects extend to the level of the peripheral circulation and BM, we assessed these compartments for inflammatory markers and quantified the proportions of specific cell populations. DMHCA treatment significantly reduced the expression of several important proinflammatory proteins in the BM, including TNF-α, IL-3, and CCL-2. Moreover, DMHCA treatment significantly reduced circulating monocytes and increased the proportion of vascular reparative cells in the BM and circulation.[58,59] Vascular reparative cells are particularly sensitive to alterations in membrane fluidity, as they require flexibility to egress into the circulation and complex intercellular signaling networks to home to areas of injury. These findings on the increased production and egression of CACs complement our membrane fluidity results and suggest that the improvements in membrane fluidity have functional benefits.

Given the beneficial effects of LXR agonism on correcting the homeostatic balance of BM-derived cells, we next explored the HSC and progenitor compartments to test whether DMHCA treatment directly influences hematopoiesis. In LSK cells, DMHCA treatment was sufficient to correct the diabetes-induced increase in MPPs and decrease in LT-HSCs. Moreover, DMHCA reduced granulocyte myeloid progenitor hyperplasia and increased the production of megakaryocyte/erythrocyte progenitors. Last, DMHCA treatment was sufficient to lower ex vivo granulocyte/macrophage CFUs to baseline levels. Taken together, these exciting findings suggest that DMHCA's benefits extend to the hematopoietic stem cell compartment and that LXR agonism corrects diabetic myeloidosis.

To better understand the transcriptional mechanisms responsible for the beneficial effects of LXR agonism on hematopoiesis in the setting of T2D, we performed scRNA-seq on untreated and DMHCA-treated LSK cells. One striking finding in our analysis is that even the most primitive hematopoietic cells appear preprogrammed to enter specific lineages. This is supported by the 13 cell populations identified by unsupervised clustering, which account for nearly all of the main lineages derived from the BM. Another exciting finding from our scRNA-seq analysis is that DC differentiation appears to be more nuanced than previously suggested. A recent single-cell report using c-kit$^+$ murine BM found that dendritic and monocyte lineages split late in differentiation.[60] Our trajectory analysis, which uses a more primitive population of cells and thus provides a higher resolution of early fate decisions, suggests that the dendritic lineage is more closely related to the megakaryocyte/basophil and erythrocyte family and may actually represent a distinct division arising directly from the HSC compartment. Interestingly, in another recent scRNA-seq report on murine LSK sorted HSCs, the authors did not mention the DC lineage.[61] However, inspection of their publicly available data set for expression of early DC markers (CD74, H2-AA, H2-EB1) - as defined by Tusi *et al.*[60] - demonstrated close association of these genes with the HSC population (Supplemental Figure 5.5), supporting our results. This finding on the DC lineage may have important implications, as it suggests that the development of an entire arm of the immune system may be fundamentally different from all other immune cells, which in our analysis, derive from a shared hematopoietic branch. Last, our analysis identifies a potentially novel stem cell population, which we refer to as AP1-high stem cells. This relatively small population of cells express disproportionately high levels of AP1 complex genes and largely lack lineage specification. Trajectory analysis suggests that AP1-high stem cells predominantly give rise to erythrocyte progenitors and, to a lesser degree, megakaryocyte/basophil and DC progenitors. Thus, this cluster may represent a novel HSC population that is an intermediate to the aforementioned lineages.

The main findings from our DMHCA-treated sample were a decrease in the multipotent stem cell population and an increase in the AP1-high stem cell and erythrocyte progenitor populations. Both of these findings are supported in our BM HSC studies, which found that DMHCA suppressed diabetes-induced hyperplasia of MPPs and increased production of erythrocyte/megakaryocyte progenitors. Based upon our trajectory analysis, which identified the AP1-high stem cell population as precursors to erythrocyte progenitors, the increase in AP1-high stem cells is consistent with the observed enhancement in erythrocyte progenitor flux. DGE analysis demonstrated that DMHCA increased the expression of several LXR target genes[60], confirming that DMHCA directly modulates these primitive cells. Moreover, we observed a striking increase in immediate early response genes. These gene targets, such as FOS, EGR1, and MYC, are pleiotropic factors involved in many cell processes, including differentiation. They are termed immediate genes because they are rapidly induced in response to inter- and intracellular signaling.[61] Many of these genes have well-characterized roles in hematopoiesis. For example, FOS expression is known to limit HSC hyperplasia[62], whereas FOS depletion results in a > 90 % reduction of clonogenic B cell precursors[63]. Both of these observations are consistent with our results herein. Given our previous findings on improved membrane fluidity with DMHCA treatment, the increase in immediate early gene expression in HSCs is not surprising, as the enhanced formation of membrane microdomains amplifies the transduction of intercellular signaling. The most highly enriched pathways in DMHCA-treated HSCs were related to ribosome synthesis/translation initiation (EIF2 and EIF4/p70S6K signaling) and mTOR signaling. Moreover, pathway enrichment analysis indicated upregulation of the hypoxia and Nrf2 pathways. At normal steady-state, the BM microenvironment is hypoxic, and cellular stress stimulates increase BM partial pressure of oxygen (pO_2).[64] Nrf2 is the master regulator of several cellular antioxidant pathways. As Nrf2 expression is decreased in diabetic BM cells[65], DMHCA-induced upregulation of Nrf2 may function as a prosurvival response. Together, these findings suggest that DMHCA treatment normalizes the BM microenvironment.

Last, we found key genes and intracellular pathways that were differentially regulated in the treated versus untreated AP1-high stem cell and erythrocyte progenitor populations. DMHCA-treated AP1-high stem cells showed increased AP1 complex genes, as well as increased expression of KLF2 and -6, two genes required for normal erythrocyte development.[66,67] Of note is the increase in MYC expression, which has recently been shown to induce proliferation of erythroid progenitor cells.[68] DGE analysis also showed significantly increased hemoglobin gene expression, suggesting that DMHCA not only increases erythrocyte progenitor flux, but also stimulates the generation of more robust erythrocyte progenitors. Taken together, these data demonstrate that DMHCA enhances HSC signaling and improves erythrocyte differentiation in diabetes.

An important characteristic of DMHCA that is worth noting is its chemical structure. DMHCA is a synthetic oxysterol with a shortened sidechain and amide moiety, giving it amphipathic properties. Like other oxysterols, DMHCA may incorporate into the exofacial leaflet of bilayers and thereby directly modify membrane dynamics and the functions of integral and membrane-associated proteins.[69] This possibility, while not directly measured in this study, may contribute to the observed beneficial and pleotropic effects of long-term DMHCA treatment on T2D db/db mice. One limitation of our study is that we did not include LXRα/β-deficient mice treated with DMHCA, which would have further addressed what portion of the effect we observed was due to LXR agonism and what could have been the result of the biophysical effects of DMHCA on membrane bilayers. However, such studies were performed by Patel *et al.*, where STZ-injected Lxrα/$\beta^{-/-}$ mice on a Western diet were treated with DMHCA and showed no beneficial effect on the kidneys of these mice, whereas DMHCA corrected diabetic nephropathy in WT STZ-injected mice.[70]

Using a multisystem approach, this study demonstrates the broad and pleiotropic effects of LXR activation. While the chemical properties of DMHCA and its potential ability to incorporate into the membrane could account for some of the observed pleotropic effects, our results provide support for the future development of potential therapeutics that capture the benefits of LXR agonism. However, the simultaneous inhibition of SREBP1c will be required, likely heralding the future development of combination therapies to optimize cholesterol homeostasis in diabetic individuals.

Author contributions

CPV designed and performed experiments, analyzed and interpreted results, and wrote the manuscript. SDF analyzed scRNA-seq data, interpreted the data, and wrote the paper. MH performed membrane fluidity assays, analyzed and interpreted the data, and wrote the paper. ALL performed and analyzed flow cytometry experiments, interpreted the data, wrote the paper, and performed aspects of the scRNA-seq study. SSH performed membrane fluidity sample preparation, data analysis, and interpretation. BAB, MSS, YAA, JLF, and SLC performed the animal experiments. DKC aligned sequencing reads and generated feature-barcode matrices. RSW reviewed the analysis of scRNA-seq data, discussed the results, and interpreted the data. GJB analyzed data, discussed the results, and interpreted the data for the membrane fluidity study. JVB designed experiments, discussed and interpreted results, and revised the paper. MBG designed experiments, interpreted the data, discussed the results, wrote the manuscript, and is the guarantor of this work; as such, MBG had full access to all the data in the study and takes responsibility for the integrity of the data and the accuracy of the data analysis.

Acknowledgements

This study was supported by the NIH grants R01EY025383, R01EY012601, R01EY028858, R01EY028037, to MBG; R01EY030766, R01EY016077 to JVB; 5T32GM008361-27 to SDF; F32EY028426 to SH; T32HL134640-01 to MD; and T32HL105349 to JLF.

The authors are grateful for Luecken and Theis[78] whose tutorial on the current best practices in scRNA-seq analyses formed the foundation of the analysis herein.

Conflict of interest: The authors have declared that no conflict of interest exists.

APPENDICES

Appendix A: Supplemental Information

Supplemental Table 5.1. Identification of human subjects. Subjects were enrolled according to the following criteria presented in : (a). Any male or female between the ages of 21–98 years of age were eligible to participate; (b) must have carried the diagnosis of diabetes (either type 1 or type 2 diabetes) or healthy aged control; and (c) was willing and able to cooperate with the eye exam protocol. The exclusion criteria included: (a) subjects with AMD, glaucoma, uveitis, known hereditary degenerations or other significant ocular complications other than diabetic retinopathy; (b) ongoing malignancy; (c) cerebral vascular accident or cerebral vascular procedure; (d) current pregnancy; (e) history of organ transplantation; (f) presence of a graft (to avoid any effect of the graft on inflammatory parameters); (g) evidence of ongoing acute or chronic infection (HIV, Hepatitis B or C, tuberculosis); and (h) subjects with anemia.

ID	Age	Type
C1	49	Control
C2	50	Control
C3	48	Control
C4	24	Control
C5	68	Control
C6	21	Control
C7	69	Control
C8	28	Control
C9	29	Control
C10	42	Control
C11	26	Control
C12	53	Control
C13	50	Control
C14	48	Control
C15	64	Control
C16	50	Control
C17	55	Control
C18	29	Control
C19	71	Control

Supplemental Table 5.1 (cont'd).

ID	Age	Type	HGBA1C	Blood Sugar	Drugs	Left Eye	Right Eye
D1	52	Type 2	5.5	140	Aspir 81, Carisoprodol, Clotrimazole-Betamethasone, Fenofibrate Nanocrystallized, Immune Support Complex, Lipitor, Metformin, Niacin ER, Novolog Pen Fill 100, Rosuvastatin, Valsartan, Vitamin D3, Indapamide	None	None
D2	40	Type 2	Unknown	Unknown	Apidra, Avasin, Lantus	Proliferative	Proliferative
D3	63	Type 2	8.1	229	Fibercon, Losartan, Novofine , Lortab, Trazadone, Oxycodone, Meloxicam, Humalog Mix, Hydrochlorothiazide, Multivitamins, Metformin, Tramadol, Aspirin, Primidone, Simvastatin , Percocet, Bupropion	None	None
D4	58	Type 2	Unknown	Unknown	Amlodipine Besylate ,Lasix, Losartan Potassium, Metoprolol Tartrate, Paxil, Ranitidine HCl	Proliferative	Proliferative

Supplemental Table 5.1 (cont'd).

ID	Age	Type	HGBA1C	Blood Sugar	Drugs	Left Eye	Right Eye
D5	65	Type 2	7.1	136	Actos, Alprazolam, Fluticasone, Nasal Spray, Suspension, Furosemide, Furosemide, Gabapentin, Humalog Mix Insulin, Hydrocodone, Acetaminophen, Jardiance, Kionex, Levothyroxine, Lisinopril, Pramipexole, Primidone, Silver Sulfadiazine, Simvastatin, Spironolactone, Sulfamethoxazole, Tizanidine, Tramadol, Venlafaxine, Victoza, Vitamin D2	Mild Non-proliferative	Mild Non-proliferative
D6	77	Type 2	Unknown	88	Finasteride, Hydrocodone, Metformin, Methimazole, Lisinopril, Nitrofurantoin Monohydrate, Oxybutynin Chloride ER, Sulfamethoxazole, Trazodone, Oxycodone-acetaminophen, Warfarin	None	None
D7	50	Type 2	Unknown	331	Unknown	None	None

Supplemental Table 5.1 (cont'd).

ID	Age	Type	HGBA1C	Blood Sugar	Drugs	Left Eye	Right Eye
D8	52	Type 2	5.5	150	Aspir-81(Delayed Release), Carisoprodol, Clotrimazole-Betamethasone Cream ,Fenofibrate Nanocrystallized, Immune Support Complex, Indapamide, Lipitor, Metformin, Niacin, Novolog Penfill, Rosuvastatin, Valsartan, Vitamin D3,Zoloft	None	None
D9	66	Type 2	Unknown	Unknown	Unknown	None	None
D10	77	Type 2	Unknown	88	Finasteride, Hydrocodone, Metformin, Lisinopril, Methimazole, Nitrofurantoin, Monohydrate, Oxybutynin, Sulfamethoxazole, Trazodone, Oxycodone, Warfarin	None	None
D11	60	Type 2	Unknown	Unknown	Prednisolone Acetate, Tobramycin, Albuterol Sulfate, Lisinopril, Ibuprofen	Pro-liferative	Pro-liferative

Supplemental Table 5.1 (cont'd).

ID	Age	Type	HGBA1C	Blood Sugar	Drugs	Left Eye	Right Eye
D12	41	Type 2	6.7	76	Maxitrol Drop, Acetazolamide, Amlodipine, Apidra, Atorvastatin, Avastin, Gabapentin, Hydrocodone, Lantus, Lisinopril, Novolin, Prednisone, Sumatriptan Tramadol, Trazodone	Pro-liferative	Pro-liferative
D13	62	Type 2	8.1	229	Fibercon, Losartan, Novofine , Lortab, Trazadone, Oxycodone, Meloxicam, Humalog Mix, Hydrochlorothiazide , Multivitamins, Metformin, Tramadol, Aspirin, Primidone, Simvastatin , Percocet, Bupropion	None	None
D14	54	Type 2	8.4	Unknown	Unknown	None	None
D15	48	Type 2	Unknown	186	Cozaar, Lantus, Norvasc, Novolog, Simvastatin	Pro-liferative	Pro-liferative
D16	52	Type 2	Unknown	427	Aspirin, Meclizine, Naprosyn, Neurontin, Novolin R, Sumatriptan	Severe NPDR	Severe NPDR
D17	55	Type 2	11.2	293	Ergocalciferol, Metformin, Novolog Mix, Proair HFA, Simvastatin	Moderate NPDR	Moderate NPDR

Supplemental Table 5.1 (cont'd).

ID	Age	Type	HGBA1C	Blood Sugar	Drugs	Left Eye	Right Eye
D18	59	Type 2	6.0	194	Amlodipine, Atorvastatin, Bupropion, Ciprofloxacin, Clindamycin, Gabapentin, Lisinopril 40mg, Lisinopril 20mg, Metformin, Sulfamethoxazole, Sure Comfort Insulin, Synthroid	Un-specified	Un-specified
D19	69	Type 2	7.4	79	Azelastine, Amlodipine, Azithromycin, Clonidine, Enalapril, Furosemide, Metoprolol, Novolin, Potassium Chloride, Sure Comfort Insulin Syringe	Moderate NPDR	Moderate NPDR

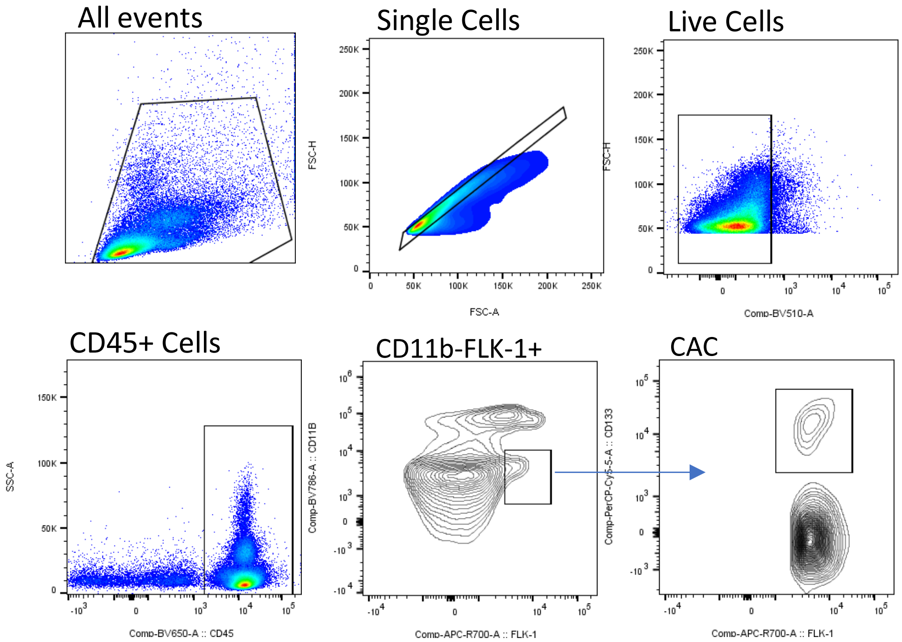

Supplemental Figure 5.1. Gate Strategy of CAC on BM cells and PBMCs. CD45$^+$ cells were gated after exclusion of debris, doublets and dead cells. The FLK-1$^+$CD11b$^-$ cells were defined for further selection of CD133$^+$ cells.

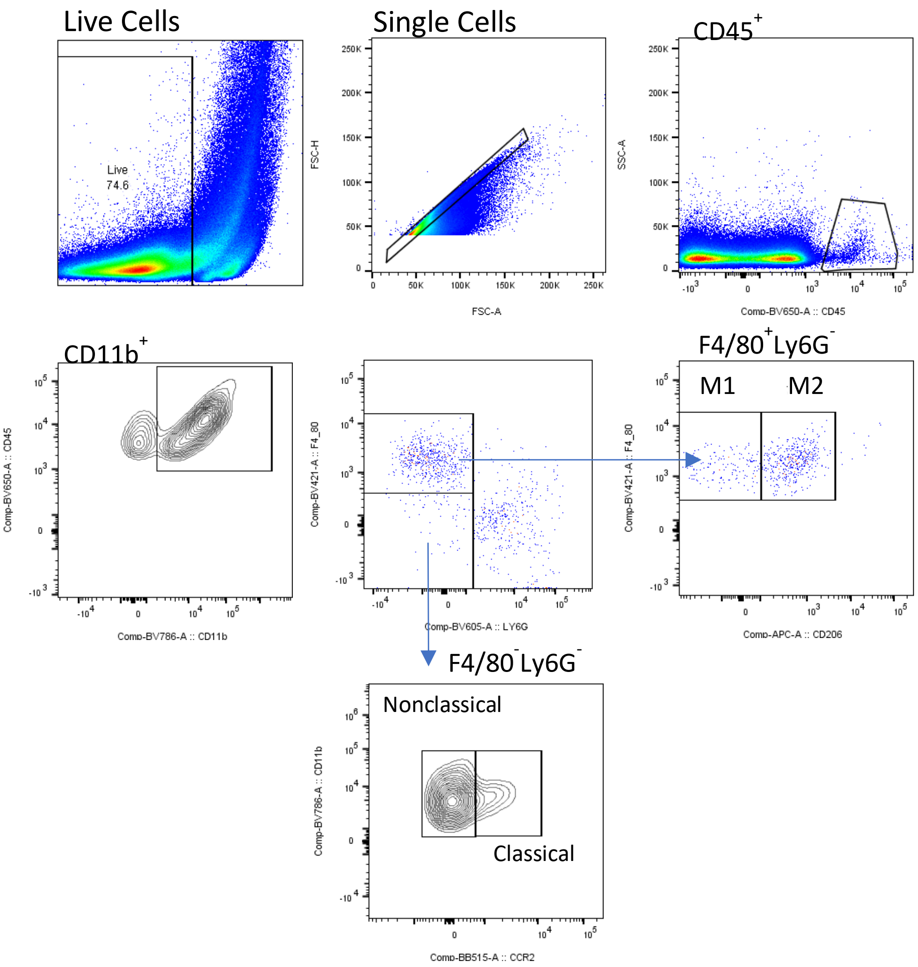

Supplemental Figure 5.2. Gate Strategy to define monocytes and macrophages subtypes on Retina. CD45$^+$ cells were gated after exclusion of doublets and dead cells. The CD11b$^+$ expressing F4/80 and lacking expression of Ly6G were defined as macrophages, further the CD206$^+$ cells were gated to address M2 and CD206$^-$ to define M1 macrophages. Monocytes (CD11b$^+$Ly6G$^-$ F4/80$^-$) were divided into CCR2$^+$ fraction comprised of classical monocytes and CCR2$^-$ fraction defined as nonclassical monocytes.

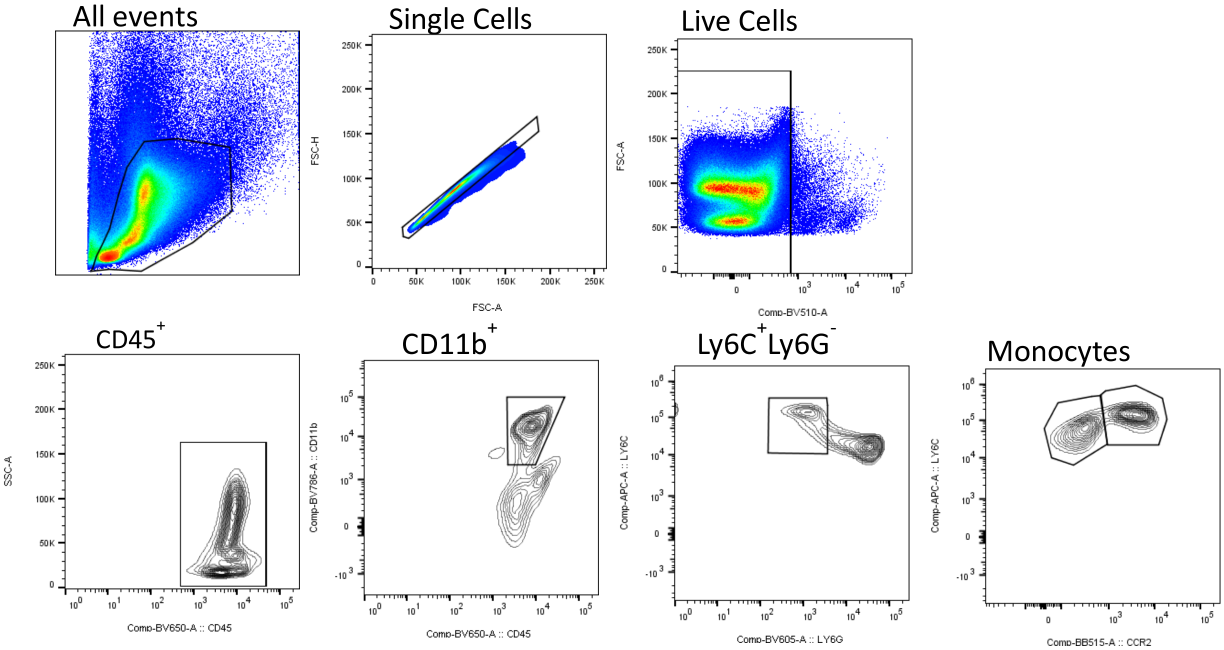

Supplemental Figure 5.3. Gate Strategy of subtypes of monocytes on BM cells and PBMCs. CD45$^+$ cells were gated after exclusion of debris, doublets and dead cells. The CD11b$^+$ expressing Ly6C and lacking expression of Ly6G were defined as monocytes. Monocytes were divided into CCR2$^+$ fraction comprised of classical monocytes and CCR2$^-$ fraction defined as nonclassical monocytes.

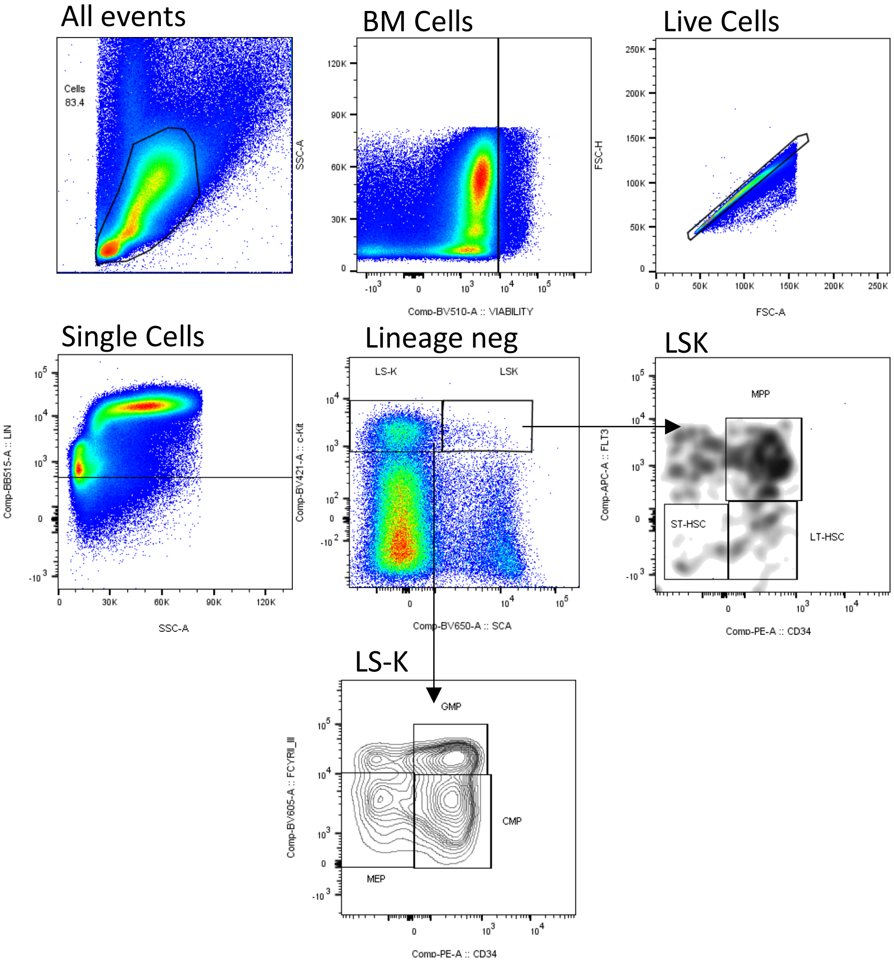

Supplemental Figure 5.4. Gate Strategy of HSC on BM. Lin$^-$ cells were gated after exclusion of debris, doublets and dead cells. Sca-1$^-$c-Kit$^+$ cells (LS-K) were divided in CD34$^+$FcgRII/III$^+$ (GMP), CD34$^+$FcgRII/III$^-$ (CMP) and CD34$^-$FcgRII/III$^-$ (MEP). Sca$^+$c-Kit$^+$ (LSK) were divided in CD34$^+$FLT3$^+$ (MPP), CD34$^+$FLT3$^-$ (LT-HSC) and CD34$^-$FLT3$^-$ (ST-HSC).

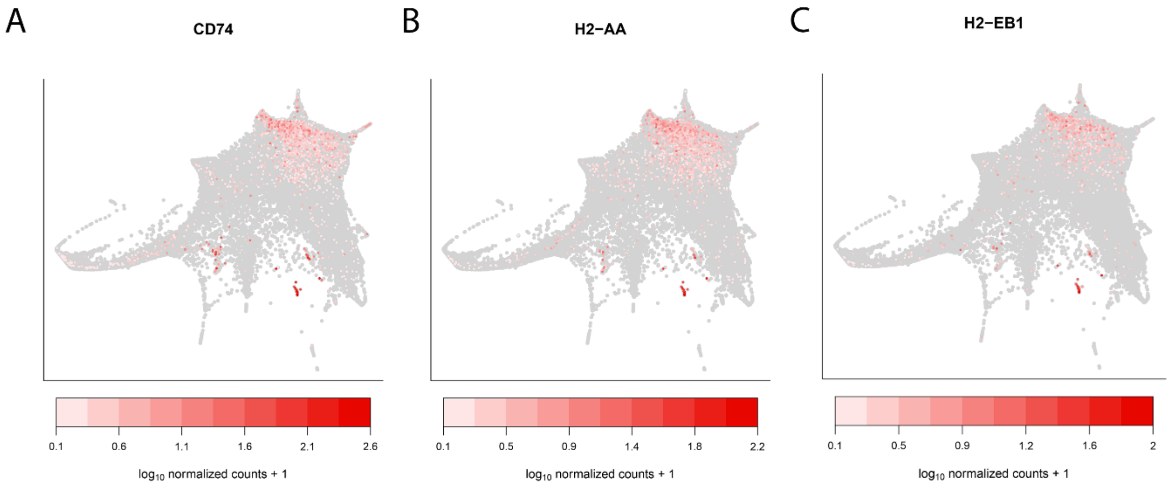

Supplemental Figure 5.5. Expression of dendritic cell markers in scRNA-seq dataset from Dahlin *et al.* 2018. scRNA-seq was performed on 44,802 HSCs derived from Lin$^-$Sca-1$^+$c-Kit$^+$ (LSK) and Lin$^-$c-Kit$^+$ (LK) BM cells. (**A-C**) Force-directed graph embedding of publicly available scRNA-seq data from Dahlin *et al*. 2018 showing spatial distribution of the dendritic cell markers (**A**) CD74, (**B**) H2-AA, and (**C**) H2-EB1.

Supplemental Table 5.2. Panel of antibodies used to determine myeloid cells on bone marrow and blood. For preparation of antibody mixes, Brilliant Stain buffer was used and samples were incubated for 30 minutes at 4°C in the dark, followed by two washes. Titers refer to final dilution factors, and staining volume per sample was 100 µl. SB: Super Bright, BV: Brilliant Violet, BB: Brilliant Blue, AF: AlexaFluor, PE: Phycoerythrin, APC: Allophycocyanin.

Antigen	Fluorophore	Vendor	Number	Titer
Ly6G	SB600	ThermoFisher	63-9668-82	1/200
CD45	SB645	ThermoFisher	64-0451-82	1/100
CD11b	SB780	ThermoFisher	78-0112-82	1/100
CCR2	FITC	R&D Systems	FAB5538F-100	1/100
CD133	PercP-eFluor710	ThermoFisher	46-1331-82	1/100
Ly6C	APC	ThermoFisher	17-5932-52	1/200
Flk-1	AF700	ThermoFisher	56-5821-81	1/100
Viability dye	eFluor506	ThermoFisher	65-0866-14	1/200

Supplemental Table 5.3. Panel of antibodies used to determine precursor cells on bone marrow. For preparation of antibody cocktail, Brilliant Stain buffer was used and samples were incubated for 30 minutes at 4°C in the dark, followed by two washes. Titers refer to final dilution factors, and staining volume per sample was 100 µl. SB: Super Bright, BV: Brilliant Violet, BB: Brilliant Blue, AF: AlexaFluor, PE: Phycoerythrin, APC: Allophycocyanin.

Antigen	**Fluorophore**	**Vendor**	**Number**	**Titer**
c-Kit (CD117)	SB436	ThermoFisher	48-1171-82	1/100
FcyRII/III	SB600	ThermoFisher	63-0161-82	1/100
Sca-1	SB645	ThermoFisher	64-5981-82	1/100
Lineage cocktail	FITC	ThermoFisher	22-7778-72	1/50
CD34	PE	ThermoFisher	MA5-17831	1/100
Flk2/Flt3	APC	ThermoFisher	17-1357-41	1/100
CD127 (IL7Ra)	APC-Cy7	ThermoFisher	47-1271-82	1/100
Viability dye	eFluor506	ThermoFisher	65-0866-14	1/200

Supplemental Table 5.4. Panel of antibodies used to stain isolated cells from retina. For preparation of antibody cocktail, Brilliant Stain buffer was used and samples were incubated 30 minutes at 4°C in the dark, followed by two washes. Titers refer to final dilution factors, and staining volume per sample was 100 µl. SB: Super Bright, BV: Brilliant Violet, BB: Brilliant Blue, AF: AlexaFluor, PE: Phycoerythrin, APC: Allophycocyanin.

Antigen	**Fluorophore**	**Vendor**	**Number**	**Titer**
F4/80	SB436	ThermoFisher	48-4801-82	1/100
Ly6G	SB600	ThermoFisher	63-9668-82	1/200
CD45	SB645	ThermoFisher	64-0451-82	1/100
CD11b	SB780	ThermoFisher	78-0112-82	1/100
CCR2	FITC	R&D Systems	FAB5538F-100	1/100
CD133	PercP-eFluor710	ThermoFisher	46-1331-82	1/100
CD206	APC	ThermoFisher	17-5932-52	1/100
Flk-1	AF700	ThermoFisher	56-5821-81	1/100
Viability dye	eFluor506	ThermoFisher	65-0866-14	1/200

Appendix B: Supplemental Methods

Electroretinogram (ERG). For full-field ERG recordings, mice were dark adapted for 12 h. In preparation for the ERGs, the mice were anesthetized with intramuscular (IM) injections of ketamine and xylazine. The pupils were dilated with 1 % atropine sulfate and 2.5 % phenylephrine hydrochloride ophthalmic solution which also reduced sensitivity of the eyes to touch. When anesthetized, the mice were placed on a stand in a LED Ganzfeld stimulator (LKC Technologies, Gaithersburg, MD. Full-field ERGs were recorded from both eyes using the LKC system.

qRT-PCR. RNA was isolated according with the RNeasy mini kit (74106; Qiagen) according to manufacturer's instructions. First-strand complementary DNA was synthesized from isolated RNA using iScript II reverse transcription supermix (1708841; Bio-Rad). Prepared cDNA was mixed with SsoAdvanced Universal SYBR Green Mix (172570; Bio-Rad) and sets of gene-specific forward and reverse primers (ABCA1, CCL-2) (Bio-Rad) and subjected to real-time PCR quantification using the CFX384 Real Time PCR. Cyclophilin A was used as a control, and results were analyzed using the comparative Ct method and Ct values were normalized to Cyclophilin A levels. Data is shown as normalized relative to control levels or as non-normalized raw expression levels.

Immunofluoresence staining. Enucleated eyes were fixed in 4 % paraformaldehyde overnight at 4 ^{o}C. Eyes were washed 2X for 5 min with PBS(1x) follow by incubation in 30 % sucrose for 48 hrs. and then snap frozen in optical cutting temperature compound. Retinal crossections (12 μm) were processed for immunostaining using rat monoclonal to CD45 antibody (clone 30-F11, R&D

Systems, 1:50). Alexa Fluor 594 was used as the secondary antibody. Positive cells were counted from 3-5 sections at 100 µm interval for each eye with a minimum of four images per section.

Cytokines quantification. Levels of TNF-alpha and CCL-2 were measured on the BM supernatant using Cytometric Bead Array (TNF #888299; CCL-2 #558342), and IL-3 measurement by ELISA kit (R&D system #M3000). The concentrated supernatant was incubated with beads and acquired on a BD FACSCelesta following the manufacturer's instructions. The concentration was determined using a standard curve and analyzing on BD FACSArray software. Protein assay was performed to normalize the concentration in pg/mg.

BM analysis. Bones were harvested from mice in sterile conditions and the supernatant was washed with PBS (1x) containing a protease inhibitory cocktail (AEBSF 1mM, Aprotinin 800nM, Bestatin 50µM, E64 15µM, Leupeptin 20µM, Pepstatin A 10µM) (Thermo Scientific #78438). After centrifugation at 300 x g for 10 min at 4°, the BM supernatant was removed and the cells destined for cell culture analysis or freeze to posterior analysis. The BM supernatant was concentrated with Amicon Ultra-15 (#UFC900324) for 60 min at 3220 x g. The supernatant was used for quantification of cytokines and chemokines

REFERENCES

REFERENCES

1. The ACCORD Study Group and ACCORD Eye Study Group. Effects of Medical Therapies on Retinopathy Progression in Type 2 Diabetes. *N Engl J Med*. 2010;363(3):233-244.

2. Sandhoff R, Brügger B, Jeckel D, *et al*. Determination of cholesterol at the low picomole level by nano-electrospray ionization tandem mass spectrometry. *J Lipid Res.* 1999;40(1):126-132.

3. Stancu C, Sima A. Statins: mechanism of action and effects. *J Cellular Mol Med*. 2001;5(4):378-387.

4. Niesor EJ, Schwartz GG, Perez A, *et al*. Statin-Induced Decrease in ATP-Binding Cassette Transporter A1 Expression via microRNA33 Induction may Counteract Cholesterol Efflux to High-Density Lipoprotein. *Cardiovasc Drugs Ther*. 2015;29(1):7-14.

5. Zheng W, Mast N, Saadane A, *et al*. Pathways of cholesterol homeostasis in mouse retina responsive to dietary and pharmacologic treatments. *J Lipid Res*. 2015;56(1):81-97.

6. Bryszewska M, Watala C, Torzecka W. Changes in fluidity and composition of erythrocyte membranes and in composition of plasma lipids in Type I diabetes. *Br J Haematol*. 1986;62(1):111-116.

7. Kruit JK, Wijesekara N, Fox JEM, *et al*. Islet Cholesterol Accumulation Due to Loss of ABCA1 Leads to Impaired Exocytosis of Insulin Granules. *Diabetes*. 2011;60(12):3186-3196.

8. Simons K, Ehehalt R. Cholesterol, lipid rafts, and disease. *J Clin Invest*. 2002;110(5):597-603.

9. Chen W, Jump DB, Esselman WJ, *et al*. Inhibition of cytokine signaling in human retinal endothelial cells through modification of caveolae/lipid rafts by docosahexaenoic acid. *Invest Ophthalmol Vis Sci*. 2007 Jan;48(1):18-26

10. Sohn J, Lin H, Fritch MR, *et al*. Influence of cholesterol/caveolin-1/caveolae homeostasis on membrane properties and substrate adhesion characteristics of adult human mesenchymal stem cells.*Stem Cell Res Ther*. 2018;3;9(1):86.

11. Wang B, Tontonoz P. Liver X receptors in lipid signalling and membrane homeostasis. *Nat Rev Endocrinol*. 2018;14(8):452-463.

12. Janowski BA, Willy PJ, Devi TR, *et al*. An oxysterol signalling pathway mediated by the nuclear receptor LXRα. *Nature*. 1996;383(6602):728-731.

13. Venkateswaran A, Laffitte BA, Joseph SB, *et al*. Control of cellular cholesterol efflux by the nuclear oxysterol receptor LXRalpha. *Proceedings of the National Academy of Sciences*. 2000;97(22):12097-12102.

14. Rong X, Albert CJ, Hong C, *et al*. LXRs Regulate ER Stress and Inflammation through Dynamic Modulation of Membrane Phospholipid Composition. *Cell Metabolism.* 2013;18(5):685-697.

15. Cermenati G, Abbiati F, Cermenati S, *et al*. Diabetes-induced myelin abnormalities are associated with an altered lipid pattern: protective effects of LXR activation. *J Lipid Res*. 2012;53(2):300-310.

16. Cermenati G, Giatti S, Cavaletti G, *et al*. Activation of the Liver X Receptor Increases Neuroactive Steroid Levels and Protects from Diabetes-Induced Peripheral Neuropathy. *J Neurosci*. 2010;30(36):11896-11901.

17. Joseph SB, McKilligin E, Pei L, *et al*. Synthetic LXR ligand inhibits the development of atherosclerosis in mice. *Proceedings of the National Academy of Sciences*. 2002;99(11):7604-7609.

18. Hazra S, Rasheed A, Bhatwadekar A, *et al*. Liver X Receptor Modulates Diabetic Retinopathy Outcome in a Mouse Model of Streptozotocin-Induced Diabetes. *Diabetes*. 2012;61(12):3270-3279.

19. Hammer SS, Beli E, Kady N, *et al*. The Mechanism of Diabetic Retinopathy Pathogenesis Unifying Key Lipid Regulators, Sirtuin 1 and Liver X Receptor. *EBioMedicine.* 2017;22:181-190.

20. Chisholm JW, Hong J, Mills SA, Lawn RM. The LXR ligand T0901317 induces severe lipogenesis in the db/db diabetic mouse. *J Lipid Res*. 2003;44(11):2039-2048.

21. Kirchgessner TG, Sleph P, Ostrowski J, *et al*. Beneficial and Adverse Effects of an LXR Agonist on Human Lipid and Lipoprotein Metabolism and Circulating Neutrophils. *Cell Metabolism*. 2016;24(2):223-233.

22. Quinet EM, Savio DA, Halpern AR, Chen L, Miller CP, Nambi P. Gene-selective modulation by a synthetic oxysterol ligand of the liver X receptor. *J Lipid Res.* 2004;45(10):1929-1942.

23. Lund EG, Peterson LB, Adams AD, *et al*.,. Different roles of liver X receptor alpha and beta in lipid metabolism: effects of an alpha-selective and a dual agonist in mice deficient in each subtype. *Biochem Pharmacol*. 2006;14;71(4):453-63.

24. Miao B, Zondlo S, Gibbs S, *et al*.,. Raising HDL cholesterol without inducing hepatic steatosis and hypertriglyceridemia by a selective LXR modulator. *J Lipid Res*. 2004;45(8):1410-7

25. Kratzer A1, Buchebner M, Pfeifer T, *et al*., Synthetic LXR agonist attenuates plaque formation in apoE-/- mice without inducing liver steatosis and hypertriglyceridemia. *J Lipid Res*. 2009;50(2):312-26.

26. El-Darzi N, Astafev A, Mast N, *et al*. N,N-Dimethyl-3β-hydroxycholenamide Reduces Retinal Cholesterol via Partial Inhibition of Retinal Cholesterol Biosynthesis Rather Than its Liver X Receptor Transcriptional Activity. *Front Pharmacol.* 2018;25;9:827.

27. Fessler MB. The challenges and promise of targeting the Liver X Receptors for treatment of inflammatory disease. *Pharmacol Ther*. 2018; 181:1-12.

28. Pfeifer T, Buchebner M, Chandak PG, *et al*. Synthetic LXR agonist suppresses endogenous cholesterol biosynthesis and efficiently lowers plasma cholesterol. *Curr Pharm Biotechnol*. 2011;12(2):285-292.

29. Repa JJ. Regulation of mouse sterol regulatory element-binding protein-1c gene (SREBP-1c) by oxysterol receptors, LXRalpha and LXRbeta. *Genes & Development.* 2000;14(22):2819-2830.

30. Schulman IG. Liver X receptors link lipid metabolism and inflammation. *FEBS Lett*. 2017;591(19):2978-2991.

31. Song X, Wu W, Gabbi C, *et al*. Retinal and optic nerve degeneration in liver X receptor β knockout mice. *Proc Natl Acad Sci USA*. 2019;116(33):16507-16512.

32. Choudhary M, Ismail EN, Yao PL, *et al*., LXRs regulate features of age-related macular degeneration and may be a potential therapeutic target. *JCI Insight*. 2020 16;5(1). pii: 131928.

33. Ito A, Hong C, Rong X, *et al*. LXRs link metabolism to inflammation through Abca1-dependent regulation of membrane composition and TLR signaling. *eLife*. 2015;4:e08009.

34. Duan Y, Prasad R, Feng D, *et al*. Bone Marrow-Derived Cells Restore Functional Integrity of the Gut Epithelial and Vascular Barriers in a Model of Diabetes and ACE2 Deficiency. *Circ Res*. 2019;125(11):969-988.

35. Dimmeler S, Zeiher AM. Vascular repair by circulating endothelial progenitor cells: the missing link in atherosclerosis? *J Mol Med*. 2004;82(10):671-677.

36. Fadini GP, de Kreutzenberg S, Agostini C, *et al*. Low CD34+ cell count and metabolic syndrome synergistically increase the risk of adverse outcomes. *Atherosclerosis*. 2009;207(1):213-219.

37. Jarajapu YPR, Hazra S, Segal M, *et al*. Vasoreparative Dysfunction of CD34+ Cells in Diabetic Individuals Involves Hypoxic Desensitization and Impaired Autocrine/Paracrine Mechanisms. Madeddu P, ed. *PLoS ONE*. 2014;9(4):e93965.

38. Li Calzi S, Shaw LC, Moldovan L, *et al*. Progenitor cell combination normalizes retinal vascular development in the oxygen-induced retinopathy (OIR) model. *JCI Insight*. 2019;4(21):e129224.

39. Rasheed A, Tsai R, Cummins CL. Loss of the Liver X Receptors Disrupts the Balance of Hematopoietic Populations, With Detrimental Effects on Endothelial Progenitor Cells. *JAHA*. 2018;7(10).

40. Laffitte BA1, Joseph SB, Walczak R, *et al*. Autoregulation of the human liver X receptor alpha promoter. *Mol Cell Biol*. 2001;21(22):7558-68

41. Schultz JR, Tu H, Luk A, *et al*. Role of LXRs in control of lipogenesis. *Genes Dev*. 2000; 15;14(22):2831-8

42. Blanchard GJ, Busik JV. Interplay between Endothelial Cell Cytoskeletal Rigidity and Plasma Membrane Fluidity. *Biophys J*. 2017;14;112(5):831-833.

43. Chakravarthy H, Navitskaya S, O'Reilly S, *et al*. Role of Acid Sphingomyelinase in Shifting the Balance Between Proinflammatory and Reparative Bone Marrow Cells in Diabetic Retinopathy. *Stem Cells*. 2016;34(4):972-83.

44. Ayee MAA, LeMaster E, Shentu TP, *et al*. Molecular-Scale Biophysical Modulation of an Endothelial Membrane by Oxidized Phospholipids. *Biophys J*. 2017;24;112(2):325-338.

45. Bogdanov P, Corraliza L, Villena JA, *et al*. The db/db mouse: a useful model for the study of diabetic retinal neurodegeneration. *PLoS One*. 2014;16;9(5):e97302.

46. Cheung AK, Fung MK, Lo AC, *et al*. Aldose reductase deficiency prevents diabetes-induced blood-retinal barrier breakdown, apoptosis, and glial reactivation in the retina of db/db mice. *Diabetes*. 2005;54(11):3119-25

47. Ferraro F, Lymperi S, Méndez-Ferrer S, *et al*. Diabetes impairs hematopoietic stem cell mobilization by altering niche function. *Sci Transl Med*. 2011;12;3(104):104ra101.

48. Hazra S, Jarajapu YP, Stepps V, *et al*. Long-term type 1 diabetes influences haematopoietic stem cells by reducing vascular repair potential and increasing inflammatory monocyte generation in a murine model. *Diabetologia*. 2013;56(3):644-53.

49. Fliesler SJ, Florman R, Rapp LM, *et al*. In vivo biosynthesis of cholesterol in the rat retina. *FEBS Lett* 1993;335:234-8.

50. Fliesler SJ, Florman R, Keller RK. Isoprenoid lipid metabolism in the retina: dynamics of squalene and cholesterol incorporation and turnover in frog rod outer segment membranes. *Exp Eye Res* 1995;60:57-69.

51. Lin JB, Mast N, Bederman IR, *et al*. Cholesterol in mouse retina originates primarily from in situ de novo biosynthesis. *J Lipid Res* 2016;57:258-64, PMC4727421.

52. Fliesler SJ, Bretillon L. The ins and outs of cholesterol in the vertebrate retina. *J Lipid Res* 2010;51:3399-413, 2975712.

53. Zheng W, Reem RE, Omarova S, *et al*. Spatial distribution of the pathways of cholesterol homeostasis in human retina. *PLoS One* 2012;7:e37926, 3358296

54. Pikuleva IA, Curcio CA. Cholesterol in the retina: the best is yet to come. *Prog Retin Eye Res* 2014;41:64-89, PMC4058366.

55. Pikuleva IA. Cholesterol-metabolizing cytochromes P450: implications for cholesterol lowering. *Expert opinion on drug metabolism & toxicology* 2008;4:1403-14, 2957831

56. Omarova S, Charvet CD, Reem RE, *et al*. Abnormal vascularization in mouse retina with dysregulated retinal cholesterol homeostasis. *J Clin Invest* 2012;122:3012-23, 3408752.

57. Meaney S, Bodin K, Diczfalusy U, *et al*. On the rate of translocation in vitro and kinetics in vivo of the major oxysterols in human circulation: critical importance of the position of the oxygen function. *J Lipid Res* 2002;43:2130-5.

58. Zafar B, Krishnasamy SS, Shaj J, *et al*. Circulatng angeogenic stem cells in type 2 diabetes are associated with glycine control and endothelial dysfunction. *PLoS One*. 2018;13(10).

59. Petrelli A, Maestroni A, Fadini, *et al*. Improved function of circulating angiogenic cells is evident in type 1 diabetic islet-transplanted patients. *Am J Transplant.* 2010;10(12):2690-700.

60. Tusi BK, Wolock SL, Weinreb C, *et al*. Population snapshots predict early haematopoietic and erythroid hierarchies. *Nature*. 2018;555(7694):54-60.

61. Dahlin JS, Hamey FK, Pijuan-Sala B. A single-cell hematopoietic landscape resolves 8 lineage trajectories and defects in Kit mutant mice. *Blood*. 2018;131(21):e1-e11.

62. Okada S, Fukuda T, Inada K, *et al*. Prolonged expression of c-fos suppresses cell cycle entry of dormant hematopoietic stem cells.Blood. 1999 Feb 1;93(3):816-25

63. Okada S, Wang ZQ, Grigoriadis AE, *et al*. Mice lacking c-fos have normal hematopoietic stem cells but exhibit altered B-cell differentiation due to an impaired bone marrow environment. *Mol Cell Biol.* 1994;14(1):382-90

64. Spencer JA, Ferraro F, Roussakis E, *et al*. Direct measurement of local oxygen concentration in the bone marrow of live animals. *Nature*. 2014;10;508(7495):269-73.

65. Rabbani PS, Soares MA, Hameedi SG, *et al*. Dysregulation of Nrf2/Keap1 Redox Pathway in Diabetes Affects Multipotency of Stromal Cells. *Diabetes*. 2019;68(1):141-155.

66. Basu P, Morris PE, Haar JL, *et al*. KLF2 is essential for primitive erythropoiesis and regulates the human and murine embryonic beta-like globin genes in vivo. *Blood.* 2005;106: 2566-2571

67. Matsumoto N, Kubo A, Liu H, *et al*. Developmental regulation of yolk sac hematopoiesis by Kruppel-like factor 6. *Blood*. 2006;107(4):1357-65. Epub 2005

68. Mayers S, Moço PD, Maqbool T, *et al*. Establishment of an erythroid progenitor cell line capable of enucleation achieved with an inducible c-Myc vector. *BMC Biotechnol.* 2019;19(1):21.

69. Covey DF. ent-Steroids: Novel Tools for Studies of Signaling Pathways. Steroids. 2009 Jul;74(7):577-85.

70. Patel M, Wang XX, Magomedova L, *et al*. Live X receptors preserve renal glomerular integrity under normoglycaemia and in diabetes in mice. Diabetologia. 2014 Feb;57(2):435-46.

71. Axelrod D, Koppel DE, Schlessinger J, Elson E, Webb WW. Mobility measurement by analysis of fluorescence photobleaching recovery kinetics. *Biophys J*. 1976;16(9):1055-69

72. Ishikawa-Ankerhold H, Ankerhold R, Drummen G. Fluorescence Recovery After Photobleaching (FRAP). *Encyclopedia of Life Sciences*. John Wiley & Sons, Ltd: Chichester 2014, 1-11.

73. Lydic TA, Busik JV, Reid GE. A monophasic extraction strategy for the simultaneous lipidome analysis of polar and nonpolar retina lipids. *J Lipid Res*. 2014;55(8):1797-809.

74. McDonald JG, Thompson BM, McCrum EC, *et al*. Extraction and analysis of sterols in biological matrices by high performance liquid chromatography electrospray ionization mass spectrometry. *Methods Enzymol*. 2007;432:145-70

75. Machacek M, Saunders H, Zhang Z, *et al*. Elevated O-GlcNAcylation enhances pro-inflammatory Th17 function by altering the intracellular lipid microenvironment. *J Biol Chem*. 2019;294(22):8973-8990.

76. Bhatwadekar A, Glenn JV, Figarola JL, *et al*. A new advanced glycation inhibitor, LR-90, prevents experimental diabetic retinopathy in rats. *Br J Ophthalmol* 2008;92:545–547

77. Duan Y, Beli E, Li Calzi S, *et al*. Loss of Angiotensin-Converting Enzyme 2 Exacerbates Diabetic Retinopathy by Promoting Bone Marrow Dysfunction. *Stem Cells*. 2018;36(9):1430-1440.

78. Luecken MD, Theis FJ. Current best practices in single-cell RNA-seq analysis: a tutorial. *Mol Syst Biol*. 2019;15(6):e8746.

79. Lun AT, Bach K, Marioni JC. Pooling across cells to normalize single-cell RNA sequencing data with many zero counts. *Genome Biol*. 2016 27; 17:75.

80. Tirosh I, Izar B, Prakadan SM, *et al*. Dissecting the multicellular ecosystem of metastatic melanoma by single-cell RNA-seq. *Science*. 2016;352(6282):189-96.

81. Johnson WE, Li C, Rabbinic A. Adjusting batch effects in microarray expression data using empirical Bayes methods. *Biostatistics*. 2007;8(1):118-27

82. Han X, Wang R, Zhou Y. Mapping the Mouse Cell Atlas by Microwell-Seq. *Cell*. 2018;172(5):1091-1107.e17.

83. Finak G, McDavid A, Yajima M *et al*. MAST: a flexible statistical framework for assessing transcriptional changes and characterizing heterogeneity in single-cell RNA sequencing data. *Genome Biol*. 2015;10(16):278.

84. Aibar S, Gonzalez-Blas CB, Moerman T, *et al*. SCENIC: Singe-Cell regulatory network interference and clustering. Nat Methods. 2017 Nov;14(11):1083-1086.

CHAPTER 6: CONCLUSIONS AND FUTURE DIRECTIONS

The goal of this research was to study the effects of external factors such as anesthetics and the diabetes disease state on the fluidity of model and live cell membranes. Utilizing fluorescence recovery after photobleaching (FRAP) (Chapter 2), we studied the effects of short chain alcohols ethanol and *n*-butanol on a model planar supported lipid bilayer, discussed in Chapter 3. Pillman had prepared an artificial lipid bilayer composed of 1,2-dimyristoyl-*sn*-phosphatidylcholine (DMPC) and perylene and applied varying concentrations of ethanol from 0.25 to 1.00 M at both 289 K (gel phase) and 303 K (fluid phase).[1] Around 0.6 M, there were perturbations to the rotational diffusion motion of perylene at both temperatures, assessed by time resolved fluorescence measurements. The results are consistent with the DMPC phospholipids undergoing interdigitation, in agreement with the literature.[2-8] Setiawan also performed similar fluorescence measurements and varied ethanol concentrations but at room temperature on a model composed of DOPC, cholesterol, sphingomyelin, and sulforhodamine-tethered DOPE fluorescent probe.[9] The ternary lipid composition mimics more closely that of a plasma membrane, and sphingomyelin was necessary for phase segregated structures.[9-11] Fluorescence anisotropy decay images (FADI) and decay time constants were indicative of structural transitions at *ca.* 0.8 M ethanol, and the structure degraded at 1.5 M. He performed a similar study using *n*-butanol and noticed drastic changes at lower concentrations than for ethanol. Around 0.4 M *n*-butanol, there appeared to be two structural domains.

We reproduced Setiawan's model but replaced the rhodamine chromophore (sensitive to phospholipid head group motion) with perylene which probes tail group mobility. Moreover, we utilized FRAP to obtain translational diffusion constants on the micrometer to sub-millimeter scale, opposed to FADI which affords information on the submicron level. We noticed an overall increase, followed by a decrease in diffusion coefficients over varying alcohol concentrations implying the bilayer interdigitation phenomenon, results of which are in Chapter 3.

The ultimate objective of this work was to understand general anesthetics molecular mechanisms and though the work presented here are small steps, they set the foundation for experiments with general anesthetics used in modern medicine, ranging from inhaled or intravenous compounds. We applied 0.3 - 1.5 M ethanol and 0.1 - 0.6 M *n*-butanol (toxic concentrations) to draw parallels to previous work, but clinically relevant concentrations of general anesthetics range from 10 - 100 mM and could be tested in future work.[12] For example, Herold *et al.* performed a gramicidin-based fluorescence assay to gauge the effects of general anesthetics on lipid bilayer elastic properties and, depending on the drug, found minimal changes at clinically relevant concentrations but some alterations at supratherapeutic and potentially toxic concentrations.[12]

In Chapter 4, we also used the rhodamine probe of Setiawan's model and obtained similar fluorescence images with dark circular spots representing cholesterol domains and bright spots likely phospholipids. An unexplored area was the observation by Setiawan and Blanchard that the bright areas surrounded the dark regions (cholesterol), and those bright regions expanded upon increasing light exposure (private communication). One possibility is that the bright region growth was a result of heating and annealing, but further experimentation is clearly required.

Despite conducting multiple trials carefully, every lab environment has a unique contamination profile, and lipids degrade due to oxidation from exposure to oxygen, making it challenging to obtain reproducible translational diffusion constants. Other reasons involved experimental difficulties and working with a heterogeneous system, revealed from histograms of translational diffusion data. Lipid vesicles were formed by a vesicle extrusion method, and another common way of forming the liposomes is via sonication where the duration controls the particle size.[13] Lapinski *et al.* found that vesicles consisting of DOPC, with and without cholesterol, resulted in similar molecular scale environments and translational diffusion behaviors.[13] However, we had more success with extrusion (especially with ceramide-based models), even though it is more time-consuming than sonication potentially due to working with ternary and quaternary lipid systems. It may be useful to compare results from FRAP measurements on bilayers formed from said vesicles formed by both sonication and extrusion. Thereafter, we characterized the particle size distribution of vesicle solutions and suggest researchers also use transmission electron microscopy, which yields complementary information on the morphology. The vesicles were then deposited on a mica substrate using a popular fusion method, and other techniques are worth exploring such as solvent-assisted lipid bilayer (SALB) method, which works on various material supports.[14, 15] Aqueous solutions of Tris® buffer (pH ~ 7.5) and calcium chloride (2 mM) were applied on the mica supported lipid bilayer, whose pH and ionic strength affect bilayer properties.

Mize, for instance, varied both on a ternary lipid model of DOPC, cholesterol, and sphingomyelin (probed with fluorescent tethered sulforhodamine-DOPE) and highlighted interactions among the lipids, mica support, and overlayer solution.[16] At low and high pHs, charge repulsions would be expected between DOPC and sphingomyelin phosphate groups due to protonation and hydroxide ions in solution, respectively. For increasing ionic strengths, the lipids could experience a smaller extent of intermolecular interactions with each other. Temperature also has significant effects, observed by Pillman (*vide supra*).[1] Numerous other parameters from individual lipid mole percentages and total lipid concentration to type of support may be changed to optimize the system of interest, but from a broader perspective, heterogeneity tends to manifest itself and needs to be characterized.

Toward that goal, diffusion coefficients varied over photobleaching spot sizes in our ceramide-system, indicative of non-Gaussian anomalous diffusion. An approach to describing the anomalous behavior is with Lévy motions/distributions which are random walks of multiple short steps and much longer ones between.[17] Some use Lévy flights for instantaneous steps and Lévy walks for steps of finite velocity, while others use the terms interchangeably.[18, 19] Atomic force microscopy and more translational diffusion data could be connected with Lévy models to gain insight in how the molecules are distributed and interact with each other.

Though we simplified our membrane model by considering only lipid contributions, protein inclusion would represent a biological membrane more closely, especially for distinguishing between direct and indirect actions of anesthesia mechanisms. Moving forward, connections between the well-controlled model system and live neuronal cell membranes could prove insightful by performing similar FRAP experiments on the latter. As part of a collaborative work with the Busik laboratory at Michigan State University, membrane fluidity experiments were conducted on plasma membranes of circulating angiogenic cells (CACs).

Diabetes may lead to multiple complications, one of which is sight-threatening diabetic retinopathy. It is thought that restoring the fluidity of CAC membranes could enable them to home to sites of retinal injury and repair damaged blood vessels. Therefore, the CACs were treated with the compound N, N-dimethyl-3β-hydroxy-cholenamide (DMHCA). Among other beneficial effects, DMHCA is an LXR agonist which restores cholesterol levels. Indeed, the membrane fluidity does increase upon treating CACs ex-vivo, compared to control samples (no treatment), the results of which were presented in Chapter 5. For future consideration, the effects of other drugs could be promising. For example, acid sphingomyelinase (ASM) hydrolyzes sphingomyelin to pro-inflammatory, pro-apoptotic ceramide[20] by removing the phosphocholine headgroup, and the drug desipramine blocks ASM, leading to an accumulation of sphingomyelin and a consequent decrease in ceramide levels[21]. It is hypothesized that ceramide reduction could be another pathway for rejuvenating CAC membrane fluidity.[20, 22-24] Similar experiments with the DMHCA drug, with patient and animal subjects could provide important results.

In a plasma membrane there are hundreds of distinct molecular species[25] and one change may have multiple effects. For instance, membrane fluidity may be influenced by the cytoskeleton.[26-29] Specifically, it is universally thought that lowering cholesterol increases membrane fluidity. However, recent work by Levitan *et al.* shows that decreasing cholesterol could actually make a cell more stiff due to the complex interplay between actin filaments (F-actin) and other cellular components.[30] In conclusion, the field of biomimetic membranes is a growing area of research, and the utilization of fluorescence recovery after photobleaching to measure live circulating angiogenic cell membrane fluidity is a novel application; both areas open the possibilities of unraveling molecular mechanisms at play in biological membranes.

REFERENCES

REFERENCES

1. Pillman, H. A.; Blanchard, G. J., Effects of Ethanol on the Organization of Phosphocholine Lipid Bilayers. *Journal of Physical Chemistry B* **2010,** *114*, 3840-3846.

2. Vierl, U.; Löbbecke, L.; Nagel, N.; Cevc, G., Solute Effects on the Colloidal and Phase Behavior of Lipid Bilayer Membranes: Ethanol-Dipalmitoylphosphatidylcholine Mixtures. *Biophysical Journal* **1994,** *67* (3), 80572-80577.

3. Rowe, E. S., Lipid Chain Length and Temperature Dependence of Ethanol-Phosphatidylcholine Interactions. *Biochem.* **1983,** *22*, 3299-3305.

4. Bondar, O. P.; Rowe, E. S., Role of Cholesterol in the Modulation of Interdigitation in Phosphatidylethanols. *Biochimica et Biophysica Acta* **1998,** *1370* (2), 207-217.

5. Lobbecke, L.; Cevc, G., Effects of Short-Chain Alcohols on the Phase Behavior and Interdigitation of Phosphatidylcholine Bilayer Membranes. *Biochim. Biophys. Acta* **1995,** *1237*, 59.

6. McIntosh, T. J.; Lin, H.; Li, S.; Huang, C., The Effect of Ethanol on the Phase Transition Temperature and the Phase Structure of Monounsaturated Phosphatidylcholines. *Biochimica et Biophysica Acta* **2001,** *1510* (1-2), 219-230.

7. Bartucci, R.; Páli, T.; Marsh, D., Lipid Chain Motion in an Interdigitated Gel Phase: Conventional and Saturation Transfer ESR of Spin-Labeled Lipids in Dipalmitoylphosphatidylcholine-Glycerol Dispersions. *Biochemistry* **1993,** *32* (1), 274-281.

8. Hata, T.; Matsuki, H.; Kaneshina, S., Effect of local anesthetics on the bilayer membrane of dipalmitoylphosphatidylcholine: interdigitation of lipid bilayer and vesicle-micelle transition. *Biophysical Chemistry* **2000,** *87* (1), 25-36.

9. Setiawan, I.; Blanchard, G. J., Ethanol-Induced Perturbations to Planar Lipid Bilayer Structures. *J. Phys. Chem. B* **2014,** *118*, 537-546.

10. Setiawan, I.; Blanchard, G. J., Structural Disruption of Phospholipid Bilayers over a Range of Length Scales by n-Butanol. *J. Phys. Chem. B* **2014,** *118*, 3085-3093.

11. Tamm, L. K.; McConnell, H. M., Supported Phospholipid Bilayers. *Biophys J* **1985,** *47* (1), 105-113.

12. Herold, K. F.; Sanford, R. L.; Lee, W.; Andersen, O. S.; Hemmings, H. C., Clinical concentrations of chemically diverse general anesthetics minimally affect lipid bilayer properties. *Proc Natl Acad Sci U S A* **2017,** *114* (12), 3109-3114.

13. Lapinski, M. M.; Blanchard, G. J., The Role of Phospholipid Headgroups in Mediating Bilayer Organization. Perturbations Induced by the Presence of a Tethered Chromophore. *Chem Phys Lipids* **2007,** *150* (1), 12-21.

14. Jackman, J. A.; Cho, N. J., Supported Lipid Bilayer Formation: Beyond Vesicle Fusion. *Langmuir* **2020,** *36* (6), 1387-1400.

15. Ferhan, A. R.; Yoon, B. K.; Park, S.; Sut, T. N.; Chin, H.; Park, J. H.; Jackman, J. A.; Cho, N. J., Solvent-assisted Preparation of Supported Lipid Bilayers. *Nat Protoc* **2019,** *14* (7), 2091-2118.

16. Mize, H. E.; Blanchard, G. J., Interface-Mediation of Lipid Bilayer Organization and Dynamics. *Phys. Chem. Chem. Phys.* **2016,** *18*, 16977-16985.

17. Reynolds, A. M., Current Status and Future Directions of Lévy Walk Research. *Biol Open* **2018,** *7* (1), 1-6.

18. Weeks, E. R.; Swinney, H. L., Anomalous diffusion resulting from strongly asymmetric random walks. *Phys. Rev. E* **1998,** *57* (5), 4915-4920.

19. Dybiec, B.; Gudowska-Nowak, E.; Barkai, E.; Dubkov, A. A., Lévy Flights Versus Lévy Walks in Bounded Domains. *Phys Rev E* **2017,** *95* (5-1), 1-13.

20. Kady, N.; Yan, Y.; Salazar, T.; Wang, Q.; Chakravarthy, H.; Huang, C.; Beli, E.; Navitskaya, S.; Grant, M.; Busik, J., Increase in Acid Sphingomyelinase Level in Human Retinal Endothelial Cells and CD34+ Circulating Angiogenic Cells Isolated From Diabetic Individuals Is Associated With Dysfunctional Retinal Vasculature and Vascular Repair Process in Diabetes. *Journal of Clinical Lipidology* **2017,** *11* (3), 694-703.

21. Jiang, M.; Huang, S.; Duan, W.; Liu, Q.; Lei, M., Inhibition of Acid Sphingomyelinase Activity Ameliorates Endothelial Dysfunction in db/db Mice. *Bioscience Reports* **2019,** *39* (4), 1-10.

22. Tikhonenko, M.; Lydic, T. A.; Opreanu, M.; Li Calzi, S.; Bozack, S.; McSorley, K. M.; Sochacki, A. L.; Faber, M. S.; Hazra, S.; Duclos, S.; Guberski, D.; Reid, G. E.; Grant, M. B.; Busik, J. V., N-3 Polyunsaturated Fatty Acids Prevent Diabetic Retinopathy by Inhibition of Retinal Vascular Damage and Enhanced Endothelial Progenitor Cell Reparative Function. *PLoS One* **2013,** *8* (1), e55177.

23. Chakravarthy, H.; Navitskaya, S.; O'Reilly, S.; Gallimore, J.; Mize, H.; Beli, E.; Wang, Q.; Kady, N.; Huang, C.; Blanchard, G. J.; Grant, M. B.; Busik, J. V., Role of Acid Sphingomyelinase in Shifting the Balance Between Proinflammatory and Reparative Bone Marrow Cells in Diabetic Retinopathy. *Stem Cells* **2016,** *34* (4), 972-983.

24. Opreanu, M.; Tikhonenko, M.; Bozack, S.; Lydic, T. A.; Reid, G. E.; McSorley, K. M.; Sochacki, A.; Perez, G. I.; Esselman, W. J.; Kern, T.; Kolesnick, R.; Grant, M. B.; Busik, J. V., The Unconventional Role of Acid Sphingomyelinase in Regulation of Retinal Microangiopathy in Diabetic Human and Animal Models. *Diabetes* **2011,** *60* (9), 2370-2378.

25. Heimburg, T., Coupling of chain melting and bilayer structure: domains, rafts, elasticity and fusion. *Membrane Science and Technology* **2003,** *7*, 269-293.

26. Yeung, T.; Georges, P. C.; Flanagan, L. A.; Marg, B.; Ortiz, M.; Funaki, M.; Zahir, N.; Ming, W.; Weaver, V.; Janmey, P. A., Effects of Substrate Stiffness on Cell Morphology, Cytoskeletal Structure, and Adhesion. *Cell Motil Cytoskeleton* **2005,** *60* (1), 24-34.

27. Wang, N.; Butler, J. P.; Ingber, D. E., Mechanotransduction Across the Cell Surface and Through the Cytoskeleton. *Science* **1993,** *260* (5111), 1124-1127.

28. Maniotis, A. J.; Chen, C. S.; Ingber, D. E., Demonstration of Mechanical Connections Between Integrins, Cytoskeletal Filaments, and Nucleoplasm That Stabilize Nuclear Structure. *Proc Natl Acad Sci U S A* **1997,** *94* (3), 849-854.

29. Byfield, F. J.; Aranda-Espinoza, H.; Romanenko, V. G.; Rothblat, G. H.; Levitan, I., Cholesterol Depletion Increases Membrane Stiffness of Aortic Endothelial Cells. *Biophys J* **2004,** *87* (5), 3336-3343.

30. Ayee, M. A.; Levitan, I., Paradoxical Impact of Cholesterol on Lipid Packing and Cell Stiffness. *Front Biosci (Landmark Ed)* **2016,** *21*, 1245-1259.